Time Resolved Diagnostic Study of High Power Impulse Magnetron Sputtering (HiPIMS) Discharges

A thesis submitted in partial fulfilment of the requirements to the University of Liverpool for the Degree of Doctor Philosophy

Anurag Kumar Mishra

Department of Electrical Engineering and Electronics
University of Liverpool, Brownlow Hill
Liverpool (United Kingdom), L69 3GJ

January, 2011

DECLARATION

This thesis is a presentation of my original research work. Wherever contributions of others are involved, every effort is made to indicate this clearly, with due reference to the literature, and acknowledgement of collaborative research and discussions. The work was done under the guidance of Professor J. W. Bradley, at the Department of Electrical Engineering and Electronics, University of Liverpool, Liverpool, United Kingdom.

(Anurag Kumar Mishra)

Date: 11.03.2011

In my capacity as supervisor of the candidate's thesis, I certify that the above statements are true to the best of my knowledge.

(Prof. J. W. Bradley)
Department of Electrical Engineering and Electronics
University of Liverpool, Brownlow Hill, Liverpool, United Kingdom
L69 3GJ

ABSTRACT

HiPIMS (High Power Impulse Magnetron Sputtering) is a relatively new highly ionised sputtering technique used to deposit engineering quality thin films, with the advantage that the deposition flux can be guided to the substrate through the electrical biasing. As the technique is on the verge of being adopted by the industries, it is necessary to understand its physics very well so that thin films with tailored properties can be deposited. Therefore, time-resolved diagnostic studies have been carried out to get better physical insight of the HiPIMS processes.

This thesis focuses on time resolved diagnostic study of HiPIMS discharges.

Ion energy distribution function (IEDF) is an important discharge parameter, responsible for the properties of deposited thin films. Therefore, a technique to get IEDF with very high temporal resolution (1 μs) has been developed for the HiPIMS discharges. The excellent agreement between the summation of all the time-resolved IEDFs at different times during the pulse and a time-averaged IEDF recorded by mass spectrometer demonstrated that this technique is quite suitable for very high time-resolved measurements of IEDFs in the HiPIMS discharges.

Plasma potential (V_P) is crucial paramcter that determines the plasma dynamics. Therefore, using an emissive probe the temporal evolution of V_P has been investigated in the HiPIMS discharge pulsed at 100 Hz. The 20 ns time-resolution of the probe allowed us to observe the highly dynamic nature of V_p. The emissive probe results show that for over 50 % of the 100 μs plasma "on-time" the spatial structure of V_p provides a large potential barrier for the sputtered ionised species so impeding their transport and lowering the deposition at the substrate.

The experiments were also carried out to investigate how the deposition rates in HiPIMS, DC and pulsed DC magnetron discharges depend upon the magnetic field strength of the magnetron. A deposition rate monitor has been used to measure the deposition rate at four magnetic field

strengths. For HiPIMS discharges, the results show that the deposition rate increases by a factor of 2 as the magnetic field strength at the cathode is reduced by only ~ 45%. However, in DC and pulsed DC discharges the deposition rates decreased by ~ 35% for the same reduction in the magnetic field strength.

A simple computational model of the sputter rates based on the voltage and current waveforms and energy dependent sputter yields predicts decreasing deposition rates for reduced B-fields, in-line with the DC and pulsed DC mode results. However, it shows the opposite trends to the measurements in the HiPIMS mode. This discrepancy between predicted and experiment for HiPIMS has been explained on the basis that the transport of the post-ionised sputtered atoms, which form the deposit, are affected by the potential structure in the discharge, itself modified by the magnetic field strength.

"A candle burns itself to give light for all around it".

Thesis dedicated

To my Father

ACKNOWLEDGEMENTS

It is really great pleasure to thank many people who made this thesis possible.

First and foremost I would like to extend my deep and sincere gratitude to my supervisor Prof. James W Bradley for his guidance, valuable advices and encouragement. He has always been a source of encouragement and shared his expertise and research insights. He always motivated and provided the opportunities for attending numerous national and international conferences. I am especially thankful to him for spending his valuable weekends and nights in correcting my papers and thesis.

I am thankful to Engineering and Physical Science Research Council (EPSRC) and Overseas Research Students Award Scheme (ORSAS), without their financial support, this study could not have been undertaken.

I owe my gratitude to Prof. Peter J Kelly, Manchester Metropolitan University, for allowing me to work in his laboratory and providing the valuable feedback on my experimental findings.

I am very much thankful to Dr. G C B Clarke who helped in numerous ways and was always available when I needed him.

I warmly thank Dr. Paul Bryant who has made available his support in troubleshooting the experimental set-up and fruitful discussions.

I am indebted to all of my colleagues Dr. Paul Eden, Dr. Savarnos, Dr. Robert Dodd, Shao Dong You, Nu, Leibig Bernd, Dr. Jun Seok, Dr. Glen West and Paul Barker for their friendly help and valuable discussion.

My thank goes to Mr. Alan Roby, workshop engineer, who was always ready to help in designing new tools for my experiments.

Acknowledgements

I am grateful to Mr. Alan Edwards and Mr. John for their support in designing and fabrication of the electronic circuits inevitable for my experiments.

I am very grateful to Prof Dhiraj Bora, Prof Prabal Chattopdhyay, Prof Amita Das, Dr. P K Sharma, and Dr. Joydeep Ghosh for their able guidance, teaching, fruitful discussion and their help during my days in Institute for Plasma Research, India.

This whole of the venture will not be successful without the blessings of parents. I am thankful to my parents and in-laws for their constant emotional and moral support.

This acknowledgement would not be complete without showing my gratitude to my siblings Vidhya Bhoosan, Anushuiya, Avinash, Sandhya, Avadhesh, Richa and Priyanka for providing me all kind of support during my whole study.

Chatting with Parth, Janhvi, Dev and Pari was always like a fresh breeze in hot summer. I am thankful to these little angles who always supplied energy to overcome ups and downs during the course of my thesis via their blissful smiles.

I would like to extend my gratitude to Pooja and Brijesh who were always there for all type of support. I am also thankful to Devendra who spent his precious hours and hours in proof reading of my manuscript.

On a personal note I would like thank to my wife, Dr. Preeti, for her constant and all kind of support, advice, working continuously for 30 hours during formatting. Without her support, this thesis could not have been written.

Last but not the least I would like to thank almighty god for giving me the grace, strength during the Ph.D program. Thank you Lord!

CONTENTS

Declaration i

Abstract ii

Dedication iv

Acknowledgements v

List of Figures xiii

Publications xviii

Presentations xx

Chapter 1 – INTRODUCTION

1.1 Depositional Techniques 1

1.1.1 Chemical Deposition 1

1.1.1.1 Electroplating 1

1.1.1.2 Chemical Solution Deposition 1

1.1.1.3 Chemical Vapour Deposition 1

1.1.1.4 Plasma Enhanced Chemical Vapour Deposition 1

1.1.2 Physical Deposition 1

1.1.2.1 Thermal Evaporation 1

1.1.2.2 Pulsed Laser Deposition 1

1.1.2.3 Cathodic Arc Deposition 1

1.1.2.4 Sputtering 1

1.1.3 Present Research Study and its Context 3

1.2 Plasmas 4

1.2.1 Basics of Plasmas 7

1.2.1.1 Quasi-neutrality 7

1.2.1.2 Collective Behaviour 7

1.2.1.3 Plasma Frequency 8

Contents

1.2.1.4 Plasma and Floating Potential....9
1.2.2 Sheaths in Plasmas....11
1.2.3 Guiding Centre Drifts....16

1.3 Sputtering....1.3

1.3.1 Conventional DC Sputtering....22
1.3.2 Magnetron Sputtering....23
1.3.3 Magnetron Operation....26
1.3.4 Pulsed Magnetron Sputtering....27
1.3.5 High Power Impulse Magnetron Sputtering....29
1.3.6 Purpose of this Study....30

Chapter 2 – EXPERIMENTAL SET-UP

2. Experimental Set-up....32

2.1 Vacuum Chamber and Pumping System....32
2.2 The Magnetron Sputter Source....34
2.3 Power Supplies....37

Chapter 3 – DIAGNOSTIC TOOLS

3. Diagnostic Tools....42

3.1 The Emissive Probe....42

3.1.1 Principal of Operation....42
3.1.2 Emissive Probe in Magnetron Plasmas....44
3.1.3 Time Response of Emissive probe....45
3.1.4 Probe Construction and Calibration....46

3.2 Power Density Probe 48

3.2.1 Techniques to measure Power Density on Substrate 48
3.2.2 Power Density Balance onto Substrate 49
3.2.3 Calorimetric method 50
3.2.4 Design and Calibration of Probe 51

3.3 Energy Resolved Mass Spectrometry 53

3.3.1 Principle of operation 54
3.3.2 Electrostatic Ion Shuttering Technique 56

3.4 Thin Film Deposition Monitor 59

3.5 Langmuir Probe 61

3.5.1 Langmuir Probe Theory 62
3.5.2 Langmuir Probe in Non Maxwellian Plasmas 66
3.5.3 Langmuir Probe in Pulsed Plasma 68
3.5.4 Practical Considerations in Designing Langmuir Probe 69
3.5.5 Designing and Fabrication of Langmuir Probe 69
3.5.6 Automated Langmuir Probe System 71

Chapter 4 – PLASMA POTENTIAL MEASUREMENTS

4. Plasma Potential Measurements 73

4.1 Evolution of Plasma Potential in One-dimension 73

4.1.1 Introduction 73
4.1.2 The Experimental Arrangement 77
4.1.3 Results and Discussion 83
4.1.3.1 Loop Current versus Floating Potential 83
4.1.3.2 Plasma Potential versus Probe Plane Orientation 85
4.1.3.3 Evolution of Plasma Potential 86

4.1.3.3.1 Axial Distribution in Plasma Potential....................................87
4.1.3.3.2 Temporal Evolution of Electric Field in Bulk Plasma............91
4.1.3.3.3 Spatial-Temporal Evolution of Plasma Potential.................... 93
4.1.3.3.4 Relationship between Plasma Potential, Magnetic Field Strength and Deposition Rate 100
4.1.4 Conclusions 105

4.2 Evolution of Plasma Potential in Two Dimension and E × B Drifts................106

4.2.1 Introduction 106
4.2.1.1 E × B Drifts in Magnetron Discharges...108
4.2.2 Experimental Arrangement..111
4.2.3 Results and Discussion 112
4.2.3.1 Two-dimensional Plasma Potential Evolution...................................114
4.2.3.2 Evolution of Axial and Radial Electric Fields...................................119
4.2.3.3 E × B Drifts Velocities...122
4.2.4 Conclusions...124

Chapter 5 – POWER DENSITY MEASUREMENTS ONTO SUBSTARTE

5. Power Density Measurements onto Substrate..126

5.1 Introduction...126

5.1.1 Hysteresis Effect...128

5.2 Experimental Arrangement..130

5.2.1 Experimental Set-up at Manchester Metropolitan University..................130
5.2.2 Experimental Set-up at Liverpool University...131

5.3 Results and Discussion...132

5.3.1 Metallic Mode...132

5.3.1.1 Power Density onto the Floating Substrate 132
5.3.1.2 Axial variation of the Heat Flux onto the Substrate............................ 136
5.3.1.3 Deposition rate and substrate heating in HiPIMS, DC and pulsed- DC Magnetron Sputtering 138
5.3.2 Reactive Mode 141
5.3.2.1 Effect of Magnetic Field on the Power Density in HiPIMS Discharges.. 141
5.3.3 Langmuir Probe Measurements.. 147
5.3.3.1 The Evolution of Plasma Parameters.. 148

5.4 Conclusions **151**

Chapter 6 –DEPOSITION RATE MEASUREMENTS

6. Deposition Rate Measurements **153**

6.1 Introduction **153**

6.2 Experimental Arrangements **155**

6.3 Results and discussions **159**

6.3.1 Effect of Magnetic Field on Deposition Rates in HiPIMS 160
6.3.2 Effect of Magnetic Field on Deposition Rates in DC and pulsed- DC Magnetron Sputtering... 164
6.3.3 Modelling of the Effect of Magnetic Field Strength on Deposition rates 165

6.4 Conclusions **169**

Chapter 7–MEASUREMENTS OF ION ENERGY DISTRIBUTION FUNCTION IN HiPIMS DISCHARGES

7. Measurements of Ion Energy Distribution Functions in HiPIMS Discharges.......170

7.1 High Time-Resolved IEDFs in HiPIMS Discharges 170

7.1.1 Introduction...170
7.1.2 Experimental Set-up..173
7.1.3 Results and Discussion 174
7.1.4 Conclusions..179

7.2 Temporal Evolution of Ion Bombarding Energy at Substrate Position 180

7.2.1 Introduction...180
7.2.2 Experimental Arrangement 181
7.2.3 Results and Discussion 181
7.2.3.1 Ion energy distribution functions for Ar^+ and Ar^{++} 181
7.2.3.2 Ion energy distribution for Ti^+ and Ti^{++} 184
7.2.4 Conclusions..186

Chapter 8 –DEPOSITION RATE MEASUREMENTS

8. Conclusions and Outlook 187
8.1 Conclusions 188
8.2 Outlook for Future Work 191

REFERENCES.. 193

LIST OF FIGURES

Chapter 1 – INTRODUCTION

1.1 Current-Voltage (I-V) Characteristics of Langmuir Probe........10
1.2 Sheath and pre-sheath formed in-front of the floating substrate........12
1.3 Schematic of E × B drift speeds for electron and ion........18
1.4 Schematic representation of various processes occurring on the surface when an energetic particle incidents........20
1.5 Probability distribution of an atom to be sputtered against the energy of incident ion........22
1.6 Schematic view of the target face of a circular planar magnetron........25
1.7 Schematic of balanced and unbalanced magnetron (Type II)........26

Chapter 2 – EXPERIMENTAL SET-UP

2.1 The schematic of the experimental set-up........33
2.2 A schematic diagram of the magnetron source, the B-field lines, the emissive Probe , the deposition rate monitor........35
2.3 Magnetic field strength for the 4 different magnet positions behind the cathode...36
2.4 Magnetic field strenght and field line directions for magnetic field configuration1........37
2.5 The cathode voltage (V_d) and current (I_d) waveforms produced by the SINEX 3.0 HiPIMS power supply........39
2.6 Typical cathode voltage and current pulse waveforms in pulsed DC of 100 kHz........40
2.7 Typical cathode voltage and current pulse waveforms in pulsed DC of 350 kHz. Duty factor was 50% and average power was 680 W........41

Chapter 3 – DIAGNOSTIC TOOLS

3.1 Plasma potential waveform in HiPIMS discharge with the cathode voltage........45
3.2 The schematic diagram of the emissive probe........46

3.3 Schematic of electrical and measuring circuitry of the emissive probe......................47
3.4 Schematic of various contents of the heat flux incident onto the substrate.................49
3.5 Schematic of the heat flux probe...52
3.6 Schematic of mass spectrometry with electrostatic gate to get high time-resolved measurements..54
3.7 Schematic of the electrostatic ion shuttering technique..56
3.8 Schematic of the pulsing scheme applied to ion shutter 57
3.9 Plot of Ar^+ IEDFs collected by utilizing the electrostatic ion shuttering technique with 2 μs time resolution..58
3.10 Picture of the deposition rate monitors TM400..59
3.11 A picture of the deposition rate monitors TM400 read out......................................60
3.12 A schematic of Langmuir probe used in this study..70

Chapter 4 – PLASMA POTENTIAL MEASUREMENTS

4.1 The measured magnetic field (flux density B) and field line directions for magnetic field configuration 1..79
4.2 The measured magnetic field (flux density B) and field line directions for magnetic field configuration 2..80
4.3 The measured magnetic field (flux density B) and field line directions for magnetic field configuration 3..80
4.4 The total B-field $|B| = \sqrt{(B_z^2 + B_r^2)}$ for the 3 different magnet positions behind the cathode..81
4.5 The cathode voltage (V_d) and current (I_d) waveforms produced by the SINEX 3.0 HiPIMS power supply...82
4.6 A plot of the time-evolution of typical plasma potential (V_p)...................................83
4.7 A plot of measured emissive probe floating potential (V_f) versus loop heat current..84
4.8 The time evolution of the emissive probe floating potential at r = 45 mm versus probe loop orientation angle θ...86
4.9 Plot of V_p versus axial distance z from the cathode "first peak" phase.....................87
4.10 Plot of V_p versus axial distance z from the cathode for "second peak" phase...........88
4.11 Plot of v_p versus axial distance z from the cathode for "off phase" phase.................89

4.12 Plot of the temporal-evolution of the mean axial electric field strength (E_z)............92

4.13 Contour plot of the spatial-temporal evolution of the V_p at a pressure of 0.54 Pa and an average power of 650 W..........94

4.14 Contour plot of the spatial-temporal evolution of the V_p at a pressure of 1.08 Pa and an average power of 650 W..........95

4.15 Contour plot of the spatial-temporal evolution of the V_p at a pressure of 1.08 Pa and an average power of 950 W..........97

4.16 A plot of V_p versus axial distance z from cathode at the time when "first peak" occurs..........102

4.17 A plot of V_p versus axial distance z from cathode at the time when the peak in the discharge current (I_d) occurs at an average discharge power of 750 W, a gas pressure of 1.08 Pa and above the racetrack (r = 45 mm)..........102

4.18 Plot of titanium deposition rate measured at an average discharge power of 750 W and the gas pressure of 1.08 Pa..........103

4.19 Schematic of magnetron source..........112

4.20 Plot of measured emissive probe floating potential (V_f) versus loop heat current..........113

4.21 Plot of the time-evolution of typical plasma potential with cathode discharge voltage..........114

4.22 Contour plot of the plasma potential at " first peak" phase..........116

4.23 Contour plot of the plasma potential at "second peak" phase..........117

4.24 Contour plot of the plasma potential at the t= 30 μs..........118

4.25 Plot of the derived radial electric field at "first peak" phase..........120

4.26 Plot of the derived axial electric field at "first peak" phase..........121

4.27 The plots of the E × B Drift speeds in 'first peak' condition..........122

4.28 The distribution of E × B drifts velocities..........123

Chapter 5 – POWER DENSITY MEASUREMENTS ONTO SUBSTARTE

5.1 Schematic illustration of partial pressure as a function of reactive gas flow rate..........129

5.2 Schematic of the experimental set-up used to measure the power density and the deposition rate..........131

5.3 Plot of temporal evolution of the probe temperature in heating and cooling phase....133
5.4 Plot of the heat flux density versus average power onto the isolated substrate in DC mode....134
5.5 Plot of the heat flux density versus average power onto the isolated substrate in HiPIMS mode.... 135
5.6 Plot of the heat flux density versus average pulse frequency onto the isolated substrate in pulsed DC mode....135
5.7 Plot of axial profile of heat flux density onto the isolated substrate in HiPIMS, DCMS and pulsed DCMS discharges....136
5.8 Plot of the measured deposition rates in HiPIMS discharge....139
5.9 Normalized heat flux density for equivalent deposition rates in dc HIPIMS and pulsed-dc modes....140
5.10 Plot of the cathode voltage waveforms at different flow rates of oxygen....141
5.11 Plot of the cathode current waveforms at different flow rates of oxygen....142
5.12 The measured magnetic field (flux density B) and field line directions for (a) magnetic field configuration 1....143
5.13 The total B-field has been caluclated as $|B| = \sqrt{(B_z^2 + B_r^2)}$ for all the four locations of magnets....144
5.14 The cathode voltage V_d and current I_d waveforms produced by the SINEX 3.0 supply in the HiPIMS mode for four magnetic field configuration....145
5.15 Plot of heat flux densities verses magnetic field strengths in HiPIMS....146
5.16 Evolution of electron energy distributions (EEDF) in bulk plasma (Z = 88 mm) at 40 μs (on-time) and 150 μs (off-time)....149
5.17 Plot of time-resolved plasma density profile in bulk plasma (Z = 88 mm) at two different magnetic field configurations (BF1 and BF3)....149
5.18 Plot of time-resolved electron plasma temperature profile in bulk plasma (Z = 88 mm) at two different magnetic field configurations (BF1 and BF3)....151

Chapter 6 –DEPOSITION RATE MEASUREMENTS

6.1 The cathode voltage V_d and current I_d waveforms produced by the SINEX 3.0 supply in the HiPIMS in all the four magnetic field configuration....157

6.2 The cathode voltage V_d and current I_d waveforms for100 kHz pulsed DC mode in all the four magnetic field 158
6.3 The cathode voltage V_d and current I_d waveforms for350 kHz pulsed DC mode in all the four magnetic field configuration 158
6.4 A plot of deposition rates versus magnetic field strength in the HiPIMS, DC and Pulsed DC modes 162
6.5 A plot of the deposition rates against the magnetic field strength in the DC and pulsed DC modes 167
6.6 A plot of the deposition rates against the magnetic field strength in HiPIMS 168

Chapter 7–MEASUREMENTS OF ION ENERGY DISTRIBUTION FUNCTION IN HiPIMS DISCHARGES

7.1 Schematic of experimental set-up used for IEDFs measurements 173
7.2 Plot of the IEDF in HiPIMS discharges for Ar^+ 175
7.3 Plot of time averaged IEDF for Ar^+ and the summation of all the time-resolved IEDFs in the same time window 176
7.4 Plot of time resolved IEDFs measurements in Ar^+ in the HiPIMS discharges with the time-resolution is of 2 μs 178
7.4 Plot of time resolved IEDFs measurements in Ti^+ in the HiPIMS discharges with time-resolution is of 2 μs 178
7.5 Plot of IEDFs of Ar^+ with 10 μs time-resolution 181
7.6 Plot of IEDFs of Ar^{++} with 10 μs time-resolution 182
7.7 A plot of IEDFs of Ti^+ with 10 μs time-resolution 183
7.8 A plot of IEDFs of Ti^{++} with 10 μs time-resolution 185

PUBLICATIONS

1. **Substrate heating and deposition rate measurements in a HiPIMS discharge**
   51st Society of vacuum coaters Annual Conference, 2008, Chicago, IL
   G. T. West, P. Barker, *A. Mishra*, G. C. B. Clarke, P. J. Kelly and J. W. Bradley

2. **High temporal resolution IEDF in HiPIMS discharge**
   Plasma Processes and Polymers, 2009, 6, S610
   Anurag Mishra, Gregory Clarke, P. J. Kelly and J.W. Bradley

3. **Experimental measurements of cathode current density distributions and optical imaging of HiPIMS discharge**
   Plasma Processes and Polymers, 2009, 6, S548
   Gregory Clarke, *Anurag Mishra*, J.W. Bradley and P.J. Kelly

4. **Measurements of deposition rate and substrate heating in HiPIMS discharge**
   Plasma Processes and Polymers, 2009, 6, S 543
   Glen West, Peter Kelly, Paul Barker, *Anurag Mishra*, James Bradley

5. **The temporal evolution of the ion bombarding energy at the substrate in a HiPIMS discharge**
   ICPIG, 2009, Cancun, Mexico
   Anurag Mishra, P. J. Kelly and J .W. Bradley

6. **Ion energy and plasma potential measurements in HiPIMS discharges**
   52nd Society of vacuum coaters Annual Conference, 2009, Santa Clara, CA
   Anurag Mishra, P. Poolcharuansin, P. J. Kelly and J .W. Bradley

7. **The evolution of the plasma potential in a HiPIMS discharge and its relationship to deposition rate**

   Plasma Sources Science and Technology, 2010, 19, 045014

   Anurag Mishra, P.J. Kelly and J.W. Bradley

8. **The comparative study of effect of magnetic field on deposition rates in HiPIMS, pulsed DC and DC discharge**

   In communication with Surface Coating Technology

   Anurag Mishra, P.J. Kelly and J.W. Bradley

9. **2D Spatial survey of plasma potential and electron drifts in HiPIMS discharge**

   Manuscript writing

   Anurag Mishra, P. J. Kelly and J.W. Bradley

10. **Magnetic field effect on the pre-sheath dynamics in HiPIMS discharge**

    53rd SVC-2010, Orlando, USA

    Anurag Mishra, P. J. Kelly and J.W. Bradley

PRESENTATIONS IN CONFERENCES AND MEETINGS

1. Poster Presentation in IOP Annual meeting 2008, London
   Measurement of Energy Flux on Isolated Substrate in High Power Impulse Plasma Magnetron Discharge
   Anurag Mishra, P.J. Kelly and J.W. Bradley

2. Paper Presentation in PGR-2008, Department of Electrical Engineering and Electronics, University of Liverpool
   Plasma potential measurements in Pulsed Magnetron Discharge
   Anurag Mishra and J. W. Bradley

3. Paper presentation in HIPIMS meeting, MMU, UK, 11th March, 2008
   Measurement of thermal flux in HIPIMS discharge
   Anurag Mishra, G. C. B. Clarke and J .W. Bradley

4. Paper presentation in 51st Annual technical conference society of vacuum coaters, 2008 , Chicago, IL, USA,
   Substrate heating and deposition rate measurements in a HiPIMS discharge
   G. T. West, P. Barker, *A. Mishra*, G. C. B. Clarke, P. J. Kelly and J. W. Bradley

5. Presentation in 7th International Conference on Coatings on Glass and Plastics, 15 – 19 June, 2008, Eindhoven, Netherlands
   P Barker, G West, D Ochs, P Ozimec, J W Bradley, P. J. Kelly, ***A Mishra***, A .G Spencer

6. Paper Presentation in PSE 2008, Germany
   A technique for obtaining high temporal resolution ion energy distribution functions in pulsed plasma environments
   Anurag Mishra, Gregory Clarke, James Bradley, Peter Kelly

Presentations

7. Paper Presentation in PSE (Plasma Surface Engineering) 2008, Germany
   Measurements of deposition rate and substrate heating in HIPIMS Discharge
   Glen West, Peter Kelly, Paul Barker, *Anurag Mishra*, James Bradley

8. Paper Presentation in PSE (Plasma Surface Engineering) 2008, Germany
   Experimental measurements of cathode current density distributions and optical imaging of HIPIMS discharge
   Gregory Clarke, *Anurag Mishra*, Peter Kelly and J. W. Bradley

9. Oral presentation in HiPIMS meeting, 30th September 2008,
   Oxford University, UK
   Development of time-resolved diagnostics for HiPIMS discharge
   Anurag Mishra, P. J. Kelly and J. W. Bradley

10. Oral presentation in Research Student Seminar, 8th Oct, 2008
    Department of Electrical Engineering and Electronics,
    University of Liverpool, UK
    HiPIMS: - A new Route to High Performance Films on Polymeric Web
    Anurag Mishra

11. Oral presentation in Technological Plasma Workshop, 2008, Milton Keynes, UK
    Temporal evolution of Ion Energy Distribution Functions (IEDF) in HiPIMS Discharge
    Anurag Mishra, P.J. Kelly, J .W. Bradley

12. Oral presentation in Interdisciplinary forum, University of Liverpool
    Plasma research and creation of wealth, 2008
    Anurag Mishra

13. Oral presentation in 3rd MPE – UL collaboration meeting on Complex and technological plasmas, 25 – 27 March, 2009, Liverpool, UK
Spatial – temporal evolution of plasma potential in HiPIMS discharge
Anurag Mishra, P. J. Kelly, J.W. Bradley

14. Oral presentation in SVC conference 2009, Santa Clara, California, USA
Ion energy and plasma potential measurements in HiPIMS discharges
Anurag Mishra, P. Poolcharuansin, P.J. Kelly and J.W. Bradley

15. Oral presentation at ICOPS, IEEE Conference on Plasma Sciences,1-5 June, 2009, San Diego California, USA
Spatial and Temporal Evolution of plasma potential in HiPIMS discharges
A Mishra, J.W. Bradley and P.J. Kelly

16. Poster presentation in July 2009, ICPIG, Cancun, Mexico
The temporal evolution of the ion bombarding energy at the substrate in a HiPIMS discharge
Anurag Mishra, P. J. Kelly and J .W. Bradley

17. Oral presentation, University of Oxford, UK on 20th Oct, 2009
The evolution of plasma potential in a HiPIMS discharge and its Relationship with deposition rate
Anurag Mishra, P. J. Kelly and J .W. Bradley

18. Oral presentation in Technological Plasma Workshop, 2009 Glasgow, UK
Emissive probe measurements of the plasma potential in HiPIMS discharge
Anurag Mishra, P.J. Kelly and J.W. Bradley

19. Oral presentation at 5th Mikkeli International Industrial Coating Seminar MIICS, 17th to 19th March, 2010 at Mikkeli, Finland
    Applications of High Power Impulse Magnetron Sputtering (HiPIMS)
    G .T. West, P. J. Kelly, P Barker, J.W. Bradley and *A Mishra*

20. Poster Presentation in IOP Annual meeting 29 March – 1 April, 2010, Windermere, UK
    Magnetic field effect on pre-sheath dynamics in a High Power Impulse Magnetron Sputtering Discharge
    Anurag Mishra, P.J. Kelly and J.W. Bradley

21. Oral presentation in HPPMS/HiPIMS/MPP Workshop on 23rd April, 2010 in Colorado School of Mines, Colorado, USA
    HiPIMS Deposition of Metal and Oxide Coatings
    G.T. West, P. J. Kelly, J.W. Bradley, P.M. Barker, *A Mishra*

22. 2nd Research Staff Conference, 6th May, 2010, University of Liverpool, UK

23. Poster presentation in IOP annual meeting on Plasma, Surfaces and Thin Films 16 June, 2010, London, UK
    Time evolution of plasma potential in HiPIMS discharge
    Anurag Mishra, P.J. Kelly and J .W. Bradley

24. Poster presentation in 1st international conference on HiPIMS discharges,6th-7th July 2010, Sheffield, UK
    Comparative study of magnetic field effect on the deposition rates in HiPIMS, DC and pulsed DC discharges
    Anurag Mishra, P. J. Kelly and J .W. Bradley

Presentations

25. Oral presentation in HiPIMS meeting, 16 July, 2010, Oxford U.K.
    Time-resolved Langmuir probe measurements
    Anurag Mishra, P. Barker, G. West, P. J. Kelly and J .W. Bradley

26. Oral presentation in 12th International conference on PSE (Plasma Surface Engineering Conference), 2010, Garmisch , Germany
    A comparative study of effect of magnetic field on the deposition rates in a HiPIMS, DC and pulsed DC discharges
    Anurag Mishra, P.J. Kelly and J.W. Bradley

27. Talk in LPP, Ecole Polytechnique, 18thNovember, 2010, Paris France
    Time-resolved diagnostics study of HiPIMS discharges
    Anurag Mishra

Chapter 1

INTRODUCTION

Plasma discharges are extensively used to deposit engineering quality thin-films and to modify the surface properties such as optical, mechanical, electrical and chemical [1-4]. For instance, corrosive properties of tools can be altered by the application of thin- films having very high level of wear resistance and hardness [5]. One important approach to produce optical films is depositing multiple layers having different optical frequency response of films. This can be used in the solar panels.

1.1 Depositional Techniques

There are numerous ways to deposit the thin-films such as:-

1.1.1 Chemical deposition

1.1.1.1 Electroplating [6]

1.1.1.2 Chemical Solution Deposition (CSD) [7]

1.1.1.3 Chemical Vapour Deposition (CVD) [8]

1.1.1.4 Plasma Enhanced Chemical Vapour Deposition (PECVD) [8]

1.1.2 Physical Deposition

1.1.2.1Thermal Evaporation [9]

1.1.2.2. Pulsed Laser Deposition [10]

1.1.2.3 Cathodic Arc Deposition (arc-PVD) [9]

1.1.2.4 Sputtering [8]

Sputtering is the most important method and widely used in industries to deposit engineering quality thin-films. It is a phenomenon whereby the atoms of a material are ejected by the bombardment of energetic particles. In the basic sputtering process, a target (or cathode) plate is bombarded by energetic ions generated in glow discharge plasma, situated in front of the target. The bombardment process causes the removal, i.e., sputtering', of target atoms, which may then condense on a substrate as a thin film [11]. Further efficiency of the sputtering process can be greatly enhanced by applying a magnetic field. This modified technique is known as **Magnetron Sputtering** [12]. The efficiency and applicability of this technique in the production of insulating films can be further enhanced by using this technique in pulsed mode [13-15]. Pulsing the applied voltage removes the problem of arcing and produces the better quality thin films.

Energy input per depositing species on the substrate is a crucial parameter that determines properties of thin films deposited. A relatively new magnetron technique that utilizes an application of short and intense voltage pulses on cathode greatly enhances the proportion of the ionized sputtered metal flux. This technique is known as **High Power Impulse Magnetron Sputtering (HiPIMS)**. The details of this technique will be discussed in later chapter.

1.1.3 Present Research Study and its Context

Functional thin films are finding many applications in modern technology from integrated circuits to thermal barrier coatings, electronic and opto-electronic devices, flat panel displays, electro-chromatic coatings, Organic Light Emitting Diodes (OLEDs), image sensors and thin- film photovoltaic solar cells etc [16, 17]. Moreover, flexible polymers substrates are being increasingly used in the place of rigid glass substrates due to their reduced weight, reduced cost and increased durability. In all the thin-film deposition, device performance is directly linked to the quality of individual layers deposited. However, the thin films deposited onto polymeric webs pose many significant technological challenges; one of them is relatively more thermal sensitivity of polymeric web compared to that of rigid glass substrate. This fact of thermal sensitivity, poses a significant problem because it is generally necessary to perform a post deposition annealing process (typically 500^0C) in order to optimize the optical and electrical properties and to reduce the stress of the thin- films. The high power impulse magnetron sputtering (HiPIMS), a relatively new ionized physical vapour deposition (IPVD) technique introduced by Kouznetsov et. al. [18] in 1999 and might be a potential solution to this problem as it shows to have less heating effect on the substrate.

As HiPIMS technology is above its adolescence and about to be adopted by industries, it is timely to understand better the physical processes occurring inside the discharge so that the discharge properties can be optimized. This can be accomplished by a systemic study of the spatial and the temporal evolution of various plasma parameters and their dependence on different operational conditions such as average

and peak power density, pressure, average and peak discharge current density, pulse frequency, pulse width, magnetic field strength and the cathode material etc. All these parameters, known as global parameters, determine the discharge properties that, in turn, determines the properties of thin-film deposited. As, the ability to produce and maintain a plasma is essential to the operation of a magnetron, substantial research has also been carried out investigating intrinsic properties of such plasmas, and how these are affected by global parameters [19-25]. Further investigations have also been attempted to link the properties of thin-film deposited to the plasma parameters [26].

The present experimental study is an attempt to provide in-depth and better understanding of physical processes occurring in the discharge. To accomplish this, several detailed experimental studies have been carried out such as temporal evolution of ion bombarding energy on the substrate, spatial temporal investigation of the plasma potential, deposition rate measurements and magnetic field effects on the substrate heating. The various aspect of this experimental study such designing the diagnostics and interpreting of various experiments findings will be discussed in the later chapters.

1.2 Plasmas

This section discusses the fundamental properties of the plasma state, describes some basic phenomena occurring within it, and, then, addresses those, which are relevant to magnetron sputtering operations. A more detailed description of plasmas can be found

in text books such as Chen [27], Liebermann and Lichtenberg [8], Konuma [28], Huddlestone and Leonard [29] and Chapman [30].

Plasma, an ionized state of matter, is essential for any depositional process such as magnetron sputtering deposition. The fluid like properties of the plasmas is derived from the long range interaction among the charged particles. Plasma, composed of charged particles, interacts with the electric and the magnetic fields and support flows, waves, self-organization and instabilities.

Plasma can be ignited by the application of a potential difference across a low-pressure gas. This applied potential difference exerts an electrical force on the free electrons (produced due to interaction of cosmic rays with the gas) present in the gas. These electrons travel through the gas volume, collide with the gas atoms and ionize them. If the gas becomes sufficiently ionized, plasma may form, and current can flow between the electrodes. Plasmas consist of ions (either positively or negatively charged), electrons, neutrals, free radicals, molecules and photons. For a simple description of the plasmas, in the absence of electro-negative gases, it can be assumed that the plasmas are made only of the positive ions, electrons and neutrals. Based on an assumption of large number of electron-electron collisions and other interactions, and very efficient energy sharing among the electrons, a Maxwell-Boltzmann distribution seems quite reasonable to describe the plasmas and, then, an electron temperature T_e can be associated with each electron. The energy of these constituent electrons often expressed as a temperature [30, 31, 32] by assuming:

$$kT_e = eV \qquad eq\ (2.1)$$

where k is Boltzmann's constant (1.38 x 10^{-23} JK $^{-1}$), T_e is temperature (Kelvin), e is the electronic charge (1.6 x 10^{-19} Coulomb) and V is voltage (V). Applying this formula, energy of 1 eV is equivalent to a temperature ~11600 K. The gas neutrals, in the magnetron discharges, are usually close to or above room temperature (290 K) and therefore have the effective energy equivalent to 0.025 eV. The plasma ions, due to their heavier mass than electrons, are less influenced by the electric fields and therefore may have a temperature, T_i, equivalent to energies from the fraction of eV to several eV and temperature different from electrons' temperature [30, 32]. It essentially means that the electrons and ions in the magnetron plasmas may not be in thermal equilibrium (i.e. $T_i \neq T_e$).

The typical range of plasma densities during the conventional magnetron sputtering ranges from 10^{15} to 10^{17} m^{-3} [33, 34]. Depending upon the pressure regime of the magnetron operation that is typically between 0.1 and 10 Pa, the neutral gas density varies from 10^{19} to 10^{21} m^{-3} [18]. This results in ionization fractions between 10^{-2} and 10^{-5}. However, in HiPIMS, a relatively new PVD technique, plasma densities up-to 10^{19} m^{-3} are achieved. Therefore, the ionization fraction obtained during the HiPIMS processes is significantly higher compared to conventional magnetron sputtering. These facts present in the magnetron discharges make it categorized as typically cold, low-density, non-thermal equilibrium plasmas, when compared to, for instance, those produced within a Tokamak – a fusion reactor [27].

1.2.1 Basic of Plasmas

Every ionized gas is not plasma. For an ionized gas to be in plasma state, the number of charged particles in a Debye sphere should be very large compared to 1 and the following conditions must be satisfied:

1.2.1.1 Quasi-neutrality

Quasi-neutrality means that the electrical nature of the bulk discharge should be neutral, meaning that the electron and ion densities should be approximately the same. Typically, it differs by 1 in 10^6 particles. The electron plasma density is denoted by n_e and called as plasma density [27]. The departure from this quasi-neutrality condition produces the short-range electric fields within the plasmas that occur over the short distances, known as Debye length (λ_D), which is given [27],

$$\lambda_D = \sqrt{\frac{kT_e}{4\pi n_e{}^2}} \qquad eq.(2)$$

where k is the Boltzmann constant (1.38×10^{-23} JK^{-1}) and T_e is the electron temperature (K).

1.2.1.2 Collective behavior

The charged particles within the plasma must be close enough together so that each particle influences many nearby charged particles, rather than just interacting with the

closest. This characteristic of plasma is known as the collective behavior and it is valid when the number of charge particles within the sphere of influence (known as the *Debye sphere* whose radius is the Debye length) of a particular particle are higher than unity. The average number of particles in the Debye sphere is given by the plasma parameter, "Λ" – a dimensionless quantity, which is equal to the typical number of plasma particles in a Debye sphere [8],

$$\Lambda = 4\,\pi\,n\,\lambda_D^{\,3} \qquad \text{eq. (2.3)}$$

where λ_D is the Debye length. An alternative definition of the plasma parameter is given by the average number of electrons in plasma contained within a Debye sphere N_D. Therefore [27],

$$N_D = \frac{4\pi}{3} n \lambda_D^3 \qquad eq. (2.4)$$

where n is plasma density For plasmas to exist, N_D must be very greater than unity i.e. $N_D >>> 1$.

1.2.1.3 Plasma frequency

The electron plasma frequency (the natural frequency of electrons) should be large compared to the electron-neutral collision frequency (frequency of collisions between electrons and neutral particles). When this condition is valid, electrostatic interactions dominate over the processes of ordinary gas kinetics.

1.2.1.4 Plasma and Floating potential

When an electrically floating probe is suspended into the plasma, it will start to be charged negatively, due to the higher mobility of electrons than that of ions ($\mu_e >> \mu_i$) - provided by the higher temperature and lower mass of the electron ($T_e > T_i$ and $m_e < m_i$) - compared with those of the ions. Therefore, the substrate gets a negative potential with respect to the plasma. Further accumulation of negative charge leads to a reduction in the flux of electrons, and the development of a region adjacent to the body that is no longer quasi-neutral. This accumulation of the negative charge onto the body continues until sufficient negative charge has been built up so that the flux of ions and electrons to the body are equal i.e. net charge flux to the substrate becomes zero. At this point the body will be at the floating potential, labeled in the figure 1.1 as floating potential.

If an external negative bias is applied that makes the body more negative than the floating potential, the flux of electrons will be reduced further. This will continue as the magnitude of the negative bias is increased, until it is only the ions that arrive at the body. At this point the current measured flowing through the body will consist purely of that carried by the ions, and is referred to as ion saturation current $I_{ion\ sat}$ [1]. Conversely, if the bias is increased above the floating potential, then the body will be subject to an excess arrival of negative charge due to the increasing flux of electrons, and the flow of current will change direction. The current will continue to increase until the total current reaching to the body is made of the electrons only. This current is known as electron

[1] Assuming no emission of secondary electrons

saturation current. The potential acquired by the body at the beginning of electron saturation is known as plasma potential. At this location the density of electrons and ions surrounding the body are equal, but due to their higher mobility, the current measured by the probe consists mostly of that carried by the electrons. Increasing the bias above this value will lead to the ions being repelled and the body taking purely electrons current, as indicated by $I_{electron\ sat}$ in figure 1.1.

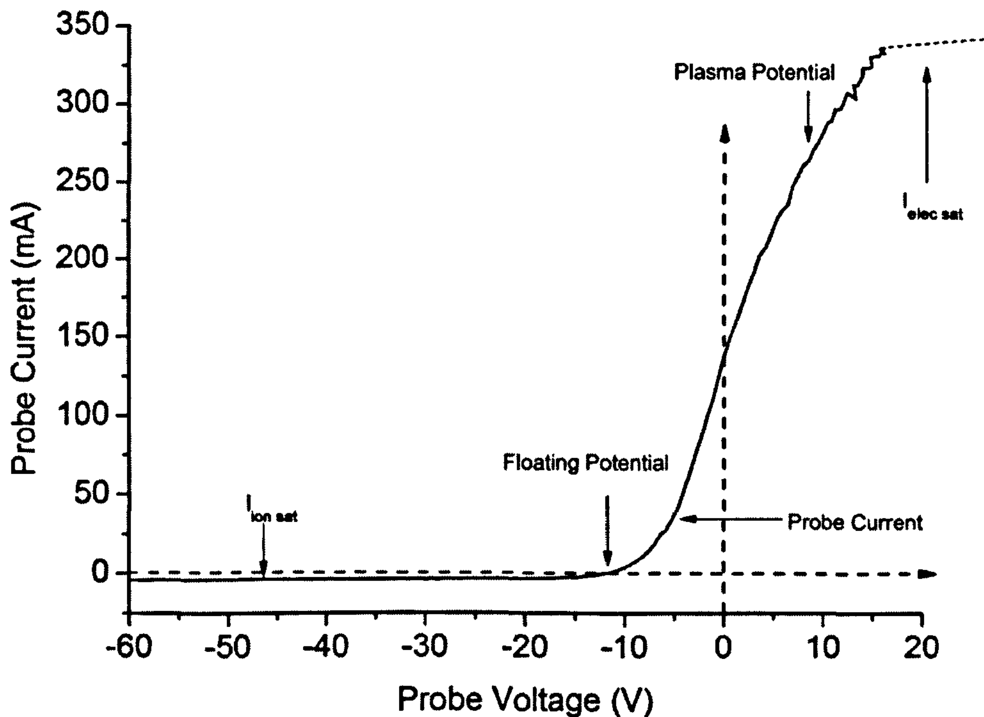

***Figure 1.1**: Current-Voltage (I-V) Characteristics of plasma sampled Langmuir Probe*

This behavior may be observed when using a Langmuir probe, which can be employed to determine the values of N_e, N_i, T_e, V_p and V_f. The details of the Langmuir probe technique will be discussed in later chapter.

1.2.2 Sheaths in Plasmas

When an isolated substrate is immersed into the plasma, the electrons and the ions move towards the substrate. Due to the higher mobility of the electrons, the electron flux to the substrate is greater than the ion flux. It results in the accumulation of negative charge onto the substrate and starts to repel electrons and attract ions. Eventually, it forms a thin layer of positive space charge next to the substrate. This thin layer in the plasma has a greater density of positive ions, and hence an overall excess positive charge, that balances an opposite negative charge on the substrate with which it is in contact. This thin layer is known as plasma sheath as shown in the figure 1.2, where the quasi-neutrality condition breaks down. The thickness of the plasma sheath equals to several Debye lengths, a value whose size depends on plasma parameters such as temperature and density. The structure of the sheath depends upon the potential difference between the substrate and plasma potential and is given by Poisson equation:

$$\epsilon_0 \nabla . E = n_i - n_e \qquad eq. (2.5)$$

Where ϵ_0 is the permittivity of space, n_i and n_e are the ion and electron plasma density respectively.

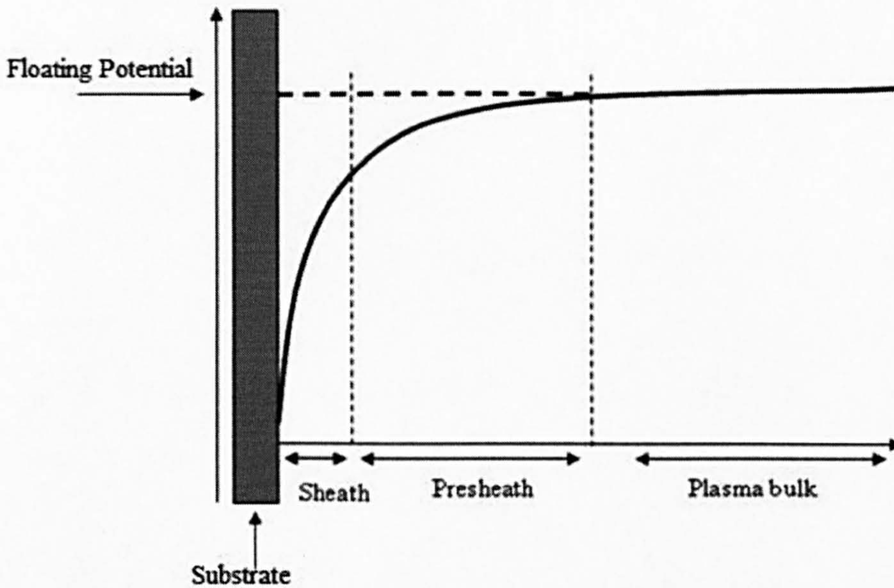

***Figure 1.2**: The plot of sheath and pre-sheath formed in-front of the floating substrate.*

The term $n_i - n_e$ creates a space charge that results in the establishment of an electric field. This electric field balances the flow of the positive and negative charge across the sheath [35]. The ions reaching the sheath boundary from the bulk plasma get accelerated towards the immersed substrate, however most of the electrons are reflected back due to the negative charge build up onto the substrate. Only the highly energetic electrons can overcome this potential barrier created by the negative and the positive charge imbalance near to the substrate.

For a plasma sheath to exist, the Bohm sheath criterion must be satisfied. According to the Bohm Sheath criterion, ions of mass M_i, must enter into the sheath at an ion velocity, v_B [19],

$$v_B = \sqrt{\frac{kT_e}{M_i}} \qquad eq.(2.6)$$

where v_B is the Bohm velocity, M_i is the ion mass and T_e is electron plasma temperature. This Bohm velocity is greater than the ion acoustic velocity (natural velocity of ions). The energy required to accelerate the ions to v_B is provided by an electric field present between the plasma bulk and the sheath in an area known as the pre-sheath. The potential difference across this pre-sheath region is given by [30],

$$\emptyset = \frac{Mv_B^2}{2e} = \frac{kT_e}{2e} \qquad eq.(2.7)$$

Therefore, the plasma density at the sheath edge can be expressed as [30],

$$n_s = n\exp\left(-\frac{e\emptyset}{kT_e}\right) = n\,exp\left(-\frac{1}{2}\right) = 0.61\,n \qquad eq.(2.8)$$

where n is the bulk plasma density.

The thermal velocity of the electrons is

$$v_{th} = \sqrt{\frac{2kT_e}{m_e}} \qquad eq.(2.9)$$

where m_e is the mass of the electron and T_e is the electron plasma temperature.

Considering the sheath thickness as the Debye length λ_D, the electron transit time through the sheath can be expressed as [8],

$$\tau_e \approx \frac{\lambda_D}{v_e} = \sqrt{\frac{\epsilon_0 m_e}{2ne^2}} \qquad eq.(2.10)$$

and the ion transit time [8],

$$\tau_i \approx \frac{\lambda_D}{v_B} = \sqrt{\frac{\epsilon_0 M_i}{ne^2}} \qquad eq.(2.11)$$

These equations are roughly used to determine the frequency response of the electric probes.

Assuming the potential drop outside the sheath is much smaller than the potential drop inside the sheath, Child Law describes the space charge limited current density to the cathode as [30],

$$j_i = \frac{4}{9}\epsilon_0 \left(\frac{2e}{M}\right)^{\frac{1}{2}} \frac{V_0^{3/2}}{s^2} \qquad eq.(2.12)$$

Where J_i is the ion current density to the target, M_i is the mass of the ion and S_{ch} is the Child sheath thickness.

Using the Poisson's law and continuity equations, the Child Langmuir Law can describe the sheath thickness adjacent to the target in the magnetron plasmas as [8],

$$S_{ch} = \sqrt{\frac{2}{3}}\,\lambda_D \left(\frac{2eV_0}{kT_e}\right)^{3/4} \qquad eq.(2.13)$$

where V_0 is the voltage across the sheath.

To assess the location of the cathode sheath edge, Gu and Lieberman [36] carried out measurements of the axial distribution in optical emission in a planar magnetron discharge.

Through a model of the motion of elcctrons, they predicted that the location of the peak in optical emission would coincide with the edge of the cathode sheath. They then compared trends in the thickness of the sheath to those predicted both by the Child-Langmuir Law and their own model, which was a version of the Child- Langmuir law adapted so as to include the effect of a magnetic field on the motion of electrons. Based on this model developed by Gu and Libermann [36], the sheath for a DC magnetron discharge can given as

$$s_{GuL} = \frac{4\sqrt{2}}{3}(\pi r_0 \epsilon_0)^{1/2}\left(\frac{e}{M_i}\right)^{1/4}\left(\frac{2m}{e}\right)^{1/8}\frac{a^{1/4}V^{7/8}}{J^{1/2}B^{1/4}} \qquad eq.(2.14)$$

where S_{GuL} is the sheath thickness, a is the measure of radius of curvature of the magnetic field lines tangent to the plane $r = r_0$, B is the magnetic field strength.

In an investigation into the structure of a DC magnetron discharge, Rossnagel and Kaufman [37] measured the variation in electron temperatures, electron densities and

plasma potentials, over a range of axial distances from the cathode. They observed a decrease in the value of V_p as the cathode was approached, which they associated with the edge of the cathode sheath. They calculated the sheath thickness using the Child-Langmuir law and found that values were between 50% and 90% of those determined experimentally.

1.2.3 Guiding Centre Drifts

The motion of plasma electrons and ions in an electric and magnetic field can be treated as the superposition of a relatively fast circular motion around a point called the **guiding center** and a relatively slow **drift** of this point. The drift speeds may differ for various species depending on their charge states, masses, or temperatures, possibly resulting in electric currents or chemical separation.

Consider a charge particle of charge q travelling in a uniform electric field E and magnetic field B respectively. The equation of motion of that charged particle can be described by the Lorentz's Force Law:

$$m\frac{d\boldsymbol{v}}{dt} = q(\boldsymbol{E} + \boldsymbol{v} \times \boldsymbol{B}) \qquad eq.(2.15)$$

where $\boldsymbol{v}$ the is the velocity of the charged particle, E is is the electric field intensity and B is the magnetic field strength.

If there is only magnetic field and it is uniform, the particle velocity is perpendicular to the field and other forces and fields are absent, then the magnetic force is perpendicular

to both the velocity and the magnetic field and is constant in magnitude, resulting in particle motion at constant speed on a circular path. This is known as the **gyration** around the magnetic field. For mass m, charge q, and magnetic field B, the frequency of the circular motion, the gyro-frequency or cyclotron frequency [27], is

$$\omega_c = \frac{qB}{m} \qquad eq.(2.16)$$

For speed v, the radius of the orbit, called the gyro-radius or **Larmor radius [27]**, is

$$\rho_L = \frac{v}{\omega_c} \qquad eq.(2.17)$$

If both the electric and magnetic field are present and they are uniform, the charged particles experience a drift motion. This drift motion is called the $\overline{E} \times \overline{B}$ (E-cross-B) drift. As a result, ions (of whatever mass and charge) and electrons both move in the same direction at the same speed, so there is no net current (assuming quasi-neutrality). In the context of special relativity, in the frame moving with this velocity, the electric field vanishes. The value of the drift velocity is given by [27],

$$\boldsymbol{v_E} = \frac{\boldsymbol{E} \times \boldsymbol{B}}{\boldsymbol{B^2}} \qquad eq.(2.18)$$

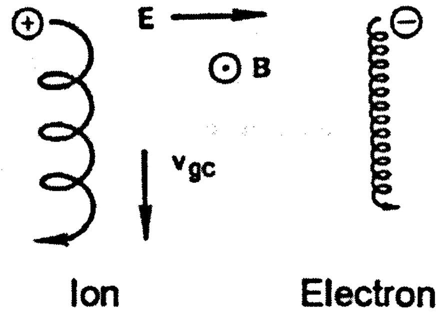

Figure 1.3: Schematic diagram of E × B drift speeds for electron and ion (taken from F F Chen [28]).

In the magnetron deposition system, due to the presence of magnetic and electric field electrons experience a significant E × B drift that results in different physical processes occurring in the discharge. Figure 1.3 shows the particle drifts in the crossed electric and magnetic field. It is important to see that the particle drift is independent from the charge q, mass m and velocity v [27].

1.3 Sputtering

This section describes the basics of the sputtering mechanism, particularly magnetron sputtering. Sputtering is a physical ballistic phenomenon which physically removes atoms from the coating material called the target, and deposits a thin, firmly bonded film onto an adjacent surface called the substrate. The process occurs by bombarding

the surface of the sputtering target with gaseous ions under high voltage acceleration. This high voltage acceleration is provided by the sheath voltage that is typically similar to the applied cathode voltage in glow discharge plasmas. The incident ions set off collision cascade in the target. When such cascades recoil and reach the target surface with energy above the surface binding energy, an atom can be ejected. If the target is thin on an atomic scale the collision cascade can reach the back side of the target and atoms can escape the surface binding energy 'in transmission'. The average number of atoms ejected from the target per incident ion is called the sputtering yield. These sputtered atoms collide with the plasma electrons and get ionized and propelled against the substrate, where they form a very tight bond. However, most of the depositing species are neutrals (gas and sputtered flux). The resulting coating is held firmly to the surface by mechanical forces, although, in some cases, chemical bonds may result. Sputtering has proven to be a successful method of coating a variety of substrates with thin films of electrically conductive or non-conductive materials. One of the most striking characteristics of sputtering is its universality. Since the coating material is passed into the vapour phase by a mechanical rather than a chemical or thermal process, virtually any material can be deposited. Direct current can be used to sputter conductive materials, while pulsed DC or RF is used for non-conductive materials to alleviate target arcing [38]. In the sputtering process, the interaction between the incident ions and the target can be treated as a series of binary collisions as shown in figure 1.4. The sputtering target kinetics can be understood in the terms of the energy transfer function in binary collisions and the sputtering yield. When an incident ion of mass M_1 collides with the

target of mass M_2, it transfers a fraction of its incident energy to the target and it can be described as [30]

$$\kappa = \frac{4M_1M_2}{(M_1 + M_2)^2} \qquad eq.(3.1)$$

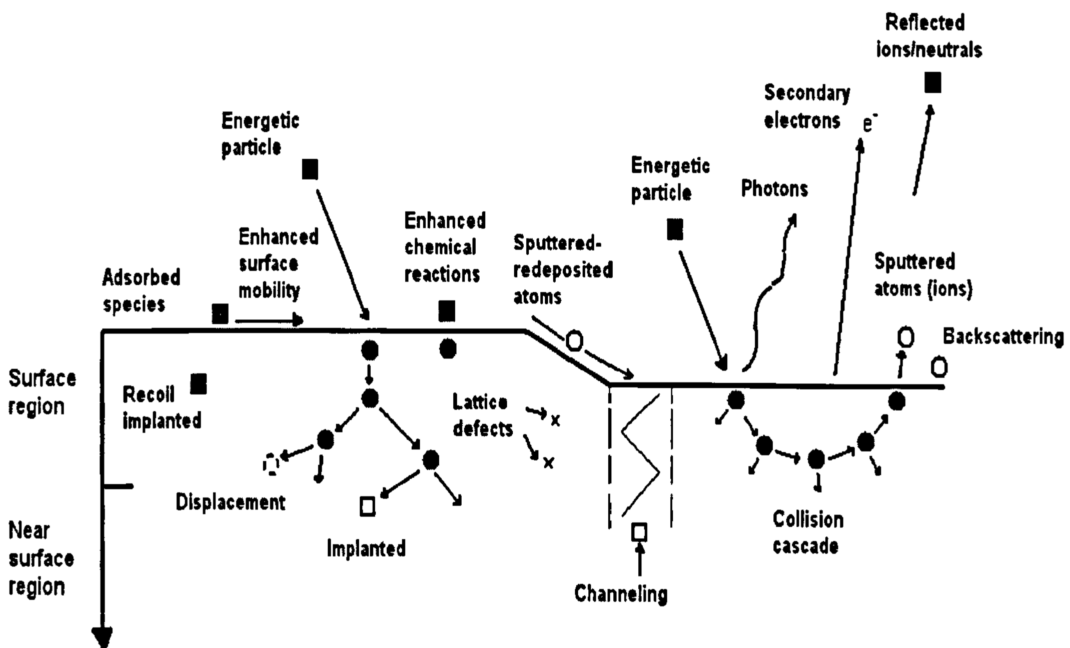

Figure 1.4: Schematic representation of various processes occurring on the surface when energetic particle incidents, taken from Mattox [41]

Substituting the mass of sputtering atom of argon (40 amu) and the mass of target atom of Titanium (48 amu), the energy transfer fraction κ comes out to 0.992. As the interaction between the incident ions and the target is very complex, the magnitude of the energy transferred to the target is often calculated by using computational

techniques such as SRIM (Stopping Range of Ions in Material) [39]. The sputtering yield is defined as [40]

$$Y = \frac{number\ of\ the\ sputtered\ atoms}{number\ of\ the\ incident\ ions\ on\ the\ target} \qquad eq.(3.2)$$

The magnitude of the sputtering yield depends on incident angle of ions, the energy of the ions and material of the target as every target material has its own physical properties such as masses of target atoms, surface binding energy of atoms in the target. For a crystalline target the orientation of the crystal axes with respect to the target surface is relevant [41, 42, 43]. As the sputtering atoms can only come from the surface layers of the target, this energy should be transferred to the surface layers only. Therefore the sputtering yield should be proportional to the energy deposited to the surface layers only and it is expressed as nuclear stopping power. Keeping this point in consideration, Sigmund (1969) predicted the sputtering yield [30] as

$$S = \frac{3\alpha}{4\pi^2}\frac{M_1 M_2}{(M_1 + M_2)^2}\frac{E}{U_0} \qquad eq.(3.3)$$

where α is a monotonic increasing function of M_2/M_1 which has the values of 0.17 for M_2/M_1=0.1, increasing upto 1.4 for M_2/M_1 =10 and U_0 is the surface binding energy.

The probability of an atom to be sputtered by the incident ion of energy of several hundred eV can be expressed as [44] as

$$p(E) = \frac{2U_0}{E^2\left(1+\frac{U_0}{E}\right)^3} \qquad eq.(3.4)$$

The simulated plot of this probability distribution against the energy of incident ion is shown in the figure 1.5. Here U_0 = 4.85 eV as for titanium target.

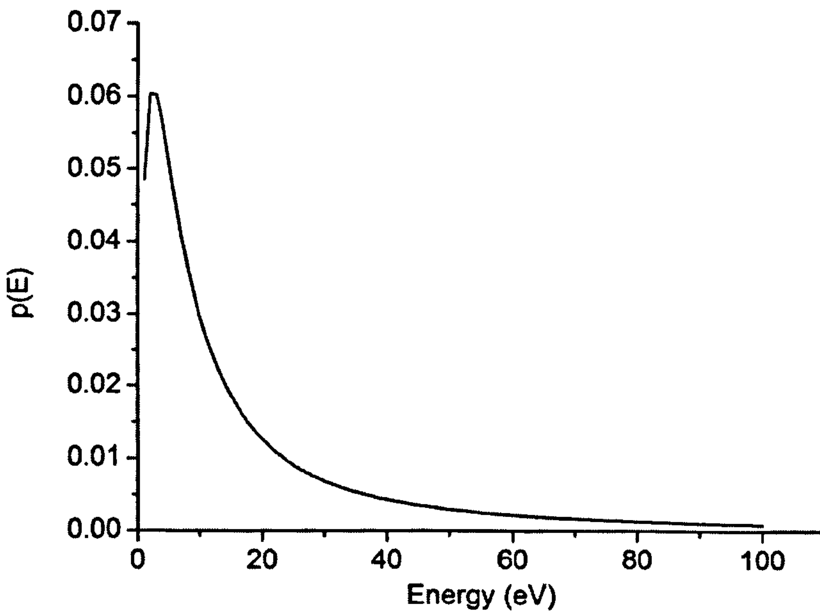

Figure 1.5: A plot illustrating the probability distribution of an atom to be sputtered against the energy of incident ion.

1.3.1 Conventional DC Sputtering

In a conventional DC diode sputtering, sputtering species are gas ions. A gas is introduced at specified pressure between 10 and 100 m Torr [41, 43]. Then a high potential of several hundred volts is applied between the two electrodes. This applied

potential difference results in an electric field between the electrodes that exerts a force on the free electrons, caused by the cosmic rays and already available in the gas, and accelerates them. These accelerated electrons collide with gas atoms and ionise them. The ions, thus produced, are accelerated by the field towards the target and sputter the target material. The impact of the gas ions on the target may also release some electrons from the target. These released electrons known as secondary electrons play an important role in sustaining the discharge. This DC sputtering technique suffers from a serious drawback of low ionization efficiency that can be improved by the various ways such applying higher voltage between the electrodes and increasing the average pressure etc [30]. Application of higher voltage between the electrodes results significant target heating and arcing that cause the damaged coatings. Increasing the pressure enhances the ionization efficiency, though the energy of the bombarding particles onto the substrate significantly reduces due to the higher collisions among the particles in the space between the target and the substrate. This, in turn, results in poor quality coatings. A possible method to increase the ionization efficiency is to confine the electrons in the vicinity of the cathode by using a magnetic field. This technique is known as **magnetron sputtering.**

1.3.2 Magnetron Sputtering

The magnetron discharges incorporate a specially shaped magnetic field to a diode sputtering. The principle is that the cathode surface is immersed in a magnetic field such that electron traps are created so that $\boldsymbol{E} \times \boldsymbol{B}$ drift currents close in on themselves. The

principle was discovered as far back as the 1930s by Penning [44] and has been used in the magnetron coating context for many years. In essence, the operation of a magnetron source relies on the fact that primary and secondary electrons are trapped in a localized region close to the cathode in an endless 'racetrack'. In this manner their chance of experiencing an ionizing collision with a gas atom is vastly increased and so the ionization efficiency is increased too. This causes the impedance of the plasma to drop and the magnetron source operates at much lower voltages than diode systems (500 - 600 V as compared with several kV). This greater ionization efficiency leads directly to an increase in ion current density onto the target which is proportional to the erosion rate of the target.

Therefore magnetron sputtering is a magnetically enhanced DC sputtering technique in which magnetic field together with the electric field produced in the sheath is used to trap the electrons near the target that results in higher ionization efficiency. Figure 1.5 shows the enhanced sputtering zone due to the application of magnetic field.

A conventional DC magnetron system consists of planar cathode (sputtering source or target) with permanent magnets placed directly behind the cathode in such a way so that magnetic field lines make a closed loop starting from and ending on the cathode surface. The anode is usually grounded and serves as the plasma boundaries (chamber walls).

Magnetrons can be used in two modes of operations i.e. balanced and unbalanced, depending on the magnetic configurations. In the balanced magnetron, the magnetic flux through the outer and inner magnets is identical.

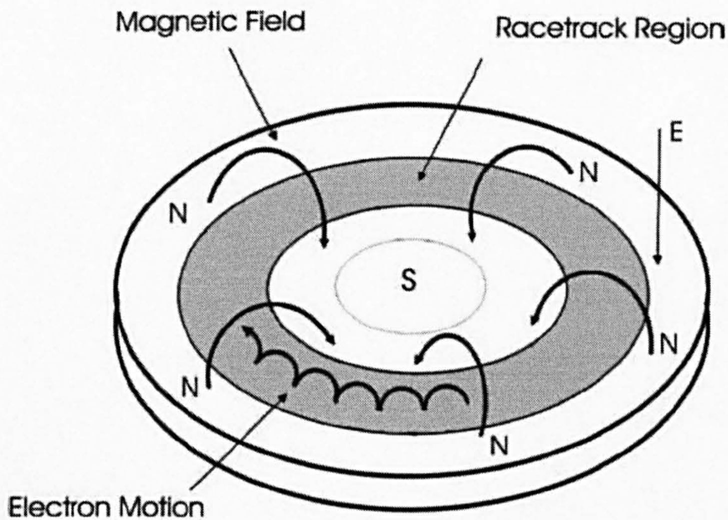

Figure 1.6: *Schematic view of the target face of a circular planar magnetron, showing the enhanced sputtering zone under the racetrack region and the motion of an electron in the E × B drift [taken from I SWINDLE THESIS (University of Liverpool), plasma diagnostics and characterization of magnetron sputtering discharges]*

By strengthening and weakening one of the poles, an unbalanced magnetron can be achieved. Unbalanced magnetron can further be divided into two modes namely type I and type II depending on the location of the null zone as shown in the figure 1.6.

In type I unbalanced magnetron, null zone is far to the target as compared to type II. In the unbalanced magnetron, the energetic electrons can escape the magnetic trap to reach the substrate.

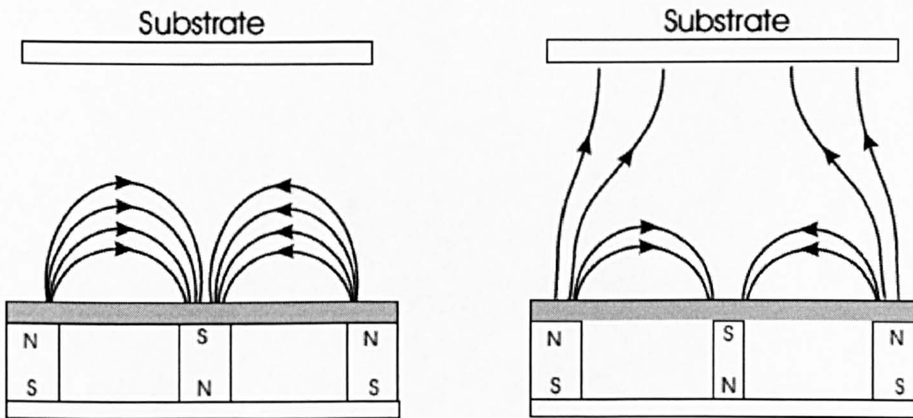

Figure 1.7: Schematic of balanced and unbalanced magnetron (Type II) (taken from I Swindle, December 2007 (Department of Electrical Engineering and Electronics, University of Liverpool), plasma diagnostics and characterization of magnetron sputtering discharges)

1.3.3 Magnetron operation

Magnetrons can be operated in a number of ways depending on the application [15]. In the simplest case, a negative voltage is applied to a single (conducting) target that develops DC glow discharge. Most of the externally applied potential at the cathode drops within a thin layer of few mm known as the cathode sheath. Due to their heavier mass (40 × 1856 × electronic mass), argon ions are not magnetized (ion Larmor radii > chamber dimensions) therefore are not confined by the magnetic field. These unconfined ions are accelerated towards the cathode sheath via a weaker electric field produced in the pre-sheath region. When these ions enter into the sheath region, the strong electric field present there accelerates ions to high energy. These highly energetic ions strike the target cause the target sputtering that occurs in small localized area known as 'race-track'.

It is also possible to use multiple magnetrons of different target materials to produce compound coatings. Alternatively a pure metal target combination with a reactive gas can also be used for this purpose. Reactions between the sputtered material and the reactive gas can now take place at the film surface and a compound film can be grown. In this way, for example, Ti-Al-N can be reactively grown by using a single Ti-Al target, or by using separate Ti and Al targets, in a N_2 environment.

Since the charged particles follow magnetic field lines, therefore the magnetic field geometry present in the magnetron plays an important role in the distribution and transport of the plasma to the substrate. This fact leads to improve the efficiency, such as higher ionization efficiency. In un-balanced magnetrons (UM), in which outer magnetic field is stronger that inner magnetic field and therefore a fraction of the magnetic field lines closes at the substrate instead of the cathode. This magnetic field geometry allows the discharge to reach onto the substrate. This results in a plasma column which leaves the magnetic trap region and transports towards the substrate. The original work on this subject has been carried out by B. Window and N. Savvides [45-47] at CSIRO Institute of Sydney.

1.3.4 Pulsed Magnetron Sputtering

Many industrial applications involve deposition of thin films in a reactive environment (nitrogen, oxygen and carbon) [15]. DC sputtering from a ceramic or compound target is not possible, if the desired coating is electrically non-conducting. When a DC voltage is applied to the insulating target, the target surface is charged up and it results in

ceasing of the sputtering process. Similar problems also occur when a metallic target is sputtered in a reactive environment. DC magnetron sputtering in reactive environment results in arcing and target poisoning that in turn, makes the discharge unstable and therefore it is impossible to deposit dense layers of the materials. A sputtering of non-conducting target materials could only be possible after introducing the radio frequency (RF) power supplies for powering the target. However, this process suffers from the various drawbacks such as lower deposition rate, lower ionization efficiency and high substrate heat loading [48]. These various drawbacks can be overcome by using the modulated alternating current (AC) supplies. These power supplies generally generate quasi-rectangular voltage waveforms in the mid frequency range 20-350 kHz. These waveforms may be in unipolar or bipolar in nature. In both of these cases, sputtering takes places in the 'on-time' phase of the pulse when a very high negative voltage is applied to the target. In the bipolar mode a positive voltage (10-20% of the 'on-time' voltage) is applied during the 'off-time' phase of the pulse. Introduction of the positive voltage in 'off-time' attracts plasma electrons to the target that in turn, discharges positive charge build-up on the target [34].

For the reactive sputtering, one must keep a very good control over the partial pressure of the reactive gas because excess gas causes the poisoning of the cathode surface and the sputtering becomes very inefficient (low rate, or a lot of arcing). On the other hand, in the absence of enough reactive gas, the compound will not form with the right stoichiometry. The partial pressure must, therefore, be controlled so that it keeps the pressure at a level where the target is kept relatively "clean" by the sputtering, but there

is enough gas to form the desired stoichiometry. This can be a quite complicated and unstable process. The right partial gas pressure depends upon the various parameters such as system geometry, target material and average discharge powers etc and it can be found only by iterative experiments.

1.3.5 High Power Impulse Magnetron Sputtering (HiPIMS)

In some applications, high concentration of metallic ions at the substrate is beneficial. DC and pulsed DC magnetron sputtering techniques suffer from a drawback of lower ionization of the sputtered metal flux (20-30 %) [18]. The quest of getting higher fraction of the ionized metal flux and guided deposition of metal flux to substrate has led to the development of high power impulse magnetron sputtering technique (HiPIMS) introduced by Kouznetsov et al. [49] in 1999, in which the deposit is formed from the bombardment of metal ions rather than neutrals. HiPIMS is a low-duty cycle, low frequency pulsed plasma technique that is characterized by very high peak currents and power densities at the sputter target, for instance reaching values up to several Acm^{-2} and $kWcm^{-2}$ at the target respectively. These values are typically only limited by requirements not to overheat the target. Since the duty cycles are typically only a few percentage, the mean applied powers are similar to those in conventional DC or pulsed DC sputtering. The typical target voltage and current pulse waveforms are shown in figure 2.5 (Chapter 2).

The application of this short and intense power pulse to the magnetron can lead to charged particle densities (n_e) in the vicinity of the target in excess of 10^{18} m^{-3}. This in

turn enhances the probability of ionization of both the background Ar gas and importantly the sputtered neutral metal (M) flux, leading to metal ion fractions, M^+/M at the substrate typically between 30 and 90 %, depending on the target material and process parameters [18].

The ability to produce a copious number of deposition ions that can be attracted and thus directed by an electrical bias on the substrate has meant HiPIMS discharges are now finding uses in a number of technological areas. These include the directional deposition of metals such as Cu into the high-aspect ratio Si trenches in micro-electronics [50], the Cr and Nb ion pre-treatment of 304 stainless steel and M2 high speed steel substrates [51] and the controlled ion-assisted growth of Cr-N films on engineering steels [26]. Despite many useful properties, it is often reported that HiPIMS discharges suffer from lower deposition rates compared to conventional DC and pulsed DC magnetron sputtering. This reduction is typically between 30 - 70 % for metals, oxides and nitrides given for same nominal applied powers, as reported in [51].

1.3.6 Purpose of this study

The purpose of this study is to get a better physical insight of the processes occurring in a HiPIMS discharges. To accomplish this, time-resolved studies of HiPIMS discharges have been carried out with various diagnostic tools such as emissive probes, Langmuir probes, power probes, deposition rate monitor and mass spectrometry. The emissive probe allowed us to measure the spatial and temporal evolution of the plasma potential with very high time resolution (< 20 ns). Time-resolved Langmuir probe

measurements provided the information about the evolution of plasma parameters. Magnetic field effect on the heating of the substrate and deposition rates has been carried out by using the power probe and the deposition rate monitor respectively. The mass spectroscopic measurements provided a picture of time evolution of various species in the discharge.

The experiments carried out and their findings will be discussed in the later chapters.

Chapter 2

EXPERIMENTAL SET-UP

This chapter details the experimental set-up used in this study, including vacuum chamber, the magnetron source, pumping system and the power supplies.

2.1 Vacuum Chamber and Pumping System

All the experiments were carried out in a purpose built cylindrical stainless steel vacuum chamber having internal dimensions of 40 cm in diameter and 70 cm in length. The chamber was evacuated by a Leybold Vacuum pump of pumping speed 1000 ls^{-1} backed by a Leybold TRIVAC D 40 B rotary pump of pumping speed 40 m^3 min^{-1}. This vacuum chamber has been supplied by Gencoa Ltd and known as Genlab. The schematic of experimental set-up is shown in the figure 2.1. During this entire study, the vacuum chamber was pumped down up to a base pressure of 7×10^{-4} Pa as measured by a penning gauge PR26 Penningvac coupled by a read out PM31 Penningvac supplied by Leybold Vacuum. After getting the base pressure, pumping speed can be reduced using a butterfly valve and the chamber was backfilled with the sputtering gas Ar (99.95% pure) to the operating pressure that is typically 0.54 Pa as monitored by Baratron capacitance manometer pressure gauge coupled with a type 250 MKS Instruments pressure control unit. The gas flow into the chamber was controlled by the mass flow controller supplied by MKS Instruments type 1179 A.

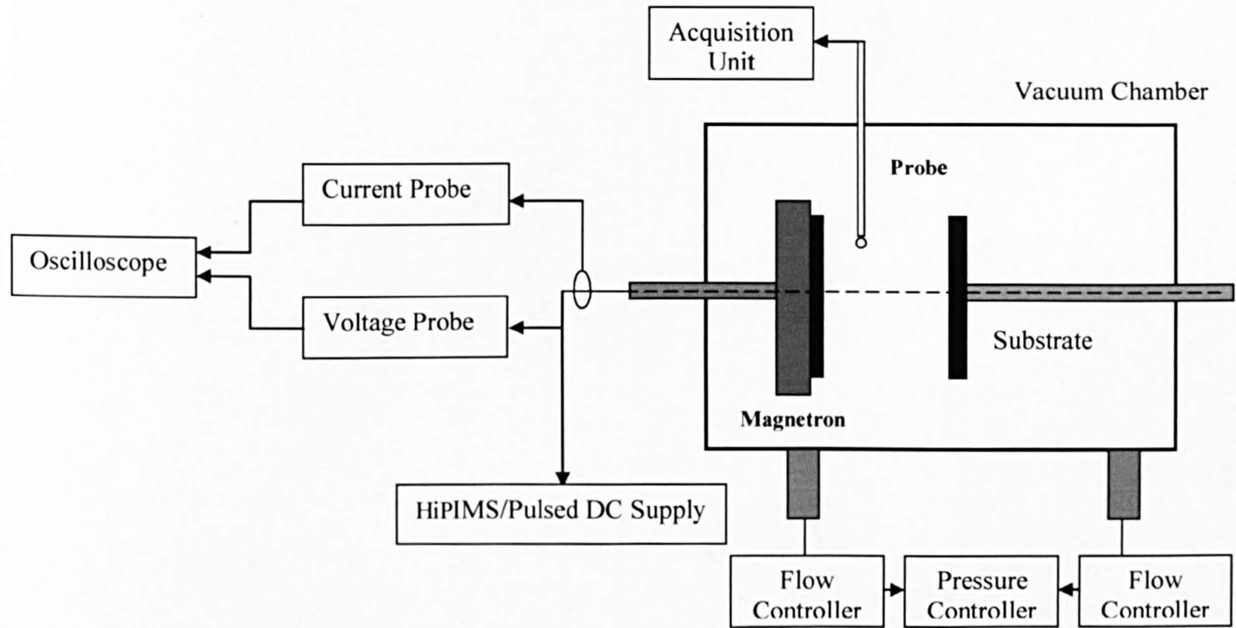

***Figure 2.1**: Schematic of the experimental set-up. For the diagnostic of different discharge parameters, different probes were used. Therefore probe and probe acquisition system is different each time.*

The cylindrical vacuum chamber was oriented with the axis of symmetry parallel to the floor. The chamber is equipped with two O-ring sealed doors at the both ends. The left end door is equipped with a cylindrical magnetron and the right end door has several access ports for mounting THE substrate holder, different probes and viewing ports. Many other ports are also available on the cylindrical surface of the chamber for the induction of additional diagnostic equipments or view ports. All these diagnostic equipments were fitted to the vacuum chamber by the Wilson vacuum Feed-through and hence could be pushed in or pulled back without breaking the vacuum that, in turn, provides the facility to diagnose the entire discharge volume.

The planar and cylindrical magnetron was mounted on a barrel which could be moved axially inside the chamber without breaking vacuum.

2.2 The Magnetron Sputter Source

In this study a planar circular magnetron cathode (supplied by Gencoa Ltd, Liverpool, UK and known as V-Tech 150) and equipped with titanium target (99.995 % pure, supplied by the Kurt J. Lesker Company Ltd.) was used. The cathode was 150 mm in diameter and mounted along the central axis of the chamber. The V-Tech 150 magnetron has the facility to alter externally the magnetic field strength and configuration of the magnetron's magnetic field configuration. It is achieved by pulling back the inner and outer magnetic poles relative to the cathode surface by using two external screw gauges mounted on the rear of magnetron assembly. Due to the movement restriction of magnetic poles, the magnetron could only be operated in type II mode of unbalance. The schematic of the magnetron with the magnetic field lines, emissive probe and deposition rate monitor is shown in figure 2.2. During the course of this study, four different magnetic field configurations have been used. However, most of the work was carried out in magnetic field configuration 1 as described in table 2.1.

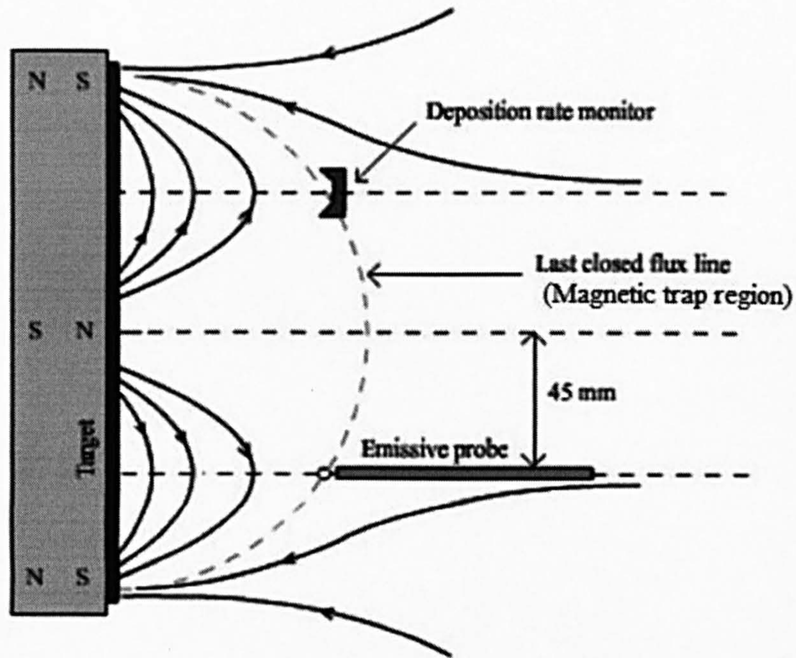

***Figure 2.2**: A schematic diagram of the magnetron source, the B-field lines, the emissive probe, the deposition rate monitor and the line along which the deposition rate ρ_d measurements were carried out. On this line the trap entends from 0 to 50 mm.*

***Table 2.1**: The location of magnets and their respective field strength*

Magnets (Inner, Outer) (mm)	Name of the magnetic field	B- field strength (G) (Radial = 45, Axial = 0 mm)
0, 0	B-field Configuration 1 (BF1)	380
5, 5	B-field Configuration 2 (BF2)	320
10, 10	B-field Configuration 3 (BF3)	260
15, 15	B-field Configuration 4 (BF4)	190

The axial distribution of the magnetic field strength as measured by Hirst GM04 Hand Held Gauss meter parallel to discharge center line and above the racetrack with a transverse Hall Probe in all the four magnetic field configurations is shown in the figure 2.3.

A spatial map of the magnetic field measured in the B-field configurationl is shown in the figure 2.4. This spatial map was achieved by measuring the magnetic field at discrete locations relative to the cathode surface with spatial resolution of 5 mm.

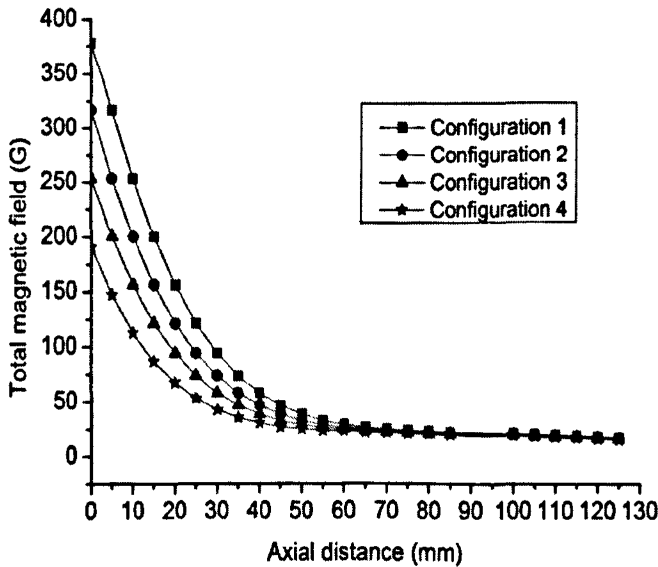

Figure 2.3: *The measured magnetic field strength* $|B| = \sqrt{B_z^2 + B_r^2}$ *for the 4 different magnet positions behind the cathode. Magnetic field shown in the figure have been measured parallel to discharge center line and above the racetrack.*

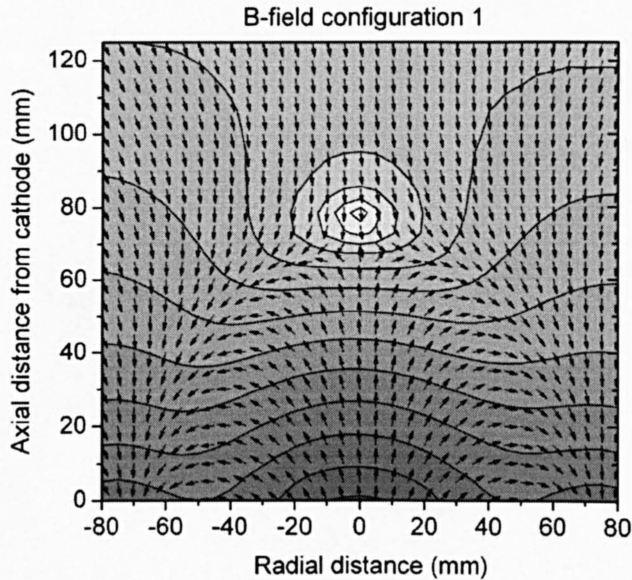

Figure 2.4. *The measured magnetic field (flux density B) and field line directions for magnetic field configuration 1 (magnets were situated at 0 mm behind the cathode). Normalized arrows indicate the B-field direction, gray scale is the magnitude of magnetic field B.*

From the figure 2.4, it can be seen that the magnetic null point ($B_r = B_z = 0$) is situated at 75 mm away from the cathode and along the center line of the target (Z = 75 mm, R = 0 mm).

2.3 Power Supplies

The experimental measurements in this study have been carried out in HiPIMS, pulsed DC at 100 kHz and 350 kHz of repetition frequency and DC. However, most of the work has been performed in HiPIMS mode. The DC and pulsed DC modes of operation have been operated only for 'comparison' purposes between plasma parameters of HiPIMS mode and pulsed DC modes.

The HiPIMS power supply unit used during this work was SINEX 3.0 supplied by Chemfilt Ion Sputtering. This power supply has been designed for HiPIMS applications and is capable of producing waveforms of peak voltage of 3.0 kV and peak current of 2.0 kAmps. Therefore, it produces very high peak power density (~several kW cm^{-2}), essential for HiPIMS applications. The pulse frequency ranges from 25 to 600 Hz and pulsed width 50 to 500 μs. These power supplies can be operated in voltage and power regulation modes of control. However, the pulse frequency and the pulse width were kept constant at 100 Hz and 100 μs during the entire study. Therefore, 'duty factors' defined as the ratio of 'pulse-on' time and time period of pulse is kept constant at 1%.

A typical cathode voltage and current waveforms produced by the SINEX 3.0 HiPIMS supply mode is shown in figure 2.5. The pulse cycle proceeds as follows. The pulse begins at t = 0 μs defined as a zero crossing line from positive to negative discharge voltage. Then it reaches a maximum negative voltage of -650 V within 200 ns. Then stabilizes for 15 μs and decays by almost half of the discharge voltage (250 V) up to 100 μs. It, then, settles at 0 V during entire pulse 'off-time'. The exact shape of the cathode current waveform depends upon the various operational parameters such as average pressure, average power and target material; however general features remain same for all operational parameters. The cathode current pulse always comes few (~ 10) μs after the initiation of the discharge voltage pulse and then starts to develop. The peak discharge current occurs around 40 μs after the initiation of discharge is then fully developed.

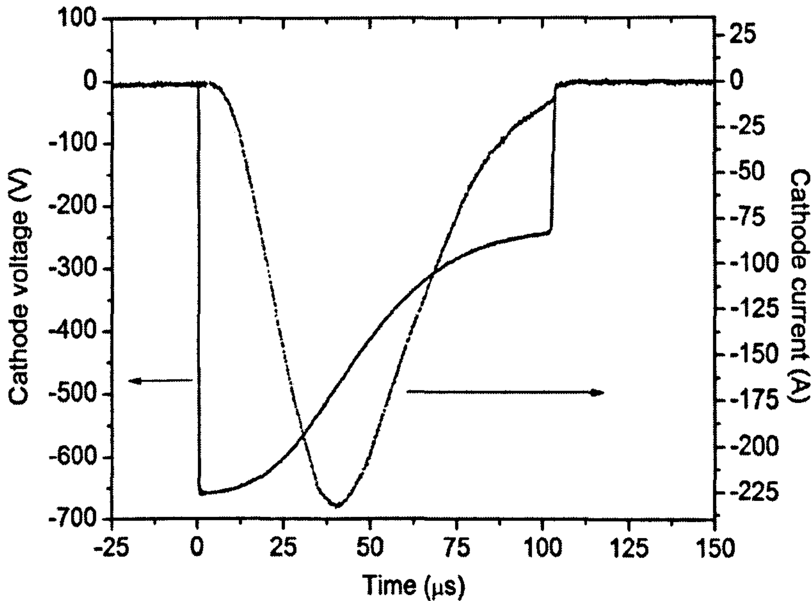

Figure 2.5. *The cathode voltage (V_d) and current (I_d) waveforms produced by the SINEX 3.0 HiPIMS power supply for an average discharge power of 650 W and a gas pressure of 0.54 Pa.*

The exact time of occurrence of peak discharge current depends upon the operational parameters such as average power, average pressure and the cathode material.

For operation in DC and pulsed DC modes, the discharge was driven by a Pinnacle Plus$^+$ power supply unit supplied by Advanced Energy Incorporated. This is an asymmetric bipolar DC pulsed supply capable of producing output waveforms in the frequency range between 0 to 350 kHz. The pulse off time can be adjusted therefore capable for various duty factors. In this present study, two frequencies were used namely 100 and 350 kHz with 50% duty factors i.e. the 'on-time' were 5 and 1.43 μs respectively.

This power supply can be operated in voltage, current and power regulation modes. However, in this study, power supply was used only in power regulation mode.

A typical cathode voltage and current pulse waveforms in 100 kHz are shown in the figure 2.6. The pulse waveform can be divided in following sections: (I) the pulse begins at t=0 μs defined as zero crossing voltage from positive to negative voltage. (II) It, then, reaches maximum positive values known as overshoot. (III) The cathode voltage stabilizes. (IV) Then it achieves it maximum negative values (V) then cathode voltage oscillates until it settles at positive value. The pulse 'on-time' and 'off-time' have been mentioned on the waveforms.

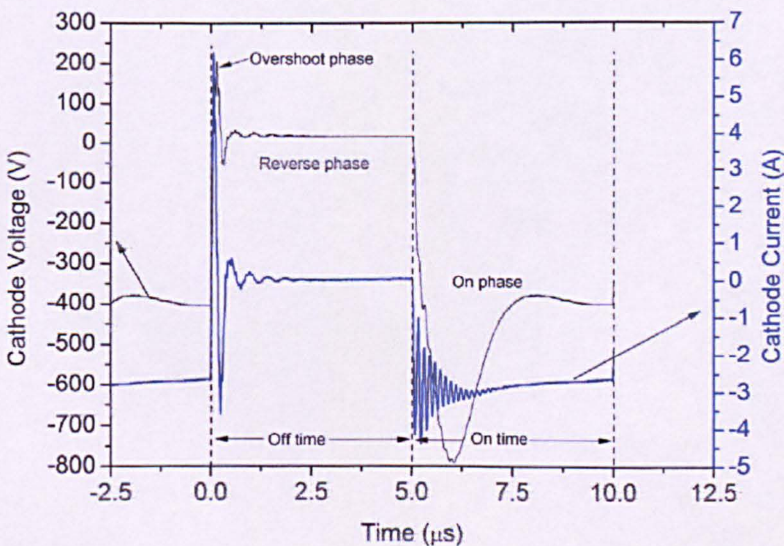

Figure 2.6: *Typical cathode voltage and current pulse waveforms in pulsed DC of 100 kHz. Duty factor was 50% and average power was 680 W.*

A typical pulse waveform of 350 kHz is shown in the figure 2.7. Comparison of figure 2.6 and 2.7, the pulse waveform changes with frequency and the different phases were identified as described earlier. During the pulsed DC mode the average power was 680 W and duty factor was 50% in both 100 and 350 kHz modes of operation.

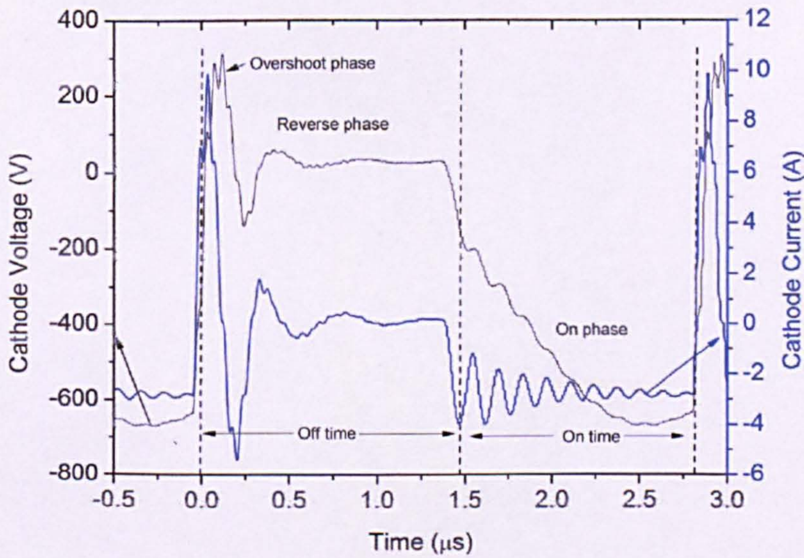

***Figure 2.7**: Typical cathode voltage and current pulse waveforms in pulsed DC of 350 kHz. Duty factor was 50% and average power was 680 W.*

Chapter 3

DIAGNOSTIC TOOLS

This chapter details the diagnostic tools used to investigate the plasma parameters during the study.

3.1 The Emissive Probe

The emissive probe is an electron emitting probe described by Langmuir [52]. These probes are used to measure the plasma potential and have distinct advantages over the Langmuir probes such as the ability to obtain the time evolution of the plasma potential with very high temporal resolution (~20 ns) and reliable plasma potential measurements in magnetic fields, in drifting plasmas and in the presence of electron and ion-beams [49]. However, while using the emissive probe in magnetic fields, the probe plane orientation with respect to the magnetic field lines should be taken into account. The emissive probes also produce accurate measurements of plasma potential even in contaminated plasmas as the heated surface of the emitting probe stays clean, whereas the Langmuir probes are subject to contamination [49]. However, emissive probes don't provide information about electron temperature and plasma density.

3.1.1 Principle of Operation

The fundamentals of the emissive probe technique have been described by Kemp et.al. [53]. Many of the details for their operation in magnetrons and other technological plasmas have been described [54-57]. We will outline here the main issues. The caused by the cosmic rays working principle of the emissive probe is as follows

the emissive probe consists of a thin, thoriated tungsten wire, which is heated (by passing current through it), up to a temperature until significant thermionic emission of electrons occurs. When the probe biasing voltage V_b, is more negative than the plasma potential V_p, the emitted electrons flow from the probe to the plasma, so reducing the effective net electron flux arriving at the probe. With strong emission this naturally pushes the probe floating potential to more positive values with $V_f \rightarrow V_p$ as the net electron flux balances the ion flux. This method provides an uncertainty in the measurement of V_p with a voltage equivalent to the wire temperature, kT_w/e, which is typically 0.1 V. However, as noted in [58] for measurements in a pulsed DC magnetron, the error in V_p is better given by the voltage equivalent of the local electron temperature (kT_e/e), typically ~ 1- 3 V during the pulse "on-time" and < 1 V in the "off-time".

Three proposed methods to use the emissive probe are found in the literature as follows:

1. **Saturating floating potential method:** - In this method, floating potential approaches to the plasma potential when the probe is in strong emission condition i.e. voltage at zero probe current is identified as plasma potential when the probe is in strong emission condition.
2. **Divergence point method:** - In this method, the point of divergence between the I-V characteristics obtained by the emissive in hot and cold condition is identified as the plasma potential.

3. **Inflection point method:** - In this method, the point of inflection in the hot probe I-V characteristics is identified as the plasma potential.

The *saturated floating potential* method provides good results with an accuracy of 1 V. It is also suitable to measure the time-resolved plasma potential with very high time resolution (~ few tens of ns) and therefore has been used in the present study to measure the time-resolved plasma potential.

3.1.2 Emissive Probe in Magnetron Plasmas

The presence of complex magnetic field geometry in the magnetron discharge makes the emissive probe measurements particularly challenging. If the electron Larmor radius ($r_L = mv_\perp/eB$ where $v_\perp$ is the velocity perpendicular to magnetic field B) of the emitted electrons from the probe is smaller than the probe wire radius r_p ($r_L < r_p$), they may return to the probe surface after one gyration. This restricts cross-field transport of electrons from the probe, forming a space charge region. The resulting reduced emission current yields an inaccurate determination of the plasma potential (V_p). In this present study, the probe radius (r_p) is 1.25×10^{-4} m and over the positions of measurement (2 to 100 mm), the B-field varies from 375 to 20 G. Assuming at these positions $T_e \sim 2$ eV [59], it yields ratios of Larmor radii to probe radii r_L/r_p of 0.99 and 18 at z = 2 and 100 mm respectively. Therefore, the effect of space charge limited emission was expected only near the target, and this indeed was observed through changing the probe orientation relative the B–field as described later. The error in V_p near the target was estimated to be around 5 %.

3.1.3 Time Response of Emissive Probe

The time response of the emissive probe depends upon the impedance of the sheath around the probe and the probe capacitance to the ground. When the probe is cold, it is irresponsive to the fast plasma dynamics because sheath around the probe has finite impedance and therefore offers a large time constant ($\tau \sim R_sC_s$).

The typical plasma potential waveform obtained by the emissive probe in strong emission condition, sampled at 100 mm away from the cathode surface and just above the race-track (Z = 100 mm and R = 45 mm) is shown in the figure 3.1. When the probe is in strongly emitting condition, the sheath around the probe collapses and therefore, in principle, $\tau \sim R_sC_s \sim 0$ as $R_s \sim 0$.

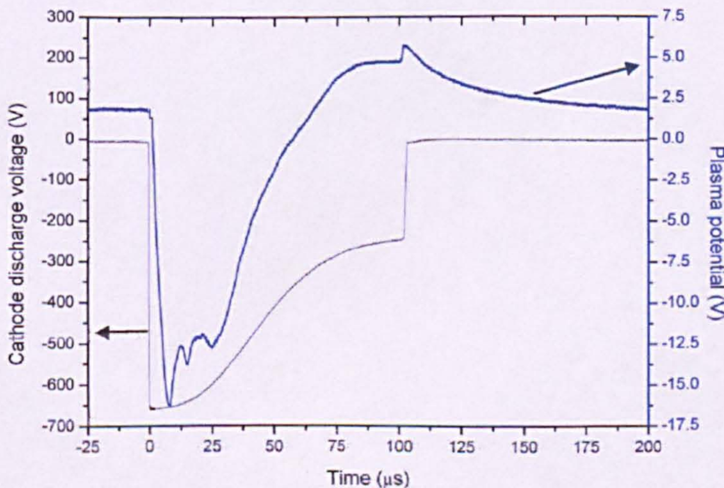

Figure 3.1.: *A plot of plasma potential waveform in HiPIMS discharge together with the cathode voltage. This waveform has been obtained at 100 mm away from the cathode and above the racetrack (Z = 100 and R = 45 mm).*

If the negative space charge is present around the probe, it provides low impedances. Therefore effective sheath impedance becomes very low and t time response very high.

3.1.4 Probe Construction and Calibration

The schematic diagram of the emissive probe is shown in figure 3.2. The emissive probe itself was made of a thoriated tungsten wire of diameter 125 μm, looped in a semicircle of 2 mm diameter and push-fitted into a ceramic stem, housing with enameled copper connecting wires of 250 μm diameter that carry the external heating current. The probe loop was heated by passing through it a 50 Hz AC current supplied by two separate transformers. The heating current in the probe loop was varied by the variable transformer.

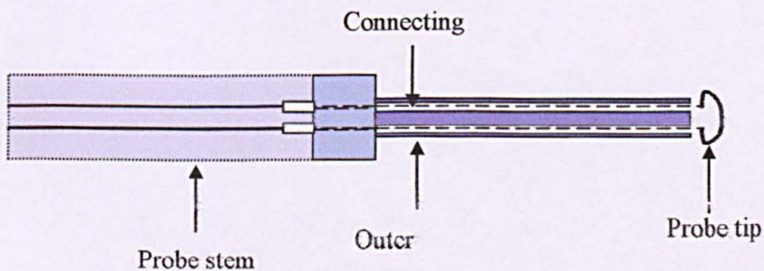

***Figure 3.2**: The schematic diagram of the emissive probe. The probe tip is semicircular loop of a thoriated tungsten wire.*

The electrical arrangement and measurement circuitry of the emissive probe is shown in figure 3.3.

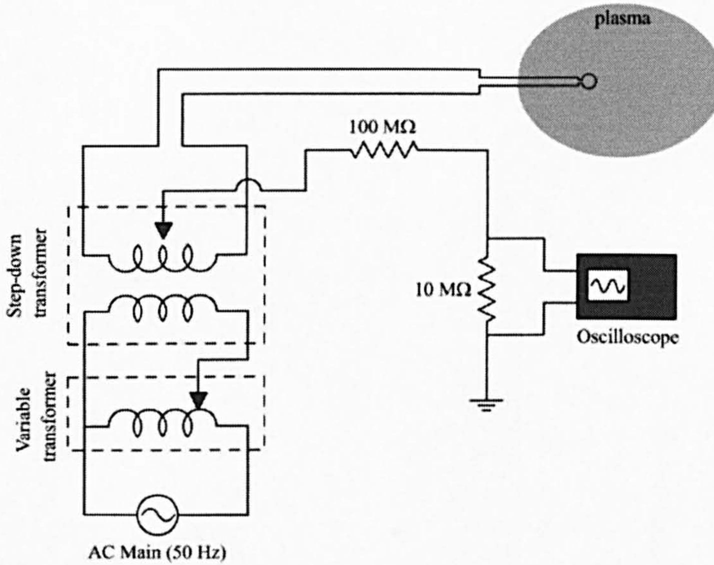

***Figure 3.3**: The schematic of electrical and measuring circuitry of the emissive probe.*

The centre tap of the second transformer was connected to a fast oscilloscope (TDS 3014, 10 MΩ input impedance, Tektronix Ltd model) via a single strand wire (used to minimize the capacitance to ground) to obtain the mean voltage (floating potential) across the loop and hence a good estimate of V_p. This floating potential data was stored over 128 discharges pulses and then averaged to minimize the random error in the electrical signal. It was found that a current of 2.5 A was sufficient to achieve strong electron emission during the entire cathode voltage pulse, however a higher current (3.75 A) is needed to achieve strong emission in the vicinity of the target ($z < 10$ mm).

3.2 Thermal Probe

Plasma surface interactions are very important mechanism in depositional and etching processes that determines the thin film properties. It supplies the energy flux that enhances the substrate temperature. This temperature rise is a very crucial parameter as atomic process such as ion implantation, etching, sputtering, diffusion and chemical processes, are all temperature dependent [30]. Moreover, manufactures are moving away from the rigid glass substrate to the polymeric web. These polymeric webs are relatively more sensitive to the temperature. Energy flux – a product of particle flux and the energy of incident particles written as average power per unit area - to the substrate changes with operational parameters and therefore, the properties of thin films such as optical, mechanical and electrical can be tailored by controlling the total energy flux to the substrate. This fact demonstrates the necessity for investigation of total energy flux to the substrate and its relationship with operational parameters.

3.2.1 Techniques to measure Energy Flux on Substrate

Energy flux onto the substrate can be measured by two different techniques. First technique used by Steffen and Kersten [60, 61] employs two copper discs connected by a stainless steel tube. One disc acts as a substrate while other one is kept at a constant temperature via water cooling. When the copper disc that acts as a substrate is in thermal equilibrium with environment (discharge), then the temperature gradient produced on the connecting stainless steel tube gives the information about the energy flux deposited at the substrate.

Second technique proposed by Thornton et. al. [62] uses a copper disc as a substrate. When plasma particles incident onto this disc, it's temperature rises. The temporal evolution of the temperature onto the substrate can be used in deriving the total energy flux onto the substrate. Due to simplicity of the technique proposed by Thornton, it has been used in this study.

3.2.2 Energy Flux Balance onto Substrate

The total energy flux on to the substrate is the summation of kinetic contributions of from the films via condensation, adsorption and chemical reactions and is shown in the figure 3.4.

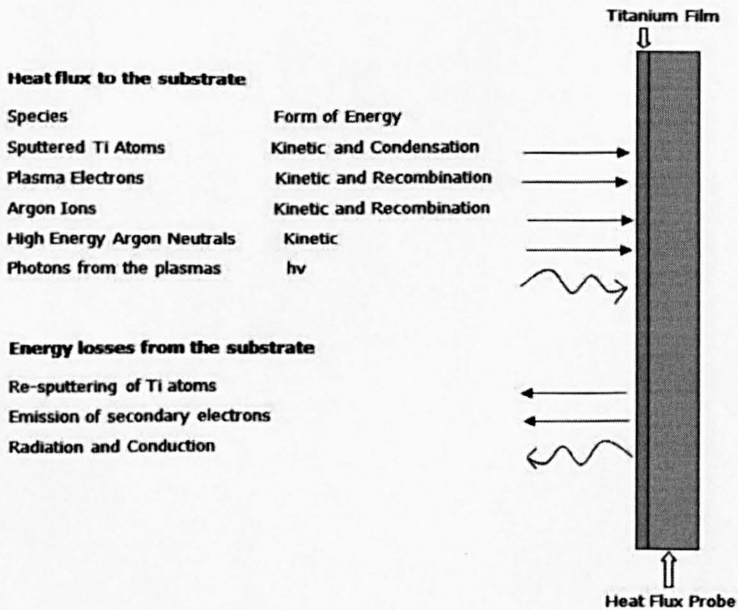

Figure 3.4: *The schematic of various contents of the power incident onto the substrate when it is exposed to plasma*

It can be described as

$$P_t = P_e + P_i + P_n + P_{rad} + P_{surface} \qquad eq.\ (3.1)$$

where P_t is the total energy flux to the substrate, P_e, P_i and P_n are the contributions by the plasma electrons, ions and neutrals, P_{rad} is the contribution due to photons and the $P_{surface}$ due to energy release at the surface.

3.2.3 Calorimetric Method – A way to determine Energy Flux

The method to calculate incoming energy flux is based upon the temporal evolution of temperature onto the test substrate. It essentially means to measure the temperature rise of the test substrate when it is exposed to the discharge and temperature fall of the substrate when the substrate is cooling. The change in energy flux to the substrate can be described as

$$\frac{dH}{dt} = C_s \frac{dT}{dt} \qquad eq.(3.2)$$

where H is the incoming power onto the substrate, C_s is the specific heat capacity of the substrate including all the connecting circuitry and interaction of the holder. T is the temperature of the substrate at a particular time.

The balance of the thermal flux onto the substrate during the measurement process can described as

$$\frac{dH}{dt} = \frac{dH_h}{dt} - \frac{dH_c}{dt} \qquad eq.(3.3)$$

where subscript '*h*' and '*c*' stand for heating and cooling processes of the substrate.

During the heating process, the energy flux balance equation can be written as

$$\frac{dH_h}{dt} = P_{in} - P_{rad_h} \qquad eq. (3.4)$$

and

$$\frac{dH_c}{dt} = -P_{rad_c} \qquad eq. (3.5)$$

where P_{in} is the incoming thermal flux and P_{rad_h} and P_{rad_c} are the losses due to the temperature of the substrate and are the functions of the substrate temperature. Therefore, the total energy flux onto the substrate can be written as

$$\frac{dH}{dt} = C_s\left(\frac{dT_h}{dt} - \frac{dT_c}{dt}\right) \qquad eq. (3.6)$$

This equation has been used for calculation of energy flux onto the substrate in this study.

3.2.4 Design and Calibration of Thermal Probe

For measuring the energy flux, a thermal probe has been used. The schematic diagram of the thermal probe used has been shown in the figure 3.5.

The probe was made of a copper disc of 24 mm in diameter and 2 mm in thickness. The copper disc was then attached via a spherical junction of 0.5 mm in diameter to a k-type thermo-couple at the rear. The junction was connected to two wires of Chromel and

Alumel. The whole assembly was inserted into a groove of 25 mm in diameter on a square ceramic block of 150 mm in length. The groove was recessed at 45 mm away from the centre of the ceramic holder. This location of the probe was chosen so that it was in-front of the racetrack. The whole surface (except of the thermal probe) was covered with a stainless steel sheet to mimic the surface of the substrate holder. The thermo-couple attached to the thermal probe was connected to the digital temperature readout via a vacuum feed through Digtron Ltd 2741-k. The whole of the measurement circuitry was kept electrically isolated to the ground so that the thermal probe must be in electrically floating condition.

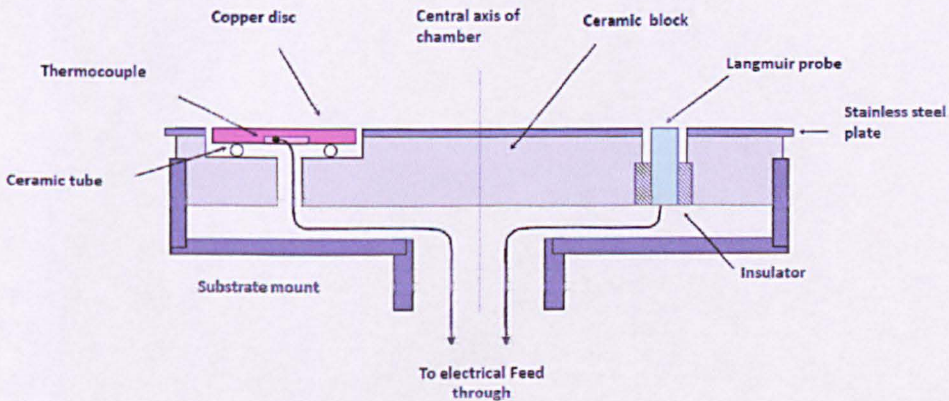

Figure 3.5: The schematic of the power probe. It consists of a copper disc of diameter 24 mm mounted onto the rectangular ceramic block. A k-type thermocouple is attached to the back of copper disc. The probe is mounted such that it faces the racetrack. This assembly also consists of planar Langmuir probe that has not been used in the present study.

To ensure that the probe should be exposed by discharge during the heating process only, a metallic shutter has been mounted with probe and it was found that the there is no temperature change of the thermal probe when the shutter was closed during the sputtering process.

To ensure that the measured energy flux by the probe should be accurate, the probe has been calibrated by a method described by Wendt et al [63]. The probe was exposed to a known heat source and biased to the voltage equal to the plasma potential. The heat capacity of the probe measured by this was found to be 2.9 J K^{-1}. The heat capacity of the probe also has been calculated theoretically according to the following formula

$$C_p = V\rho c_p \qquad eq. (3.7)$$

where C_p is the heat capacity, V is the volume of the disc and c_p is the specific heat capacity of the copper. Given the values for the copper and disc dimension, the calculated heat capacity was 3.1 JK^{-1}. Therefore the mean value of theoretically calculated and experimentally measured values was 3.0 JK^{-1} and has been used for this study.

3.3. Energy Resolved Mass Spectrometry

The properties of thin films deposited are determined by the energy distribution and composition of incident flux onto the substrate [64-66]. Therefore, it becomes necessary to know the accurate values of energy distribution and mass of incident flux to produce the engineering quality thin films with tailored properties.

3.3.1 Principle of Operation

Energy resolved mass spectrometry is a technique that can be used to get such information. This technique comprises of extraction and detection of plasma species such as neutrals, positive and negative ions according to their energy and mass. It gives the information in terms of '*energy distribution function*' with their mass.

Plasma particles are extracted from the plasma via a very small orifice. Then these particles enter into the insertion probe. If the entering particles are neutrals then they are ionized first. Then these particles travel through a series of energy and mass filters where they are binned according to their energy and mass. In-between various filters, particles are collimated by various electrostatic lenses. These collimated ionized particles are detected by the detector that is photo-multiplier tube. This scheme is illustrated in the figure 3.6.

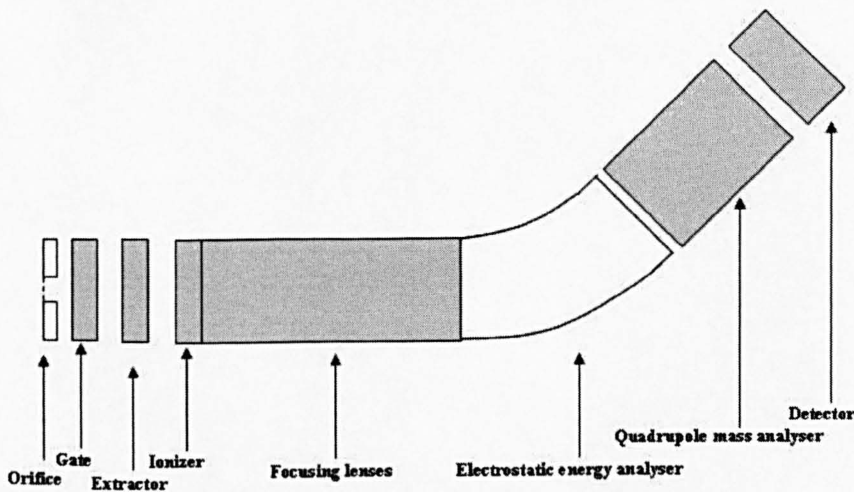

Figure 3.6: *Principle of plasma mass spectrometry with electrostatic gate to get high time-resolved measurements.*

In the present study, for energy resolve mass spectrometric measurements, energy and mass analyzer EQP-300 supplied by Hiden Analytical Ltd has been used. Here EQP stands for 'Electrostatic Quadrupole Plasma' and 300 stands for the atomic masses in amu (atomic mass unit, 1 amu = 1.67×10^{-27} kg) that can be detected by the analyzer. This instrument can measure the energy of the plasma particles in the range of ± 100 eV. The absolute value of energy range to be measured can be changed by applying external voltage on the '*reference potential* V_{ref}' situated on the analyzer control unit. For example, by the application of 500 V on the V_{ref} will allow measuring the energy of the plasma particles in the energy range of 400 to 600 eV.

The operation of mass and energy analyzer is controlled by a software MASsoft supplied by the Hiden Ltd. It provided total flexibility for the user to control the mass spectrometer.

The mass and energy analyzer can be operated in one of four modes. Residual gas analysis (RGA) mode detects the neutral particles, where an internal ionizing source is used to provide the positive ions for mass and energy analysis. In RGA negative ion mode, negatively charged ions are detected. In secondary ions mass spectroscopy (SIMS) positive ion mode, where externally generated positive ions are analyzed and in SIMS negative ion mode, externally generated negative ions are generated. Here external source of ion generation is the plasma itself.

The plasma particles can be sampled in two modes such as time-averaged, where ions are sampled by the instrument for whole of the pulse cycle and IEDFs are averaged

over the entire pulse period. In time-resolved modes of operation, ions are sampled at a specified point of time during pulse.

3.3.2 Electrostatic Ion Shuttering Technique

An electrostatic ion shuttering technique – to stop ions entering into the orifice of the instrument - has been fabricated and used in association with the commercially available mass spectrometer to get very high time-resolved IEDFs.

The electrostatic shutter was made of stainless steel mesh having 57 wires/inch and 45% geometrical transparency. The schematic diagram of the electrostatic shutter is shown in figure 3.7.

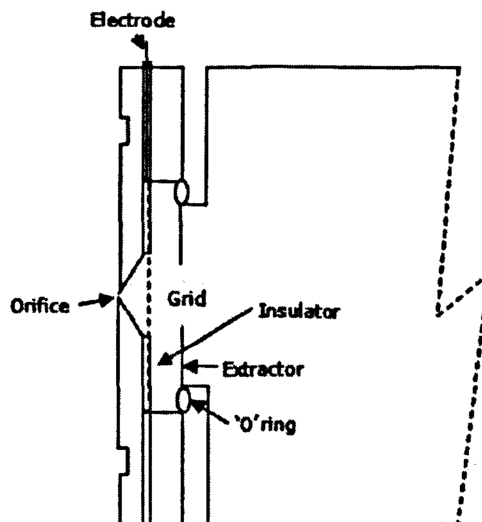

Figure 3.7: A schematic of the electrostatic ion shuttering technique that has been utilized while collection very high time-resolved IEDFs during the present study.

This electrostatic shutter was situated 0.5 mm in between the orifice and extractor. The electrostatic pulse to the shutter was supplied by the external pulse generator via a sealed pin. Both the grid and the detector have been gated by an external delay generator at a prescribed time delay. The time t=0 was the zero cutting edge of target voltage in off-on transition.

The schematic of the pulse scheme applied on the ion shutter and the on the detector of mass spectrometer together with cathode discharge voltage pulse is shown in the figure 3.8

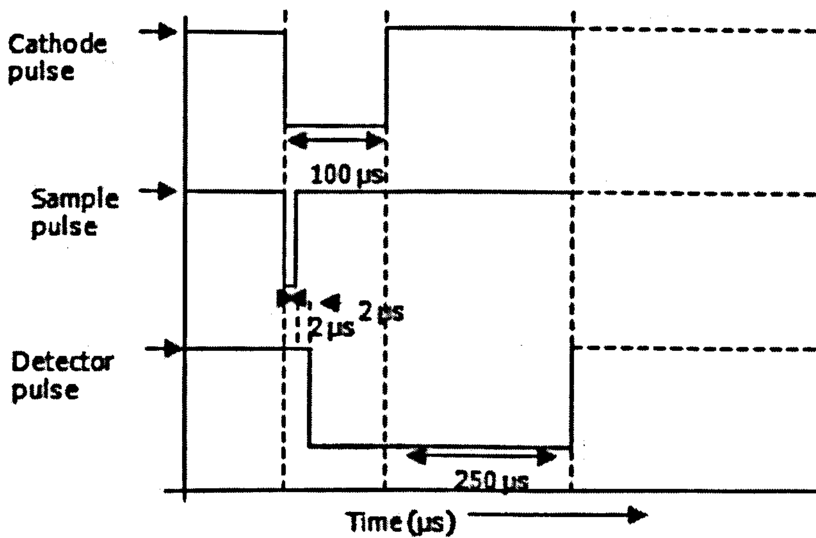

Figure 3.8: A schematic plot of the pulsing scheme applied to ion shutter while collecting the time-resolved IEDFs

During the non ion collecting region of pulse, the voltage at grid was held at 158V to repel all positive ions and during the ion collection region, the voltage at the grid was kept at -20 V for a time duration -t_g, time resolution window, allowing the ions to reach the spectrometer optics and SEM. It was found experimentally the best setting of grid and extractor voltage was -20 and -25 V for the highest counts. Falling and rising time of gate pulse was 40 and 70 ns and these are considerably shorter than the shuttering window width of 5 μs used in these experiments. After 2 μs from the end of the extractor gating pulse, shown in figure 3.8, the detector enabling pulse was sent by the EQP signal board allowing the digital ion counting pulses to be counted within this pulse. Duration of detector gating pulse was chosen 250 μs so that all the ions up to 300 amu passing through the optics could be detected at the detector.

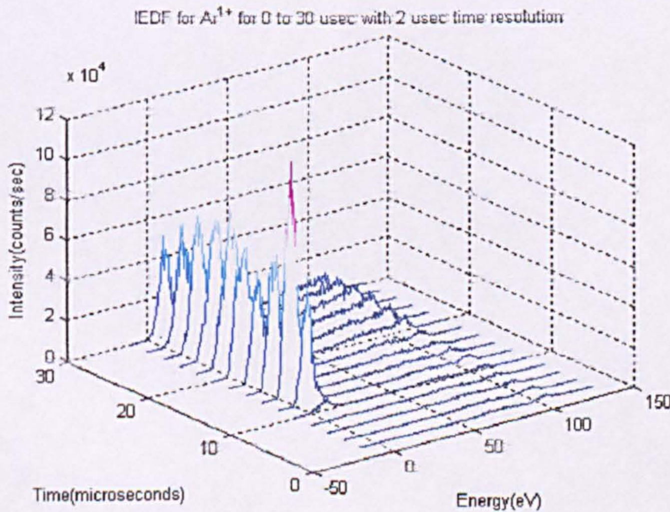

Figure 3.9: A plot of Ar^+ IEDFs collected by utilizing the electrostatic ion shuttering technique with 2 μs time resolution. A titanium target has been sputtered in Argon gas environment

This time delay between the electrostatic shuttering pulse (pulse used for ion collection) and detector enabling pulse allowed us to avoid the false ion detection at the detector due to EM interference generated by large rapid change in amplitude at the grid voltage. A typical IEDFs sampled by utilizing this technique has been shown in the figure 3.9.This electrostatic shuttering in conjunction with energy resolved mass spectrometer has been used to obtain time-resolved IEDFs with time-resolution more than 2 μs.

3.4 Thin Film Deposition Monitor

The deposition rates have been measured by using quartz crystal microbalance Maxtek thin film deposition monitor TM400.

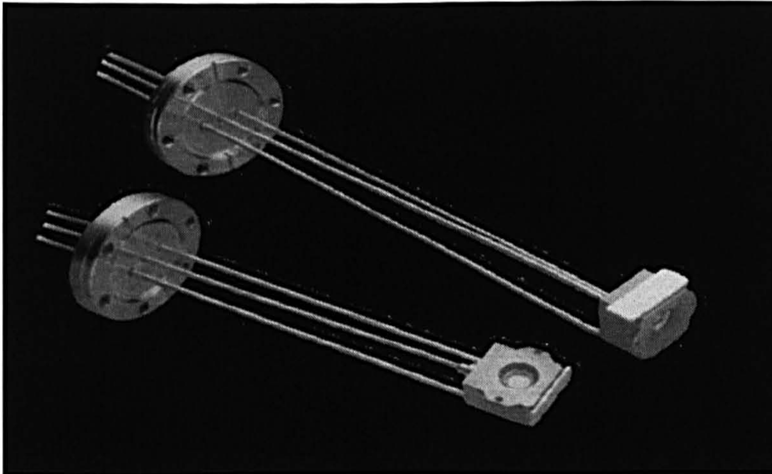

Figure 3.10: *A picture of the deposition rate monitors TM400 from Inficon Ltd. The sensor used during the present study was of silver coated quartz.*

The pictures of deposition rate monitor and its readout are shown in the figures 3.10 and 3.11.

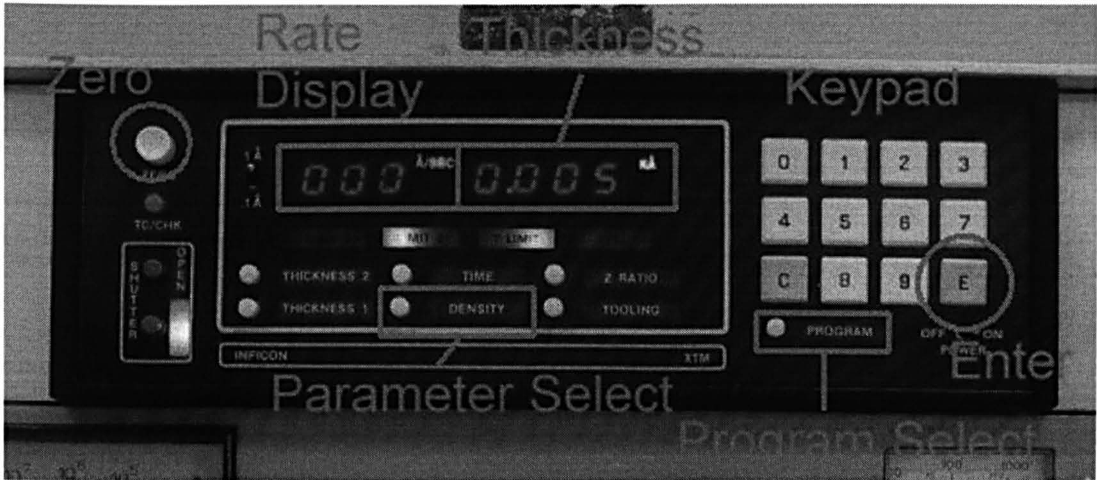

***Figure 3.11**: A picture of the deposition rate monitors TM400 read out from Inficon Ltd.*

A quartz crystal has a well defined resonant frequency which depends upon on its cut and geometrical dimension. For a quartz crystal, frequency of oscillations depends on its thickness. The monitor therefore consists of a crystal placed adjacent to a substrate onto which the film is deposited and the electrical equipment for measuring the change in the frequency. These are based on the principle that the oscillating frequency of a quartz crystal is changed by the mass of a deposited film on its upper face and the change in frequency is given by the following equation [taken from Inficon (manufactures) website].

$$t_d = \frac{\rho\, t\, df}{\rho_d\, f} \qquad eq. (3.8)$$

where t_d is thickness of the deposited film, ρ is density of the crystal, t is thickness of the crystal, df is the change in frequency, ρ_d is density of depositing material and f is frequency of the oscillator.

Electronically measuring this effect allows for a determination of the thickness of a deposited film. Once the density of the evaporated material is entered into the system, the deposited mass is measured to a resolution of 0.375 ng cm^{-2} and the thickness to a resolution of 0.5 nm on a four digit LED display having a range of 0 - 999.9 nano-meters. The crystal and holder are mounted in the vacuum chamber and connected to the oscillator of 6 MHz via the supplied BNC cable. The other end of the oscillator is connected to the display panel. The methodology used to measure the deposition rates is to measure the thickness in a specified time.

3.5 Langmuir Probe

A Langmuir probe is simply a wire, which when inserted into the discharge, measures the discharge parameters. When it is biased with respect to the discharge, current flows through it. Current flowing through the Langmuir probe is measured as a function of the applied voltage and the relation between the measured current and applied voltage is known as I-V characteristics that provides information about plasma density, plasma temperature, plasma potential, floating potential and electron energy (EEDF) functions. The beauty of the Langmuir probe is that it provides local measurements contrary to other diagnostic tools such as Optical Emission spectroscopy (OES) and mass spectroscopy. In this section, various techniques available to extract the plasma parameters will be discussed in the following sections.

3.5.1 Langmuir Probe Theory

The classical theory of Langmuir probe has been proposed by Mott and Langmuir in 1926 [67]. When the probe is biased by a potential V_b with respect to the plasma, current I_p flows through the probe. A plot between the measured I_p and applied voltage V_b is known as I-V characteristics and reveals the information about the plasma parameters such as plasma electron density (n_e), plasma ion density (n_i), plasma electron temperature (T_e), plasma potential (V_p), floating potential (V_f) and electron energy distributions (EEDF) functions.

For the convenience in analyzing, I-V characteristics are divided into three regions. When a negative voltage ($-V_b$) with respect to the plasma potential (V_p) is applied to the probe, it attracts the plasma ions and repels the plasma electrons. At sufficiently large negative potential ($-V_b >> V_p$), probe collects plasma ions only and the probe current comprises only of the ion current and there is no contribution of electron current to probe current. The current collected by the probe in this condition is known as ion saturation current. This region has been labeled as I_{ionsat} in figure 1.1 (Chapter -1).

When a positive potential is applied to the probe, it attracts electrons and repels ions. At a certain potential, the sheath around the probe collapses and electrons reach the probe with their thermal velocities. The potential applied to the probe is known as plasma potential and the probe current, in this situation is known as electron saturation current labeled as $I_{electronsat}$ in figure1.1 (Chapter 1). In the intermediate region, the probe collects both the electron and ion current.

For deriving the plasma parameters from the I-V characteristics, it is assumed that the sheath around the probe is collision less and electrons follow Maxwellian distribution. The ion saturation current to the probe can be expressed [8] as

$$I_{i\,sat} = -en_s A \left(\frac{eT_e}{M_i}\right)^{\frac{1}{2}} \qquad eq.(3.9)$$

where I_{isat} is ion saturation current, e is the electronic charge, n_s is plasma density within the collecting area ($n_s \sim 0.61\ n_0$, where n_0 is the bulk plasma density), A is the current collecting area that is bigger than the area of the Debye sphere ($A > \lambda_d^2$), T_e is the electron plasma temperature and M_i is the mass of the ion.

When the probe is biased at the plasma potential, it collects the electrons with their thermal velocities. The current collected in this condition is known as electron saturation current and can be expressed [8] as

$$I_{e\,sat} = \frac{1}{4} en_s A \bar{v_e} = en_s A \left(\frac{eT_e}{2\pi m_e}\right)^{\frac{1}{2}} \qquad eq.(3.10)$$

where $\bar{v_e}$ is the mean velocity of the electrons. The factor 1/4 comes from two factors of 1/2. First 1/2 accounts for the fact that at the sheath edge the plasma density is half of the bulk plasma density i.e. half of the density is heading towards the probe. The second factor of 1/2 accounts for the average if the direction cosines are average over hemisphere.

When the probe is biased in the electron retarding region ($V_b < V_p$), the total current to the probe will be $I=I_e+I_i$ where I_e can be written as

$$I_e = I_{e\,sat} exp\left(\frac{V_b - V_p}{T_e}\right) \qquad eq. (3.11)$$

Taking the natural log of the above equation yields

$$ln\left(\frac{I_e}{I_{e\,sat}}\right) = \frac{1}{T_e}(V_b - V_p) \qquad eq. (3.12)$$

Therefore, the slope of the plot of $ln(I_e)$ versus V_b directly gives the electron plasma temperature.

Langmuir probes may be planar, cylindrical and spherical in shape. However cylindrical probes are more common due to their simplicity in construction and they can easily satisfy the condition where current collecting area of the probe is greater than probe area ($A \gg a^2$), so that Orbital Motion Limited (OML) current theory can be applied easily.

Analysis of the Langmuir probes was first proposed by Mott and Langmuir [67] where the OML theory was first utilised. Then theory was later strengthened by Allen, Boyd, Reynolds [68] and Laframboise [69].

This theory is applicable when the sheath is collision less ($\lambda_{e,i} \gg s$) and thick ($s \gg a$). In this condition all the particles entering into the sheath are collected by the probe because of the very less probability of collisions. In this case, the probe current is independent of the exact shape of the potential because the conservations laws of energy and momentum concern only the initial and final values of energy and angular momentum.

Considering the probe length is greater than the radius of the probe ($l_p > a$) and the electrons obey the Maxwellian distribution in the bulk plasma, the current collected by probe can described as [69],

$$I_{i,e} = \frac{\sqrt{2}}{\pi} Aen_s \left(\frac{T_{i,e}}{m_{i,e}}\right)^{\frac{1}{2}} \left(1 + \frac{e\phi_p}{T_{i,e}}\right)^{\frac{1}{2}} \qquad eq.(3.13)$$

Where ϕ_p is ($V_b - V_p$) and the subscripts i and e for the ion and electron current respectively. If the ϕ_p is very large ($e\phi_p \gg T_{i,e}$), then equation 3.13 can be written as

$$I_{i,e} = \frac{\sqrt{2}}{\pi} Aen_s \left(\frac{T_{i,e}}{m_{i,e}}\right)^{\frac{1}{2}} \left(\frac{e\phi_p}{T_{i,e}}\right)^{\frac{1}{2}} \qquad eq.(3.14)$$

From the above equation, it is clear that in the limits of high potentials, a plot between I^2 and V_b is a line and the slop of this line gives directly the density n_s^2, independent of plasma temperature.

The applicability of Langmuir probe theory can be determined by considering three factors

1. The ratio of Debye length and probe radius a/λ_d
2. The ratio of electron and ion temperature T_e/T_i
3. The Knusden number $K_{i,e} = \lambda_{i,e}/a$

The first two conditions are necessary for OML theory to be valid. When ion and electron temperatures are comparable, then the plasma density calculated by this method will be reduced by a factor of $(T_i/2\pi T_e)^{1/2}$.

3.5.2 Langmuir Probe in non-Maxwellian Plasmas

Langmuir probe theory discussed above is only valid for Maxwellian plasmas. In the low pressure regime, where the discharges are not Maxwellian, application of the above theory yields the error in the calculation of plasma parameters. Processing of different parts of I-V characteristics by different probe theory (such as orbital motion and radial motion theories of ion current) gives different values of same parameters. Godyak et. al. [70] calculated plasma parameters from I-V characteristics when the electron energy distribution functions (EEDFs) were not Maxwellian i.e. these were bi-Maxwellian and Druyvseteyn EEDFs. Since the magnetron sputtering discharges are also operated at low pressure, therefore these types of EEDFs were also observed in magnetron sputtering discharges [71-75]. Hence, it is essential to extract plasma parameters from the I-V characteristics considering the bi-Maxwellian or Druyvseteyn EEDFs. This method is known as Druyvseteyn method and involves the differentiating of the probe characteristics to get EEDF and calculating plasma density and effective temperature by integrating of EEDF. The plasma potential is estimated by finding the zero crossing of the second derivative of I-V characteristics. The method can be described as following.

For an arbitrary and isotropic electron velocity distribution $f_e(v)$, the EEDF can written as

$$g_e(\varepsilon)d\varepsilon = 4\pi v^2 f_e(v)dv \qquad eq.(3.15)$$

where $\varepsilon = mv^2/2e$ is the electron energy. Introducing this relation into the above

equation results

$$g_e(\varepsilon) = 2\pi v^2 \left(\frac{2e}{m}\right)^{3/2} \varepsilon^{1/2} f_e[v(\varepsilon)] \qquad eq.(3.16)$$

The electron velocity distribution function can directly be calculated from I-V characteristics according the following relation

$$f_e[v(\varepsilon)] = \frac{me^2}{2\pi Ae^3}\frac{d^2I_e}{dV^2} \qquad eq.(3.17)$$

Substituting equation in 3.17 into equation 3.16

$$g_e(\varepsilon) = \frac{2m}{e^2A}\left(\frac{2eE}{m}\right)^{1/2}\frac{d^2I_e}{dV^2} \qquad eq.(3.18)$$

Above equation 3.18 gives the electron EEDF. The plasma density can be calculated from this equation as

$$n_e = \int_0^{\infty} g_e(\varepsilon)d\varepsilon \qquad eq.(3.19)$$

and effective plasma temperature

$$T_{eff} = \frac{2}{3}\langle\varepsilon\rangle \qquad eq.(3.20)$$

and plasma potential can be calculated from the point where $\frac{d^2I_e}{dV^2} = 0$.

This method to extract the plasma parameters has several advantages such as (1) it is

applicable in low pressure discharges where the EEDF is not Maxwellian. (2) It is free from the ratio of probe dimension to Debye length and applicable for any convex probe geometry.

3.5.3 Langmuir Probe in Pulsed Plasma

Most of the processing plasmas are operated in pulsed mode such as RF, mid frequency and HiPIMS mode. In these plasmas, plasma parameters evolve with time. The validity of the Langmuir probe theory relies on the robustness of Child sheath around the probe against the time. But in the pulsed plasmas, the Child sheath varies with time due to the varying potential. The I-V characteristics obtained by Langmuir probe get distorted due to the presence of displacement current produced by sheath oscillation and therefore, the time averaged Langmuir probe measurements does not yield accurate information about the plasma parameters. It makes necessary to diagnose the plasma in the time-resolved mode.

Time resolved measurements using a Langmuir probe are possible if operating frequency is less than the ion plasma frequency ($f \ll f_{pi}$). In this condition, the changes in plasma parameters are slow enough, so that ions can respond to varying plasma parameters on the time scale of inverse ion plasma frequency ($\tau \sim f_{pi}^{-1}$) and can maintain the Child sheath around the probe. In the case of $f \gg f_{pi,}$ the ions can not respond, but the plasma electrons can respond due to $f_{pe} \gg f$ and electrons and ions are not in equilibrium anymore. It produces a distortion in I-V characteristics due to the displacement current. It offers a restriction of the time-resolution of the Langmuir probe measurements and it is on the time scale on inverse ion plasma frequency $\tau \sim f_{pi}^{-1}$.

Typically, in the processing plasmas τ is ~ 100 ns. Therefore, the time-resolution can not be higher than 100 ns. Additionally, the circuitry used to measure is also has some time response of order of ~100 ns. It makes the time resolution higher than 200 ns impossible.

3.5.4 Practical Considerations in Designing Langmuir Probe

The presence of the probe always perturbs the plasma. Therefore, before using the probe, some designing considerations should be taken into account. The probe holder should be electrically floating so that it does not extract any current from the plasma. The length of the probe holder should be many times greater than the Debye length, so that the current collected by the probe holder from the plasma should be very small compared to the total plasma current.

The small radius of the probe offers the small current collecting area and therefore draws small current from the discharges and does not perturb the discharge. Moreover, the smaller size of the probe radius also reduces the magnetic field effects on the I-V characteristics. The length of the probe wire should be many times longer than the probe radius to reduce the shadowing effects.

3.5.5 Designing and Fabrication of the Langmuir Probe

Using the Langmuir probe in the magnetron plasmas faces difficulties due to deposition of thin layer over the probe tip and supporting stem. In the case of insulating oxide films, the deposition of the film onto the probe tip reduces the collecting area of the probe.

This eventually results in the failure of the probe. In case of conducting metallic films, deposition of metallic flux onto the probe enhances the area of the probe. Over the long time of use, the deposition flux might also deposit onto the probe support stem and might provide the connectivity between the probe tip and the much larger probe stem. If it happens, it increases the collecting area of the probe drastically (~100s times) and, in turn, extracts large currents from the plasmas perturbing the plasmas. Therefore, the probe must be designed so that these drawbacks produced by the depositing flux could be minimized and the probe should be cleaned on regularly to get accurate measurements

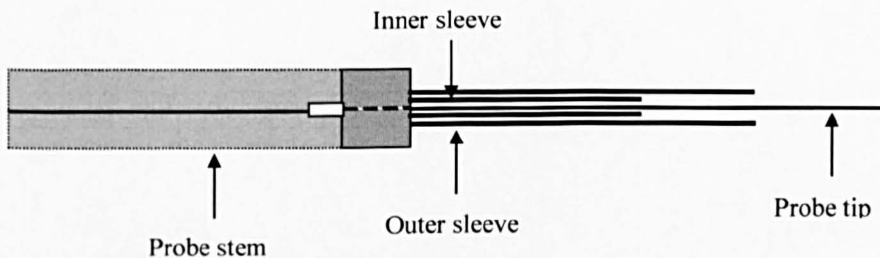

***Figure 3.12**: A schematic of Langmuir probe used in this study.*

The cylindrical Langmuir probe has been used for the present study as shown in the figure 3.12. The probe tip was made of tungsten wire of diameter 100 μm and length of 3 mm. This probe was housed in two ceramic tubes named as outer and inner sleeve to avoid the probe tip to be deposited by the deposition flux. The length of outer sleeve was kept 150 mm to avoid any metallic surface in-front of the cathode. This whole of the assembly was fitted in such a stainless steel stem that can be push fitted into a stainless steel probe shaft. This construction of the probe enable to measure I-V

characteristics for duration of entire experiment without any measurable change in the I-V characteristics recorded.

3.5.6 Automated Langmuir Probe System

The Smart Probe system supplied by Scientific Systems has been used for the present study. It has voltage scan range from -95 to +95 V that can be varied depending upon the application. The voltage range is divided into 200 equal steps with 25 mV resolution for measuring the I-V characteristics. The voltage range is selected by using the software control for each measurement. The number of the sampling points for each scan and number of the scans for each I-V characteristics can be set by the software. It has the current range 0.25 to 250 mA (@13.56 MHz) with auto current range system with 0.1 μA. For time resolved measurements, the Smart Probe system is used in BOXCAR mode with maximum trigger rate of 18 kHz and time resolution of 1 μs and it requires an external negative TTL trigger signal at the external trigger port to trigger the Smart Probe system. This external trigger signal is supplied to Smart Probe system by a delay generator (Stanford Research Systems DG535). A cathode discharge V_d is supplied to delay generator by a x100 voltage probe. At the user defined set point during the pulse (zero crossing voltage is t = 0 + delay), the delay generator produces the -5 V TTL signal that goes to external trigger port of the Smart Probe system. In the time-resolved mode, each time a trigger is received one point on the I-V characteristics is measured and 200 points are required for a complete I-V characteristics to be acquired. The number of samples per point and the number of sweeps per scan decides

the total time required to measure I-V characteristics. Therefore the total time required to get one I-V characteristics is

Total time required = [200 × No. of samples per point × Trigger period] × No. of sweeps

If the number of sweeps or number of sample per point is increased, that total time also increases.

Chapter 4

PLASMA POTENTIAL MEASUREMENTS

The plasma potential is an important intrinsic parameter as it determines electric field structure, transport and the energy distribution of the charged particles incident onto the substrate that, in turn, influences thin film properties. Therefore, to gain more understanding of the plasma processes, it is necessary to investigate the temporal evolution of the plasma potential and how it changes with global parameters such as average pressure, average power and magnetic field strength. This chapter describes the time evolution of plasma potential in HiPIMS discharges and its relationship with the deposition rate.

4.1 Evolution of Plasma Potential in One-dimension

This section describes the one dimensional spatial-temporal evolution of plasma potential along a line parallel to the discharge central line and above the racetrack, the effect of magnetic field strength on it and its relationship with deposition rates.

4.1.1 Introduction

An electron-emitting probe has been used to measure the temporal evolution of the plasma potential (V_p) along a line from target (Ti) to substrate above the racetrack in a HiPIMS discharge pulsed at 100 Hz with 100 μs pulse 'on-time'. The 20 ns time-resolution of the probe allowed us to observe the highly dynamic nature of V_p as the discharge voltage waveform develops.

The ability to produce copious number of deposition ions that can be attracted and thus directed by an electrical bias on the substrate has meant HiPIMS discharges are now finding uses in a number of technological areas. These include the directional deposition of metals such as Cu into the high-aspect ratio Si trenches in micro-electronics [50], the Cr and Nb ion pre-treatment of 304 stainless steel and M2 high speed steel substrates [51] and the controlled ion-assisted growth of CrN films on engineering steels [26].

Despite many useful properties, it is often reported that HiPIMS discharges suffer from lower deposition rates compared to conventional DC and pulsed DC magnetron sputtering. This reduction is typically between 30 - 70% for metals, oxides and nitrides given for same nominal applied powers, as reported in [50].

A number of workers have attempted to explain this observation by considering particle balance (ions and neutrals) in the discharge bulk. For instance, a phenomenological model, based on a signal flow graph with parameters interpreted as gains (adopted from Mason's gain formula) [76], has been developed by Christie et. al.[77]. The model predicts a lower deposition rate due to considerable back-scattering of metal ions (M^+) from gas ions, transporting them back to the target. Experimental observations have also been used to help explaining the lower deposition rates in HiPIMS. For instance, using a range of target materials, it has been established that the deposition rate can be directly related to the self-sputtering yield [50, 78] of the target material. Recently, Emmerlich et al. [79] used TRIM code and experimental results with Cu deposition to argue that since the sputtering yield (γ) is a non-linear function

of the applied target voltage ($\gamma \sim V_d^{1/2}$) and in HiPIMS V_d is significantly higher than in conventional sputtering (i.e. 500 to 3000 V compared to 400 V), therefore it is unreasonable to compare the two types of system for a given applied power. The bulk plasma conditions can also influence the deposition rate. Bohlmark et al. [80] showed that the magnetic geometry is an important factor and through the use of an additional, adjustable magnetic field demonstrated that the depositing ionised metal flux can be redirected to the substrate so enhancing the deposition rate. It has also been reported by the same group [81] that ions above the racetrack can achieve substantial energies in the azimuthal (E x B) direction through electron-ion friction (as a result of anomalous transverse resistivity and wave-riding), so deflecting metal ions M^+ sideways towards the wall and away from the substrate, lowering the deposition rate. Konstantinidis et. al. [82] argued that metallic ions are unable to leave the magnetized plasma (trap) due to a lack of electrons in the inter-target-substrate space affecting the space charge distribution. They suggest that the space charge of ions should be balanced by that of electrons for the efficient transport of the metal ions to the substrate. Considering this key point, they obtained higher deposition rates by applying an additional inductively coupled plasma source, which enhanced the mobility of the ions.

One area which has received little attention however, is the structure of the plasma potential V_p between the target and the substrate and how it may affect the deposition rate. Since a substantial proportion of the depositing flux in HiPIMS is ionized, any rising potential in the bulk may act as a barrier to ionized species reaching the substrate. The observation of anomalously large potential gradients (i.e. ~ 22 V across a 4 cm region) in the bulk plasma has already been made in pulsed DC magnetrons

[58, 83, 84] using a specially constructed emissive probe and it is not unreasonable to expect such electric structures could exist in HiPIMS plasmas.

It is the aim of this work to apply the methods described in [58] to examine in detail the distribution of V_p in a HiPIMS discharge, not only to gain new information on the electric field structure of the plasma but also to investigate if V_p can have some bearing on the ion fluxes at the substrate. Knowledge of V_p is generally important in plasmas because it reveals the electric field structure in the plasma volume, it defines the potential at which ions are generated and hence determines their bombarding energies at the substrate and it affects charge particle transport and the overall distribution of electron and ion plasma densities in the discharge.

Measurements of V_p in HiPIMS discharges have already been made using Langmuir probes [84-86, 59] for a number of different discharge geometries and operating conditions. For instance, time-resolved measurements of V_p at positions in the bulk plasma (9 cm from the target) have revealed only positive potentials during the whole pulse period with a peak value of $V_p \sim + 5$ V seen at the end of the "on-time" phase (duration of 100 μs) [85, 86]. The plasma potential then decayed in the afterglow, down to +0.5 V after t = 400 μs. In addition it was found that V_p values increase with lower working pressure. Spatial measurements of V_p have also been made using the Langmuir probe [86] at three radial locations (r = 0, 5 and 7 cm) for a fixed axial distance (9 cm) revealing that V_p does not change over the chosen positions, i.e. the peak in V_p was invariant at + 3.5 V (t = 100 μs) and always decayed to about + 0.7 V (at t = 500 μs). In a different HiPIMS discharge, with a 200 μs pulse "on-time", other

time-resolved measurements of V_p [59] show two peaks of +2.5 V and +3.5 V, the first occurring in the "on-time" at t = 50 μs and the second in the "off-time" at and t = 225 μs. With increased time, V_p reduced +1 V at t = 300 μs. It was also reported in the same publication that higher discharge currents give rise to higher peak values of V_p (e.g. +2.5 V at 5 A and +3.5 V at 50 A) measured in the afterglow, t = 225 μs.

Langmuir probe estimates of V_p can be problematic particularly in magnetised and pulse plasmas (such as HiPIMS), and coupled with usually poor temporal resolution (typically ~ 10 μs). Therefore emissive probe technique has been used to gain both temporal and spatial information of V_p. This relatively simple technique, when operated in the so-called "saturated floating potential regime" provides V_p directly without the need for (post-experiment) data derivation, as described in [58,83,84,87, 88]. Although the emissive probe has not to date been applied to the high density HiPIMS environment it has been successfully used in the edge of a tokamak plasmas [89] where the values for n_e and magnetic field strength B are similar to the maximum values in this study.

4.1.2 The Experimental Arrangement

A planar circular magnetron (V-TECH 150 supplied by GENCOA Ltd,) equipped with a 99.99% pure titanium target of 150 mm diameter was used in this study as detailed in chapter 2 .

Plasma Potential Measurements

The magnetron source was energized by a SINEX 3.0 HiPIMS power supply (from Chemfilt Ion Sputtering) operated at fixed frequency of 100 Hz and an "on-time" pulse width of 100 μs. The target was sputtered in an argon gas environment (purity 99.99%) at pressures of 0.54 and 1.08 Pa and time-averaged powers of 650 and 950 W. The peak target power and current density in this study were ~3 kW cm^{-2} and ~ 2.7 A cm^{-2} respectively. The plasma potential measurements were carried out above the racetrack on a line parallel to the discharge axis at a radial position of r = 45 mm. This line extends axially from positions close to the target (z = 2 mm) to a typical substrate position (z = 100 mm). Emissive probe measurements were made every 5 mm for target-probe separations z > 5 mm, however close to the target, in the vicinity of the cathode sheath and pre-sheath regions, measurements were made at every 2 mm. The probe loop diameter was 2 mm, therefore measurements for z < 5 mm were, to some degree, spatially averaged.

The deposition rates of sputtered titanium were measured along the same line as the V_p measurements but only from 30 to 100 mm using a Maxtek TM-400 multi film deposition monitor (equipped with a 6 MHz quartz crystal oscillator and silver sensors). Although the deposition rate varies during the pulse, the slow response of the sensor allows only time-averaged values to be determined (in our case from the total thickness measured in the fixed chosen deposition time of 120 s). A schematic diagram of the magnetron arrangement together with the positions of the emissive probe and deposition rate monitor is shown in figure 2.2 (Chapter 2).

One important region of the discharge is the magnetic trap, indicated in the figure 2.2 (Chapter – 2) and defined by a region enclosed by magnetic field lines that intersect the target twice. The construction and electrical arrangement of emissive probe has been described in section 3.1.4 (Chapter 3).

To investigate the effect of magnetic field strength (B) on the temporal and spatial evolution of V_p and the deposition rate ρ_d, measurements were carried at three different magnetic field configurations (1, 2 and 3) as shown in figure 4.1 – 4..3.

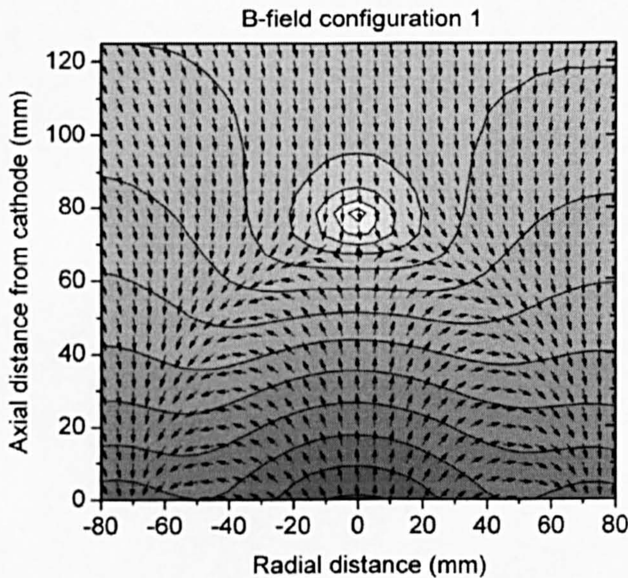

Figure 4.1 *The measured magnetic field (flux density B) and field line directions for magnetic field configuration 1 (magnets were situated at 0 mm behind the cathode). Normalized arrows indicate the B-field direction, gray scale is the magnitude of magnetic field B.*

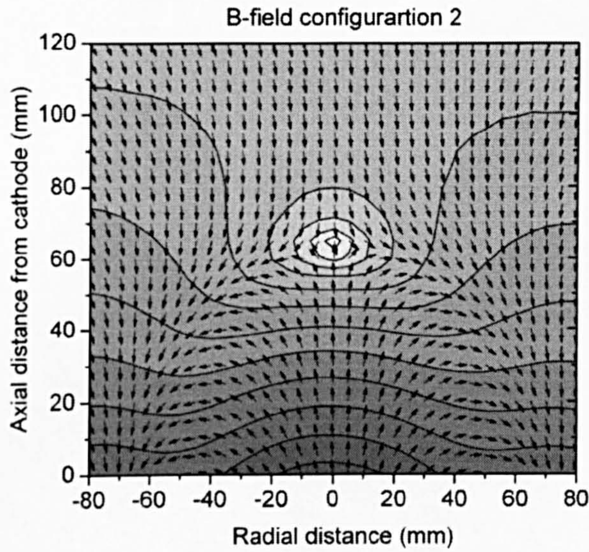

Figure 4.2 *The measured magnetic field (flux density B) and field line directions for magnetic field configuration 2 (magnets were situated at 5 mm behind the cathode). Normalized arrows indicate the B-field direction, gray scale is the magnitude of magnetic field B.*

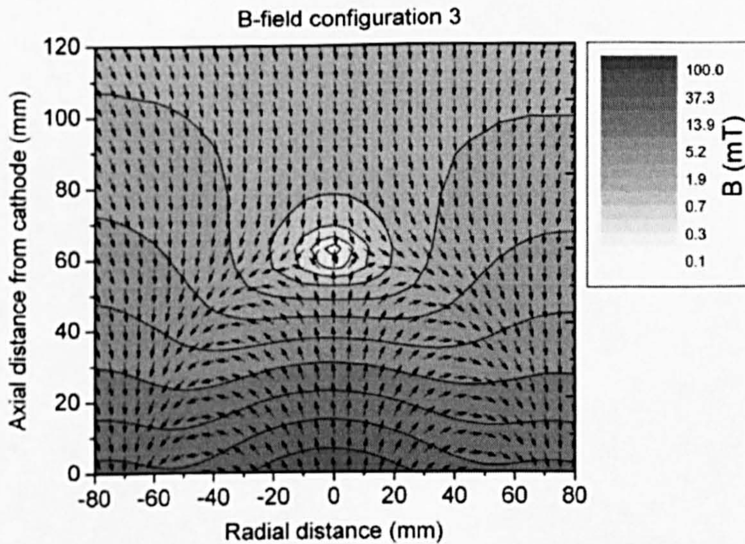

***Figure 4.3**: The measured magnetic field (flux density B) and field line directions for magnetic field configuration 3 (magnets 10 mm behind the cathode). Normalized arrows indicate the B-field direction, gray scale is the magnitude of magnetic field B*

These field strengths and directions have been determined from bench measurements of magnetic field taken in the axial (B_z) and radial directions (B_r) using a Hall probe. By pulling the magnets back behind the target, we were able to progressively lower the field strengths. Also we see that the position of the null in the magnetic field on the discharge centre line moves by 20 mm towards the target from configuration 1 to configuration 3. The magnitude of total B-field ($|B| = \sqrt{(B_z^2 + B_r^2)}$) along the line of V_p measurement is shown in figure 4.4. As the magnets were withdrawn B dropped by 33% at the target.

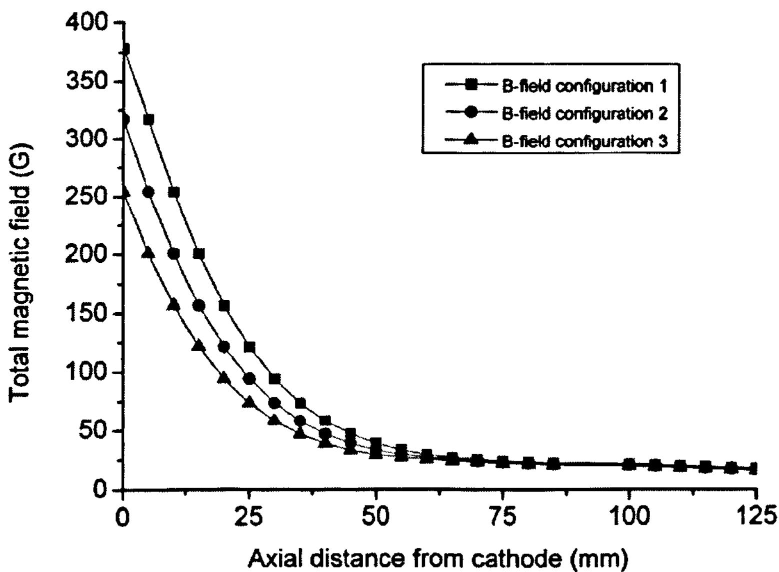

***Figure 4.4**: The total B-field $|B| = \sqrt{(B_z^2 + B_r^2)}$ for the 3 different magnet positions behind the cathode.*

The cathode voltage (V_d) and current (I_d) waveforms were measured at an intermediary aluminum test box placed between power supply and magnetron source using a x 100

voltage probe (P5100 Tektronix Ltd model) and a x 20 current probe (Tektronix Ltd Model TCP 04) in conjunction with x 10 current probe (Tektronix Ltd Model TCP 202) respectively. The reference time t = 0 was defined as the zero voltage crossing point between the 'off' and 'on' phases of the V_d pulse. Example V_d and I_d waveforms are shown in figure 4.5. In this case, an average discharge power of 650 W, a gas pressure of 0.54 Pa and magnetic field configuration 1 was chosen as shown in figure 4.1.

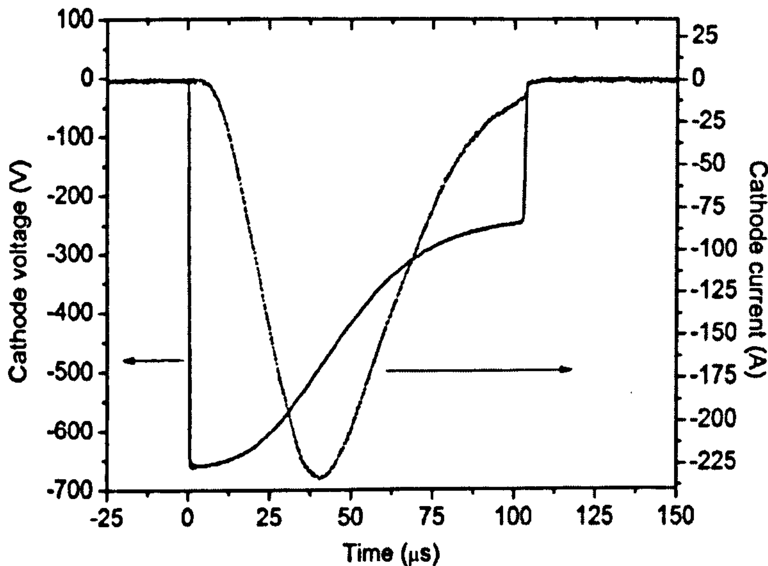

Figure 4.5. The cathode voltage (V_d) and current (I_d) waveforms produced by the SINEX 3.0 HiPIMS power supply for an average discharge power of 650 W and a gas pressure of 0.54 Pa.

From the figure 4.5 we see that in the initial phase, V_d ramps down rapidly from 0 to - 650 V in 200 ns, then relaxes somewhat to reach -600 V in next 20 μs. After this, V_d increases up to 0 V in 100 μs. I_d lags V_d, having a maximum value of 230 A which occurs 40 μs after initiation of the discharge pulse.

4.1.3 Results and discussion

4.1.3.1 Loop Current versus Floating Potential

In a preliminary experiment, the floating potential sampled by the emissive probe was measured as a function of heating current I_h up-to and past the point where full electron emission was expected. This was done for the probe positioned at z = 100 and for three different times during the pulse and these are shown in figure 4.6. The chosen times correspond to three structures we name as 'first peak', 'second peak' and the 'stable off phase.'

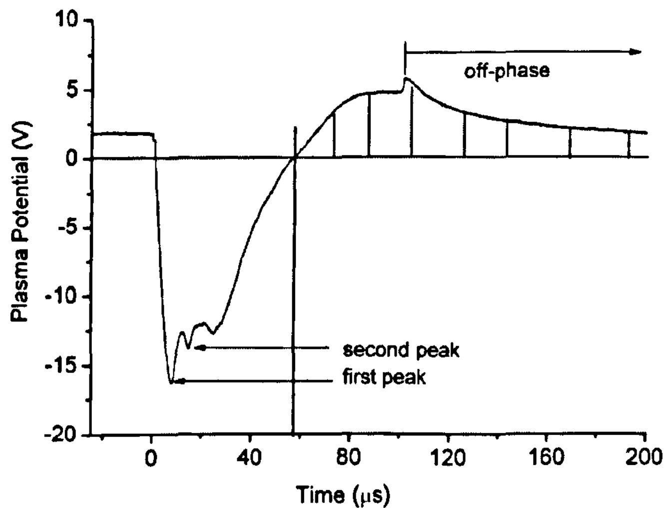

Figure 4.6. A plot of the time-evolution of typical plasma potential (V_p), measured at one position (z = 100 mm and r = 45), at an average discharge power of 650 W and a gas pressure of 0.54 Pa in B-field configuration 1. Here, we identify the "first peak", "second peak" and "off-phase". At the time of t = 57 μs V_p goes above the ground as shown by vertical line.

As we see in figure 4.7 the floating potential V_f saturates above a certain current I_h (~1.75 A) and we can therefore assume full electron emission has been achieved for all times during the pulse at this current.

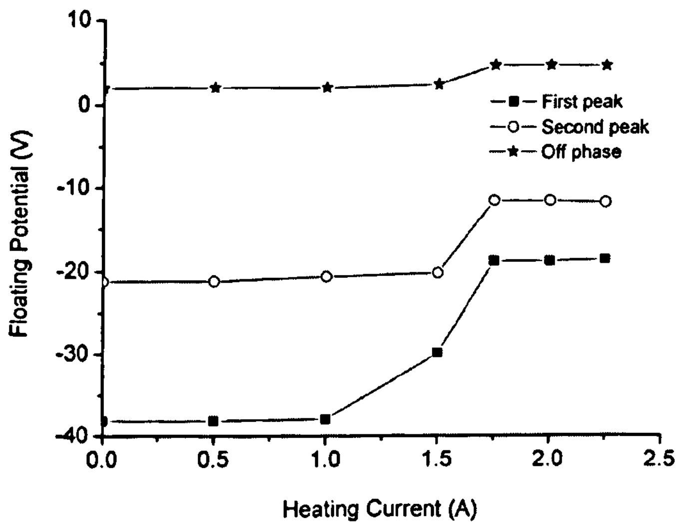

Figure 4.7: *A plot of measured emissive probe floating potential (V_f) versus loop heat current (I_h) at one position (z = 100 mm r = 45 mm) during three identified phases in the V_f waveform: (a) the "first peak" (b) "second peak" and (c) "off-phase", as described in figure 5.6. It should be noted that at $I_h > 1.75$ A, the floating potential V_f approaches to the plasma potential V_p. All the measurements were performed in B-field configuration 1*

This gives us confidence that the measured floating potential V_f represents well the true value of V_p. For currents below 1.75 A, it was found that a considerable amount of structure in V_p was not revealed, particularly during the "second peak" occurring at times between 15 and 18 μs after the initiation of the pulse.

4.1.3.2 Plasma potential versus Probe Plane Orientation

Another important consideration was the presence of the magnetic field, which as already indicated could affect the V_p measurements. Generally, in magnetron discharges, the electrons are magnetised, but the ions are not which can be written as the condition $r_e < r_p < r_i$ where r_e and r_i are the electron and ion Larmor radii and r_p is thr probe radius. Since the emitted cold electrons from the probe have energies typicaly only twice of the binding energy (a few eV) they will be magnetised at positions of large B in the discharge and therefore the orientation of the probe loop relative to the local B field may have an influence on their transport from the probe and hence the inferred value of V_p [86].

We investigate the emission characteristics of the probe and the V_p values for three different probe orientations relative to the B-field. To do this, we define the normal vector to the probe loop $\hat{n}$ and investigate V_p for angles $\theta = 0^0$, 45^0 and 90^0, where θ is the angle between $\bar{B}$ and $\hat{n}$ vectors. Measurements of V_p are made at these three angles and at two different positions in the discharge, one close to target, z = 30 mm (inside the magnetic trap) where B = 11.54 mT and the second at z = 90 mm (outside the magnetic trap) where B = 2.38 mT. These two axial locations were chosen since at z = 30 mm the bulk plasma electrons are magnetised ($r_e < r_p$), however, at z = 90 mm they are un-magnetized ($r_e > r_p$). As we see in figure (4.8) at z = 90 mm rotating the probe relative to the B-field has only a small effect (typically ~ 1 V) on V_p value, however there is a significant effect (typically ~ 12 V) at z = 30 mm. When the B-field is normal to $\hat{n}$, ($\theta = 90^0$) the transport of emitted electrons is restricted, as electrons can

not readily cross the field lines and escape into the plasma bulk, however when $\hat{n}$ is parallel to B ($\theta = 0^0$) the emitted electrons can be swept away along the fields line to the boundaries or bulk plasma.

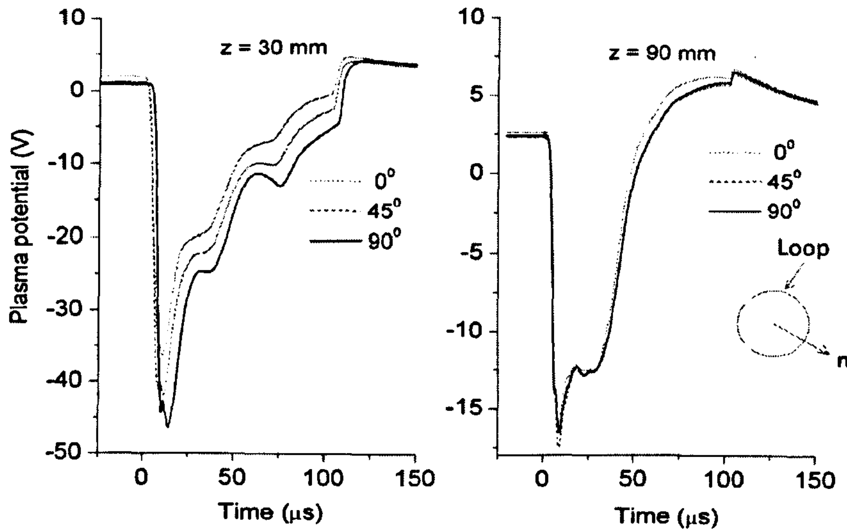

Figure 4.8 : The time evolution of the emissive probe floating potential at r = 45 mm versus probe loop orientation angle θ, ($\theta = \frac{\vec{B}.\hat{n}}{|\vec{B}|.|\hat{n}|}$ where $\hat{n}$ is normal to the probe loop plane and B is the local magnetic field vector as shown in figure 5.1-5.3) for probe positions (1) z = 30 mm and (2) z = 90 mm. All measurements were performed in B-field configuration 1.

We therefore chose to orientate the probe at $\theta = 0^0$ in all subsequent measurements of V_p.

4.1.3.3 Evolution of the plasma potential

This section describes the one dimensional plasma potential evolution and its relationship with deposition rate.

4.1.3.3.1 Axial distribution in Plasma Potential (V_p)

Figures 4.9 – 4.11 show the spatial distribution of the plasma potential V_p (from z = 2 to 100 mm) at the three chosen times during the pulse, namely at the 'first peak' (t = 6-8 μs) the 'second peak' (t = 15 - 18 μs) and during the 'stable off phase' (t = 120 μs). This was done for magnetic configuration 1 and for argon pressures of 0.54 and 1.08 Pa and average discharge powers of 650 and 950 W. In the case of the 'first peak' (figure 4.9) we see the establishment of a deep plasma potential V_p close to the cathode.

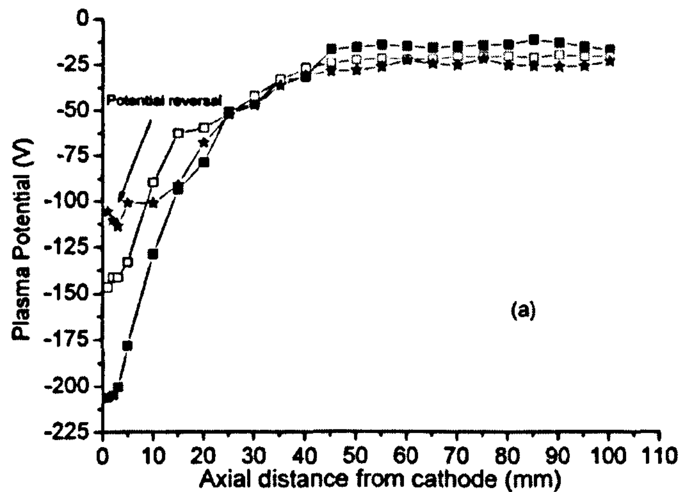

*Figure 4.9 Plot of V_p versus axial distance z from the cathode for the phase identified as "first peak" in figure 5.6. All these measurements were carried out at three different operating conditions are considered: ■ pressure of 0.54 Pa and average power of 650 W, □ pressure of 1.08 Pa and average power of 650 W and * a pressure of 1.08 Pa and average power of 950 W. All these measurements were performed in B-field configuration 1.*

This is particularly clear in the inside the magnetic trap (z = 0 to 40 mm) for the lowest pressure (0.54 Pa) and power (650 W) where V_p reaches – 210 V closes to the cathode (z = 2mm). This extremely negative value is reduced somewhat with increasing pressure and power, for example, V_p only reaches – 110 V at 1.08 Pa and 950 W.

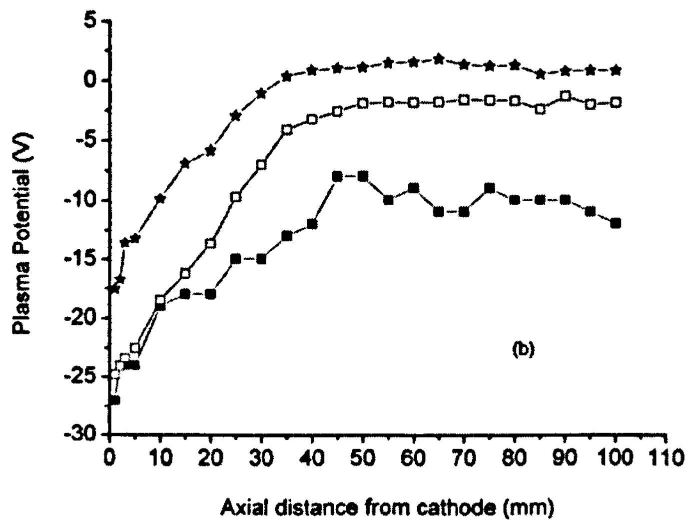

Figure 4.10 *Plot of V_p versus axial distance z from the cathode for the phase identified as "second peak" in figure 5.6. All these measurements were carried out at three different operating conditions are considered: ■ pressure of 0.54 Pa and average power of 650 W, □ pressure of 1.08 Pa and average power of 650 W and * a pressure of 1.08 Pa and average power of 950 W. All these measurements were performed in B-field configuration 1.*

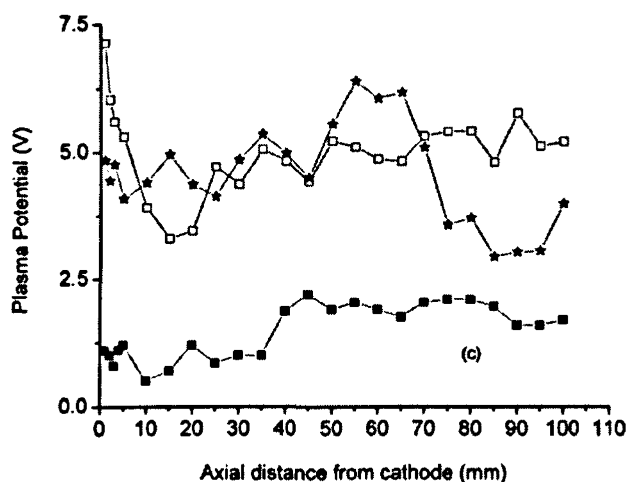

*Figure 4.11: Plot of V_p versus axial distance z from the cathode for the phase identified as "off phase" in figure 5.6. All these measurements were carried out at three different operating conditions are considered: ■ pressure of 0.54 Pa and average power of 650 W, □ pressure of 1.08 Pa and average power of 650 W and * a pressure of 1.08 Pa and average power of 950 W. All these measurements were performed in B-field configuration 1.*

It is worth mentioning that the target potentials themselves (V_d= -650 and -900 V) are not shown in figures and from the plots it is not possible to say if these deep potential are actually part of an extended sheath or constitute anomalously high pre-sheath potential values. That is, we cannot define or locate the position of the sheath-edge. If we estimate a remnant plasma density of 1 x 10^9 cm^{-3} [54] then –650 V on the cathode would produce a matrix sheath extension of 6 mm, and in principle we would see this in the plots. However, this assumes a non-magnetised matrix sheath and predictions for the sheath extension with B-fields up to 300 or 400 G at the cathode are hard to make.

Similar but smaller potential drops to those seen in figures 4.9 and 4.10 have also been reported in pulsed DC magnetron plasmas above the racetrack [82]. Clearly, the large

potential drops constitute a large axial electric fields E_z in the plasma bulk particularly inside the magnetic trap (z = 5 mm) where we estimate E_z ~ several 10's of kVm^{-1}. Outside this trap (z = 65 mm) however, we have E_z ~ < 0.5 kVm^{-1}, which is consistent with the typical negative glow region in a magnetron. The strong axial electric field at the early stage of the pulse (t < 8 μs) may accelerate any residual ions from the end of the previous "off- time" towards the target so initiating sputtering.

Interestingly, in this phase of the pulse we see a "triple-layer-like" feature in the V_p profile close to the cathode (z = 5 mm). This is a distinct potential well which has formed locally in the plasma potential structure [90]. For the case of 1.08 Pa pressure and 950 W power, this well has a depth of –10 V. The structure is labeled in figure 4.9 as a 'potential reversal'. Although this feature might be an artifact of the measurement technique i.e. due to the perturbation of the plasma as the probe approaches the cathode, it has been seen in other pulsed magnetron plasmas [19] and may warrant further investigation. In this early phase of the pulse, V_p never reaches ground potential even with increased distance from the cathode.

The axial distribution of V_p during the "second peak" (t ~ 15 - 18 μs) is shown in figure 4.10. It has similar characteristics to the "first peak" however V_p falls to much less deep voltages (- 20 V) close to the cathode. We can see clearly that for distances z < 40 mm (inside the magnetic trap) substantial E fields exist (E ~ 0.4 kVm^{-1}) while at greater extensions (outside the magnetic trap) E → 0. In contrast to the "first peak" in this phase V_p does go above the ground potential for z > 40 mm but only in the particular case of 1.08 Pa operating pressure and an average power of 950 W. Figure

4.11 shows the axial distribution of the V_p corresponding to the 'off-phase'. Here V_p varies little with distance, with values slightly above ground. The highest values are seen to increase with pressure and average power. An interesting observation in the "on-time" driven phases of the pulse is that the profiles in V_p become flat for $z > 40$ mm ($E \sim 0$) whereas for distances $2 < z < 45$ mm the plasma is characterised by large E fields. From figure 4.11 we see that the plasma potential remains at few volts above ground (~ +2 V) in the "off-time" which suggests that the plasma decays only slowly in the afterglow. In fact, looking at figure 4.6 it appears that plasma remains during the entire "off-time" with V_p sitting above ground, producing a weak ion sheath at the cathode, which itself is maintained at 0 V. This effect will provide remnant plasma so seeding the subsequent "on-time" ignition.

4.1.3.3.2 Temporal Evolution of Electric Field in the Bulk Plasma

To illustrate the dynamic nature of the electric field structure of the discharge, the instantaneous axial electric field $E_z = -dV/dz$ has been calculated as a function of time for positions both inside and outside the magnetic trap. This has been done for B-field configuration 1 and pressure 0.54 Pa and average power 650 W. Figure 4.12 shows E_z averaged over positions from 5 to 10 mm and from over 65 and 70 mm. For the former, E_z peaks at 11.5 kV m^{-1} at around t = 8 μs, however this does not correspond to the time of maximum change in cathode voltage V_d which occurs for times t < 200 ns. The calculated values of E_z are much smaller outside the magnetic trap for instance at t = 6 μs, $E_z \sim 0.4$ kV m^{-1}. In the "off-time" of the pulse (t > 100 μs) E_z collapses in both regions, inside and outside the trap.

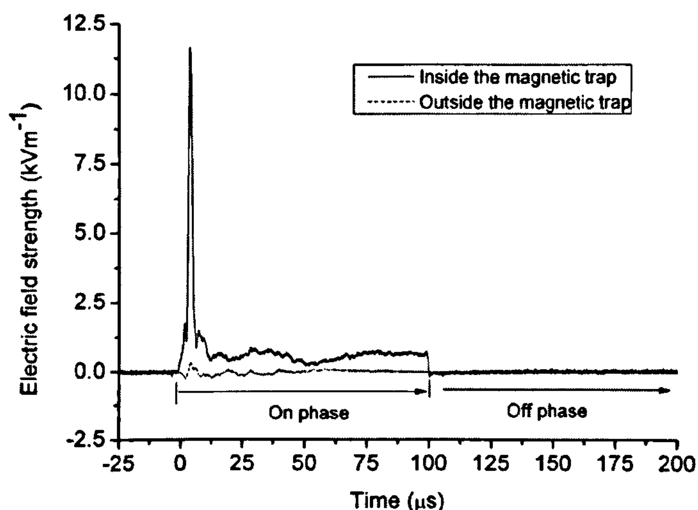

Figure 4.12: A plot of the temporal-evolution of the mean axial electric field strength (E_z) inside the magnetic trap (z = 5 mm), shown by solid line and outside the magnetic trap (z = 65 mm), shown by the dotted line. All the measurements were carried out in B-field configuration 1.

Examination of figure 4.12 reveals that for a considerable fraction of the "on-time" the very large axial electric fields in the magnetic trap will oppose the motion of positive ions (argon and post-ionised sputtered particles) travelling from target to substrate. Positive ions would need energies in excess of 190 eV at times up to t = 8 μs and 30 eV for times up to t =18 μs to overcome this repulsive potential. We should point out at these times the discharge current and plasma density have not built up yet (see figure 4.5) and relatively few ions will be created. However, even towards the end of the "on-time", ions with energies below 20 eV cannot overcome the potential barrier to leave the trap. In contrast, ions created outside the trap will see only a weak axial electric field in front of them, with little or no barrier to overcome (e.g. V_p drops from -22 to -15 V for t = 6 to 8 μs i.e. during the 'first peak' phase). Therefore Ti neutrals with only a few volts of forward kinetic energy, ionised outside the trap can readily reach the

substrate (grounded or negatively biased). It is these ions that form the bulk of the deposit in HiPIMS and have been detected by energy-resolved mass spectrometry [24, 91]. Substantial metal ionisation will only occur once the discharge current I_d reaches its maximum value which happens at t = 40 µs as seen in figure 4.5.

4.1.3.3.3 Spatial-temporal evolution of the Plasma Potential (V_p)

It is instructive to plot V_p against both time and the distance to reveal the major transient features in the evolution of the potential structure. However, as we shall see, by doing this, much of the finer detail in V_p will be lost (e.g. the "second peaks" as observed in figures 4.9 - 4.11. Figures 4.13 - 4.15 show V_p plotted in contour form for different average power and pressure settings, together with in each case plots of the associated discharge voltage V_d and current I_d waveforms, synchronized in time to the V_p plots above them. All three plots have been made for magnetic configuration 1 and reveal similar trends. The time axis is plotted logarithmically to reveal detail in V_p occurring at small times.

These interesting features can be summarized as follows. The greatest concentration of contours occurs at positions close to the cathode indicating deep potentials generated in the plasma bulk above the racetrack. For instance, in figure 4.14 at a pressure of 0.54 Pa and average power of 650 W, we see V_p values down to – 210 V at z = 2 mm and t = 6 µs.

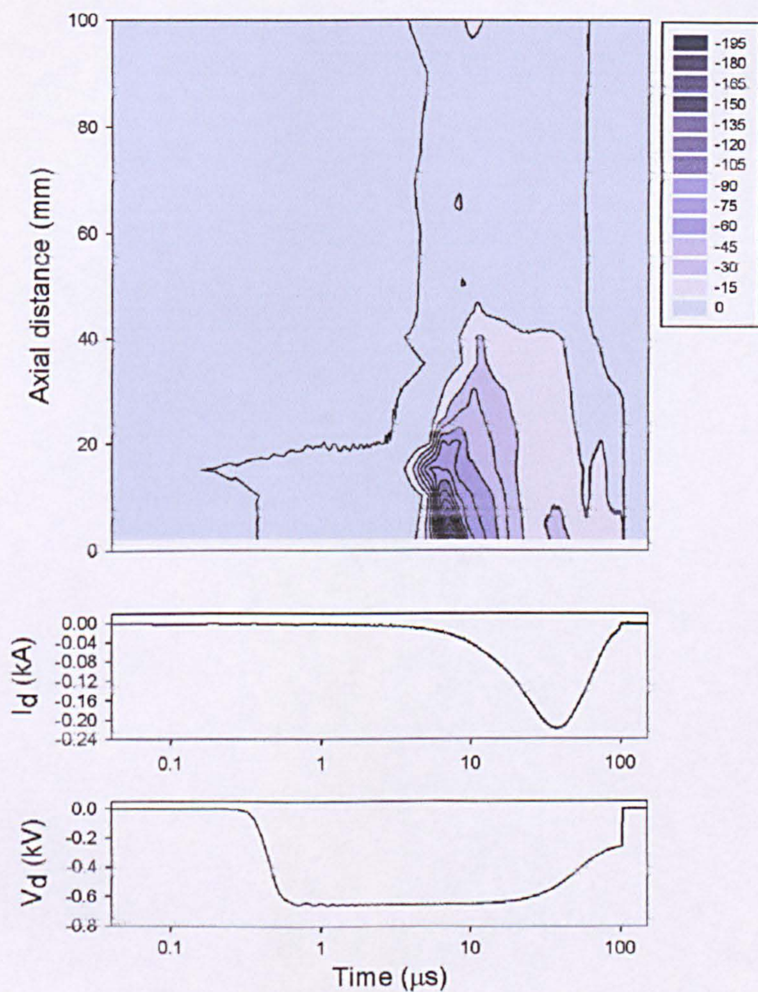

Figure 4.13 *Contour plot of the spatial-temporal evolution of the V_p at a pressure of 0.54 Pa and an average power of 650 W. The time axis is in logarithmic scale. All the measurements were carried out in B-field configuration 1.*

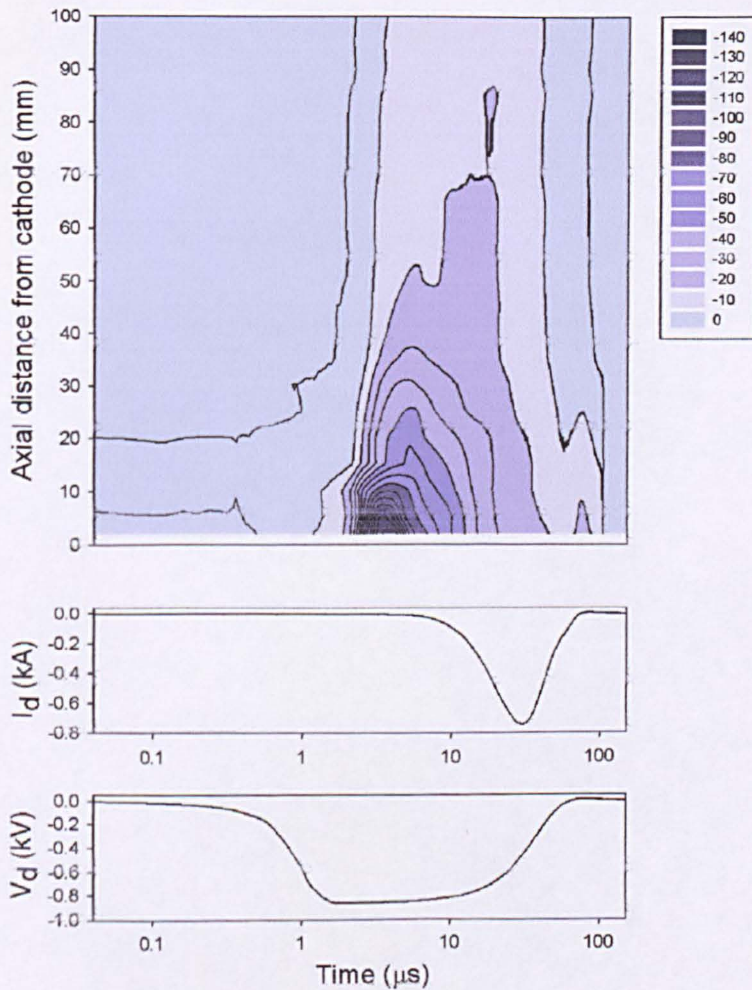

Figure 4.14 *Contour plot of the spatial-temporal evolution of the V_p at a pressure of 1.08 Pa and an average power of 650 W. The time axis is in logarithmic scale. All the measurements were carried out in B-field configuration 1.*

With increasing pressure or average power these minimum potentials are elevated. Deep values of V_p only occur in the magnetic trap ($z < 40$ mm), with V_p values outside the trap typically between -10 and +10 V.

It is interesting that comparing the discharge voltage V_d with times of deepest V_p that there is a delay between the establishment of the plasma potential structure in the bulk and V_d as it is ramped down to its maximum value. For a pressure of 0.54 Pa and average power of 650 W this delay time is 6 to 8 μs however this shortens with increasing pressure and power to < 3 μs for example at 1.08 Pa and 950 W. Clearly in these early periods (t < 10 μs) much of the full cathode fall potential $\Delta V \sim -650$ V must be contained within the 2 mm of the sheath adjacent to the target, which cannot be resolved using this probe.

Also, we see that once the plasma potential becomes established (after a few μs) there are very rapid changes in V_p occurring in the plasma over large distances, up to about 40 mm. That is, the contours are nearly vertical (e.g. at t ~ 5 μs and t ~ 50 μs) in figure 4.13. This shows the bulk potential structure changes almost simultaneously from positions close to the cathode up to the maximum extension of the magnetic trap. Another phenomenon is apparent from the contour plots, which is particularly clear in figure 4.15, is that V_p contours inside the trap have a negative slope, e.g. from z = 20 mm back to the cathode as time increases from t = 2 to 20 μs. This feature is also observed in figure 4.13 and 4.14 but to lesser degree, however the data strongly indicates that deep potentials can first occur at remote positions from the target (i.e. in the bulk plasma) and propagate back towards the cathode.

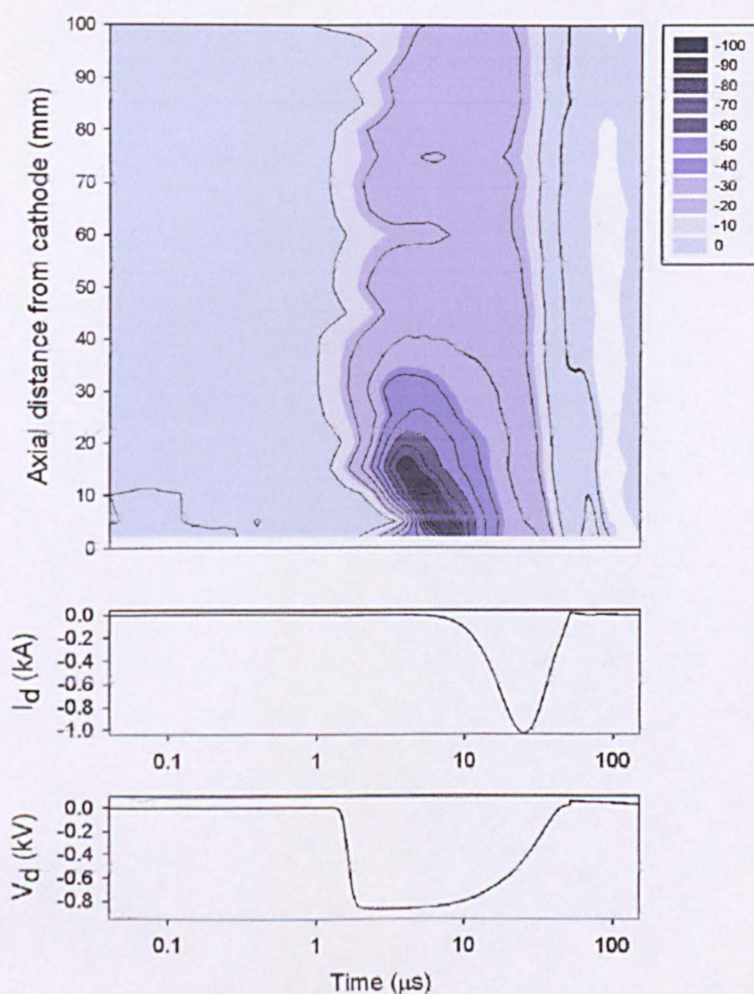

Figure 4.15 *Contour plot of the spatial-temporal evolution of the V_p at a pressure of 1.08 Pa and an average power of 950 W. The time axis is in logarithmic scale. All the measurements were carried out in B-field configuration 1.*

The effective speed of this backwards propagation in V_p (figure 4.15) is 20 mm/ 5 μs ~ 4×10^3 ms^{-1}. This speed is calculated to be somewhat smaller (~ 1.4×10^3 ms^{-1}) at lower pressures and powers, see figure 4.13, but is consistent with the ion acoustic speed for an electron temperature of 1 eV. Not only do we see backward propagation in

V_p, but for times between t = 25 to 40 μs and for positions z > 20 mm V_p also propagates forwards into the bulk plasma, e.g. this can be seen well in figure 4.13 and from the slope of the V_p contours a forward speed of ~ 1.2 x 10^3 ms^{-1} estimated. The potentials involved here are much smaller in magnitude than those observed propagating backwards, typically about 10 V.

To explain why the backward propagation first occurs at positions remote from the target (e.g. z = 10, 12 and 20 mm as seen in figures 4.13-4.15 respectively), it would require a perturbation in the local space-charge to develop in the bulk, self-consistently producing the observed V_p structure. We do not understand the origin of our observation but one plausible theory is that hot electrons generated during the initial cathode sheath expansion (t = 0 - 200 ns) may be transported to relatively deep positions into the plasma where they alter the space-charge balance. The distance of penetration of such electrons with energies up to the cathode fall potential may be defined either by their collisional mean-free-path or the extension of their cyclic orbit in the orthogonal E and B fields, whichever is the shorter. Such sheath expansion (or electron acceleration) has been invoked before to explain the existence of hot electrons in the pulsed DC magnetron [24] and are the subject of a recent paper for HiPIMS [90]. Some evidence of the sheath can be in seen in figure 4.9 for t = 5 μs and z < 5 mm, however we still cannot explain why we observe relatively large delays between the full establishment of V_d and the first changes in V_p. From each of the plots in figures in 4.13 - 4.15, it is clear that when I_d reaches its maximum value (~ 220, 290, 880 A respectively) V_p is negative inside the magnetic trap (z < 40 mm) but approaches ground potential outside the trap (z > 40). In other recent experiments [90] we have

observed that the plasma density builds up to its maximum value typically 10 μs after the maximum in I_d and during this time we see from figures 4.13-4.15 that the plasma potential is positive at a distance far from the cathode. In figure 4.13 we see V_p goes above ground for $z > 65$ mm. So, at the time when the production of ionic species in the discharge (argon and post-ionized sputtered neutrals) is at its highest, the plasma potential is negative in the trap (typically – 15 V) and close to ground or slightly positive in bulk. As we can see from figure 4.13 – 4.15 close to the target ($2 < z < 25$ mm), the V_p distribution are sensitive to pressure and average power with the density and slope of the contours increasing with power and pressure.

The general trends of deep plasma potentials and strong axial electric fields in the plasma bulk, similar to those observed here, have been predicted using a PIC–MMC model by van der Straaten et. al. [92]. However they considered the case of a low-density DC cylindrical magnetron. The large potential drops across the plasma observed in [92] are explained as being due to the buildup of negative space charge within the magnetically confined plasma. This switches the potential profile from the classical positive space charge (PSC) regime with narrow cathode fall and almost flat V_p profile in pre-sheath and bulk plasma to a negative space charge (NSC) regime with anomalously high bulk electric fields. The negative space charge is a consequence of resisted transport of electrons across the magnetic field in a regime where the electron cyclotron frequency ($\omega_e = eB/m_e$ with B the local magnetic field strength and m_e is the electron mass) >> ν, the momentum stopping collision frequency. In our experiment with magnetic fields of up to 430 G at the target (falling to 70 G at $z = 40$ mm) and low operating pressures (up to a maximum of 1.08 Pa), such a NSC regime may exist in the

magnetron particularly within the magnetic trap. From figure 4.9 – 4.11 we observe that the V_p profiles become less steep (i.e. the electric field E_z reduces) in the trap region as the pressure and average power are increased. Such a change with pressure is consistent with the general finding of [92]. It is conceivable that at higher average powers (higher currents) the diamagnetic drift current will be greater so lowering marginally the local B field above the racetrack. This phenomenon is described in [93] for DC magnetrons and is observed directly using a magnetic probe in a pulsed DC magnetron [94] in which B was found to change by a few percent. Lower B-fields lead to more PSC conditions and flatter V_p profiles. One important consequence of the large axial electric fields in the bulk plasma (directed towards the target) existing for a considerable part of the pulse "on-time" is that ionised material may be hindered from reaching the substrate (at ground or a biased potential). This effect, which acts to limit the deposition rate ρ_d, is explored in more detail below.

4.1.3.4 Relationship between Plasma Potential, Magnetic Field Strength and Deposition Rate

To investigate how changes in the magnetic-field intensity B over the trap region affect the electrical structure of the plasma, measurements of V_p were made for the three different magnetic field configurations described in section 4.1 – 4.3. The pressure was fixed at 1.08 Pa and the average power maintained at a value close to 680 W. The variation in average power between the different field configurations was 8%. To obtain nominally the same power at the different magnetic field strengths, the voltage setting on the power supply needed to be changed leading to different V_d and I_d

waveforms in each case, however we have managed to achieve similar averaged power levels. Figures 4.16 and 4.17 show the profiles of V_p during the "first peak" (t ~ 6 – 8 μs) and the time of maximum discharge current (t ~ 35 to 40 μs) for the three cases respectively.

Clearly, we see in both figures namely 4.16 and 4.17 that lowering the overall magnetic field strength reduces the drop in potential over the trap region and raises the V_p profiles generally to more positive values. At the "first peak" stage of the discharge, figure 4.16 shows that a 33% change in B at the target (this changes reduces with increasing distance along the line of measurement inside the trap) leads to almost a 40 V rise in V_p at z = 10 mm. Later in the pulse, when the plasma is better established, we also see such a rise in V_p, but by 15 V, see figure 4.17.

In terms of the electric field in the trap, there is a decrease in E by a factor of 3.5 in the discharge initial stage and a factor of 1.5 in the denser plasma at the time of maximum current when we go from magnetic field configuration 1 to configuration 3.

Outside the magnetic trap, the V_p profiles are almost flat at the two chosen phases of the discharge, the only variation being that V_p is raised to more positive values with decreasing B. It is interesting to note that the triple layer-like structure [91] observed in figure 4.16 is also seen for all three magnetic field configurations for z = 10 mm, however here we have less measurement points and less spatial resolution.

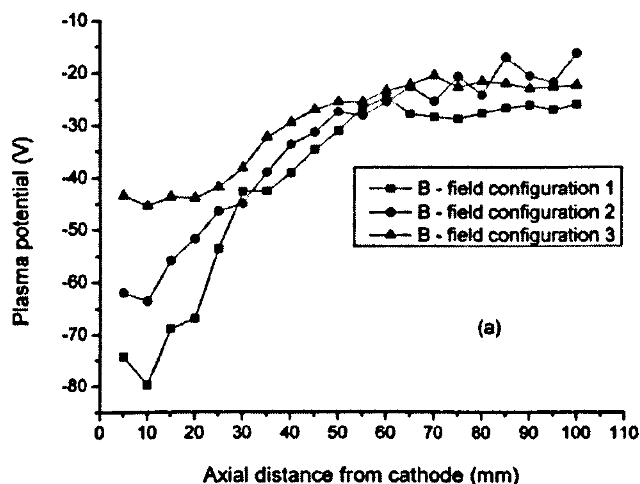

Figure 4.16 A plot of V_p versus axial distance z from cathode at the time when "first peak" occurs. In each plot the three different B-field configurations as shown in figure 5.2 are used. All the measurements were carried out at an average discharge power of 750 W, a gas pressure of 1.08 Pa and above the racetrack (r = 45 mm).

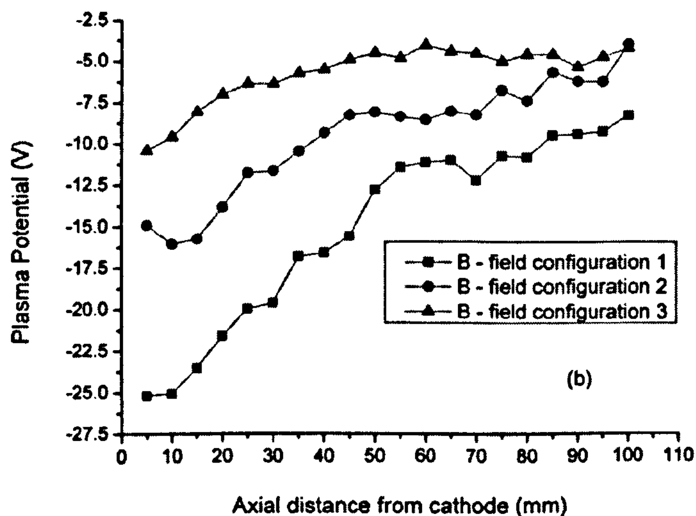

Figure 4.17 A plot of V_p versus axial distance z from cathode at the time when the peak in the discharge current (I_d) occurs. In each plot the three different B-field configurations as shown in figure 5.2 are used. All the measurements were carried out at an average discharge power of 750 W, a gas pressure of 1.08 Pa and above the racetrack (r = 45 mm).

In HiPIMS a significant fraction of the deposition flux is made of ionised metal we anticipate that the large potential differences observed across the plasma in figures 4.9 – 4.11 will constitute a potential barrier so preventing some of the ions from reaching the substrate and hence affecting the deposition rate.

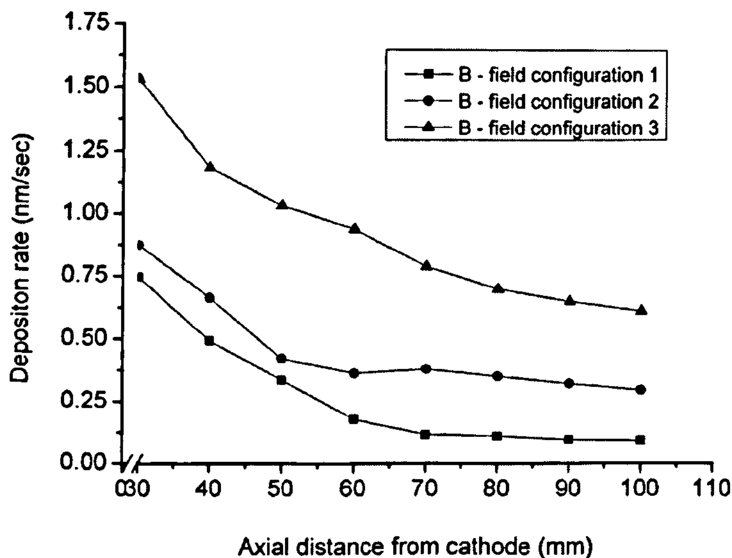

Figure 4.18: A plot of titanium deposition rate measured using a quartz crystal micro-balance (QCM) at different axial positions above the racetrack (r = 45 mm) for the three different B-field configurations as shown in figure 3. The average discharge power was 750 W and the gas pressure was 1.08 Pa.

To test this, the Ti deposition rates were measured at a number of positions (from z = 30 to 100 mm) on an equivalent line as V_p using the deposition meter as described in section 2. This sensor was electrically grounded and acted like a small substrate. These results are shown in figure 4.18.

The most striking result is that as the mean magnetic field over the trap region is lowered (e.g. by 33 % at z = 0 mm and 30 % at 40 mm), the deposition rate ρ_d increases by up to a factor of 6 at a typical substrate position z = 100 mm. The typical deposition rates for configuration 1 (~ 0.1 nm/s up to a maximum of ~ 0.75 nm/s) are significantly lower than those of 2 nm/s measured in the same magnetron but operated in DC mode. We argue that the decrease in deposition rate with increasing B is a direct consequence of increased height of the effective potential barriers existing in the trap region preventing some of the ions reaching the deposition meter. Since the average power, denoted by the integral of the product of V_d and I_d, over the pulse cycle is almost the same for the three magnetic field configurations (only an 8% variation) then the sputter rate will not vary much between the three cases. This can be argued simply by considering the sputter yield to be roughly a linear function of target voltage V_d and the ion bombardment rate to be proportional to I_d. Therefore the time integrated product of V_d and I_d gives a global sputter rate which is essentially invariant in this experiment. Ti neutrals will be sputtered from the target with a range of energies (from twice the binding energy to the maximum close to the Ar^+ or Ti^+ bombarding energies) defined by the Sigmund-Thompson distribution [94] $f(E) \sim E(E_b+E)^{-3}$ where E is emitted neutral particle energy and E_b is the binding energy. These neutrals will be ionised at different positions between the target and the substrate and hence at different plasma potentials (since V_p varies strongly in space). Depending on their initial energy (at the target) and position of their creation, ions may or may not be able to surmount the potential barrier established in the bulk plasma to reach the substrate. For magnetic configuration 1 when I_d is a maximum (t = 38 μs) V_p has a drop across the plasma of

12.5 V. For Ti sputtered at the target by (argon or Ti) of 650 eV, 8% of the emitted neutrals will have an energy > 12.5 eV [94]. All these ions will overcome the potential hill irrespective of their position of creation. However, with this argument we can see how that a significant proportion of Ti ions with low initial energies (in the sputter distribution f (E) or those created at deep plasma potentials near the cathode may never overcome the barrier and so return to the cathode. The self-sputtering probability is clearly enhanced in this scenario. The presence of such potential barriers is expected not to be so critical in determining the deposition rate in conventional magnetron sputtering plasmas where neutrals are the key depositing species rather than ions.

The increase in the potential drop across the plasma with increased B-field strength may be a consequence of the increased confinement of plasma and secondary electrons from the cathode in the magnetic trap region. As the B-field strength increases the effective cross-field transport rate of these electrons decreases, which pushes the discharge further into the negative space charge NSC regime as described in [92, 97].

4.1.4 Conclusions

Time-resolved plasma potential (V_p) measurements have been carried out in a HiPIMS discharge pulsed at 100 Hz using an emissive probe operating in the "saturated floating potential mode". We identify three distinct phases in the evolution of V_p (a "first peak", "second peak" and "stable off-phase"). In the initial phase of the voltage pulse, t = 6 - 8 μs, large potentials (-210 V) are generated across the plasma bulk particularly inside the magnetic trap. Outside the trap, V_p has typically a flat profile. As time progresses, V_p becomes more positive everywhere and (after about 55 μs) it is elevated

to values above ground potential outside the magnetic trap. In standard conditions (Ar pressure 0.54 Pa and 650 W average power), the results show that for over 50% of the 100 μs plasma "on-time" the spatial structure of V_p provides a large potential barrier for the sputtered ionized species so impeding their transport and deposition at the substrate. At times of the peak discharge current this barrier can be reduced from 45 to 12.5 V during the 'first peak' phase by lowering the magnetic field strength (33% at the target) so increasing the deposition rate by a factor of 6 some 100 mm from the target. The temporal and spatial structure of V_p is marginally sensitive to changes in pressure (over the range 0.54 to 1.08 Pa), but more strongly dependent on the applied power (over the range 650 to 950 W). The results demonstrate that the magnetic field strength (and possibly its shape) are critical factors in determining the overall electrical structure of the HiPIMS discharge and therefore the deposition rate, since in these discharges the deposition flux can be composed primarily of ions rather than of neutrals.

4.2 Evolution of Plasma Potential in Two Dimensions and E × B drifts

This section describes the two dimensional evolution of plasma potential $V_p(z, r)$ and $E \times B$ drifts throughout the bulk plasma.

4.2.1 Introduction

A bulk plasma model developed Brenning et. al. [97] provides the physical insight of the processes occurring in the discharge such as structure and time evolution of plasma currents, electric fields and potential profiles. They reported that the transverse

resistivity $\eta_{\perp}$ plays an important role in the evolution of the potential profile and the transport of the ionized target material through the bulk plasma. Many experimental studies have been carried out to accomplish this purpose. This transverse resistivity ($\eta_{\perp}$) is a probable cause for the radial transport of the plasma ions.

As the plasma potential is an important parameter of the discharge volume that determines the electric field structure in the discharge and accelerates the electrons to sustain the discharge. Therefore the spatial distribution of V_p is crucial for the discharge formation and distribution. The value of V_p in-front of the electrode or wall also determines the energy of the bombarding ions onto the substrate and controls the charge flux to the substrate and, in turn, effects the properties of thin films deposited. Therefore, understanding the spatial and temporal distribution V_p is very important in thin film technology.

The present study has been carried out to understand the discharge dynamics further. This study provided an important understanding of HiPIMS discharges. Though the measurements were carried out along a single line parallel to the discharge centre line as discussed earlier, this provides useful information, however, it does not give the picture of the entire discharge volume. There is still a need for detailed spatial temporal measurements of plasma potential in the HiPIMS discharges. To accomplish this, a detailed time-resolved two dimensional (radial and axial) plasma potential measurements using the emissive probe technique in the 'saturated floating potential mode' were carried out. Essentially, the present study provides the complete picture of the time evolution of the plasma potential in the entire discharge volume.

4.2.1.1 E × B Drifts in Magnetron Discharges

The magnetic field geometry in magnetrons is very complex and the magnetic field strength varies radially as well as axially. A significant component of the magnetic field is parallel to the cathode surface above a large region known as race-track. This parallel magnetic field together with the axial electric field, generated by the sheath and presheath, constitutes strong electron E × B drift velocities above this region and confines the plasma electrons. The plasma ions being massive (for Ar^+ M_i/M_e is 40 × 1845) are not magnetized as their Larmor radii are typical larger than the plasma scale length and hence do not experience to E × B drift.

The E × B drift of the electrons constitute a closed loop current known as Hall current I_H above the racetrack that may be many times larger than the cathode discharge current I_D. The confined electrons above the racetrack region ionize the neutral gas atoms and create a region of intense ionization adjacent to the cathode. The ions born in the electron trap region are accelerated by the plasma sheath to the cathode and impact there with several hundred electron volt energy and liberate secondary electrons. The liberated secondary electrons are accelerated back to magnetic trap region and hence help to sustain the discharge.

The E × B drift plays a very important role in sustaining the discharge in many plasma devices such as co-axial Hall thrusters [98, 99], plasma immersion ion implantation [100] and magnetron discharges and therefore gained a lot of research interest, reflected in various publications [83, 36, 102]. The nature of E × B drift has been realized experimentally by various ways. Bradley et. al. [84] predicted the E × B drift with the

help of measured plasma potential and modeled magnetic field and exists in a broad region extending from above the racetrack down to the position close to the axis, 6 cm from the cathode. With the help of measured density distribution and E × B drift, they found the total Hall current is 5 times larger than the total discharge current. Rossnagel and Kaufman [103] calculated the E × B drift currents from the magnetic field measured by the Hall sensor located above the centre of the drift loop. Drift currents I_H was found to vary almost linearly with the magnetron discharge current. The ratio of the drift current and discharge current I_H/I_D was found to be between 2.5 and 9, it decreases at higher pressure and depends on the gas and the cathode material. They also indicated the existence of anomalously high cross field charge transport responsible for low Hall current ($I_H < 10\ I_D$) [19]. Sheridan et. al. [101] measured electron distribution function by a planar Langmuir probe in a cylindrically symmetric, planar, sputtering magnetron discharge as function of the axial distance from the cathode and estimated the E × B drift velocities at different position in the drift channel (15 to 40 mm above the racetrack). They calculated the drift velocity by the asymmetry in electron velocity distribution functions measured by the probe facing into and away from the electron drift direction. They reported an existence of strong electron drift between 1 and 5 × 10^5 m/s with a maximum occurring closest allowable distance (15 mm) to the cathode surface. Fujita et. al. [104], in an earlier study, calculated the drift current by comparing the electron saturation currents measured by a planar probe facing upstream and downstream of the drift direction, using a simple model of electron collections. The drift speed was found to rise by a factor of two, up to a maximum of 7 × 10^4 m/s, over the axial distance from 2 to 40 mm away from the cathode surface and above the

racetrack. All these above mentioned studies were carried out in DC, pulsed DC and rf magnetrons only and no investigation has been carried out for the E × B drift speeds in the high power impulse magnetron sputtering (HiPIMS) discharges. The present study will provide a simple picture of the E × B drift prevalent in HiPIMS discharges. The E × B drifts have been estimated here by using the derived electric field from the temporal and spatially resolved plasma potential (V_p) measurements and the measured magnetron's magnetic field strength B in the same way as reported in Bradley et. al [84] as follows.

In a typical magnetron device, electrons are magnetized ($r_L < L$), however, ions are non-magnetized due to their higher mass and therefore do not contribute in Hall current. For magnetized electrons, the E × B drift velocity for their guiding centres is [101]

$$v_H = \frac{E \times B}{B^2} \qquad \text{eq. (1)}$$

where E is the electric field and B is the magnetic field strength. These circulating electrons produce a closed loop hall current having current density given as $J_H = e\,n\,E/B$ where n is the electron plasma density. Assuming the electron density is spatially non-varying in the bulk plasma and the full discharge current is due to electrons only ($J_e=J_D$), a simple expression for the Hall current can be found as the function of the discharge current [92]. Equation (1), in component form, can be written for cylindrical geometry as

$$v_H = \frac{E_Z B_r - B_Z E_r}{B^2} \qquad \text{eq. (2)}$$

This equation (2) has been used to calculate the drift speeds with the derived electric fields and the measured magnetic fields strengths.

4.2.2 Experimental Arrangement

Experimental setup for the present study is same as that for the previous one except the region of the diagnosis. A schematic diagram of the magnetron arrangement together with the positions of the emissive probe and the area of measurements are shown in figure 4.19. The plasma potential measurements were carried out in a plane (r, z) in only one side of the discharge central axis that represents the entire discharge volume due to azimuthal symmetry of the discharge. The axial distance ranges between 10 and 80 mm ($10 < z < 80$ mm) from the cathode surface and radial distances between 0 mm (centre of the cathode) and 90 mm ($0 < r < 90$ mm) with spatial resolution of 5 mm. The emissive probe electrical arrangement and measuring circuitry is the same as used earlier.

For estimating E × B drift speeds, the magnetic field strengths and vector directions have been determined from bench measurements of magnetic field taken in the axial (B_z) and radial directions (B_r) using a Hall probe. The electric field has been obtained from the plasma potentials using the central difference formula.

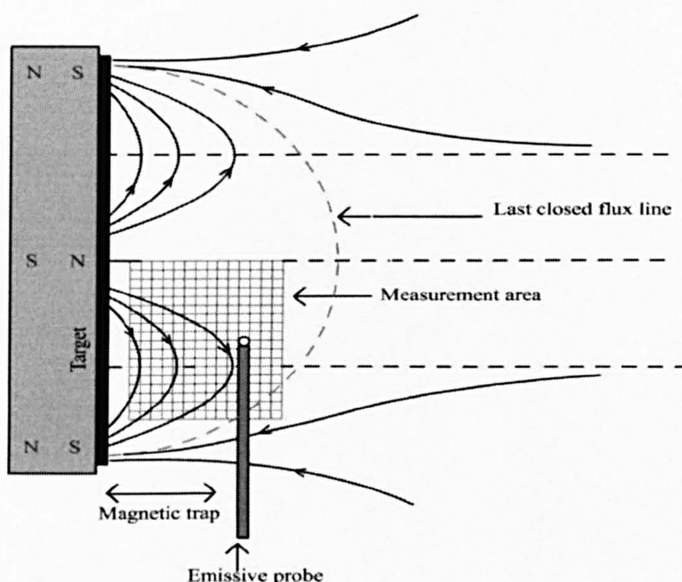

Figure 4.19: *A schematic of magnetron source, B-field lines, emissive probe, and the rectangular grid region where the measurements were carried out. The probe was inserted from the side port of the chamber.*

4.2.3 Results and discussion

The orientation of the probe-plane with respect to the magnetic field is also an important consideration for emissive probe measurements. It was found that when the probe-plane is oriented parallel to the magnetic field, emissive probe gives the correct plasma potential [105].

For measuring the plasma potential by the emissive probe in 'saturated floating potential method', the probe must be in strong emission state. To ensure that the probe is in strong emission condition, a preliminary set of experiments, measuring the floating potential as a function of the heating current in the probe loop, have been carried out at one location (z = 100 mm and r = 45 mm) in the discharge. It was found that at the

heating current I_h of ~2.3 A is sufficient to get strong emission for the entire floating potential waveform (see figure 4.7).

Separate measurements carried out with the emissive probe in this orientation indicate that a heating current of I_h = 2.5 – 3.5 A might be needed to reach full emission in the most dense part of the discharge as shown in figure 4.20.

Measurements in the region of sheath and immediate presheath (close to the cathode, z < 10 mm) could not be carried out due to the geometry of the experimental set-up. Moreover, the presence of the probe very near to the target strongly perturbed the plasma and lowered the discharge current.

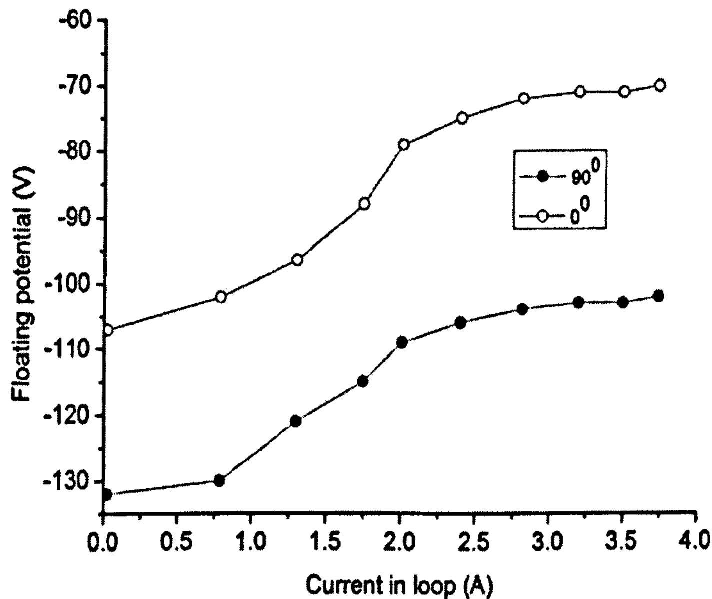

Figure 4.20: A plot of measured emissive probe floating potential (V_f) versus loop heat current (I_h) at one position (z = 30 mm r = 45 mm) during the 'first peak' in two orientation of probe-plane with respect to B-field lines. It should be noted that at I_h > 2.5 A, the floating potential V_f approaches to the plasma potential V_p.

4.2.3.1 Two - dimensional Plasma Potential Evolution

The figure 4.21 shows the time evolution of cathode discharge voltage (V_d) and the plasma potential V_p measured at z = 100 mm, r = 45 mm with the emissive probe. Both of these traces have been taken directly from the oscilloscope. From the plot, it is clear that V_d ramps down -670 V in 200 ns and then relaxes somewhat, to reach -600 V in 20 μs. After this V_d rises to 0 V in 100 μs. The plasma potential V_p waveform has been averaged over 128 samples to reduce the random error in the measurements.

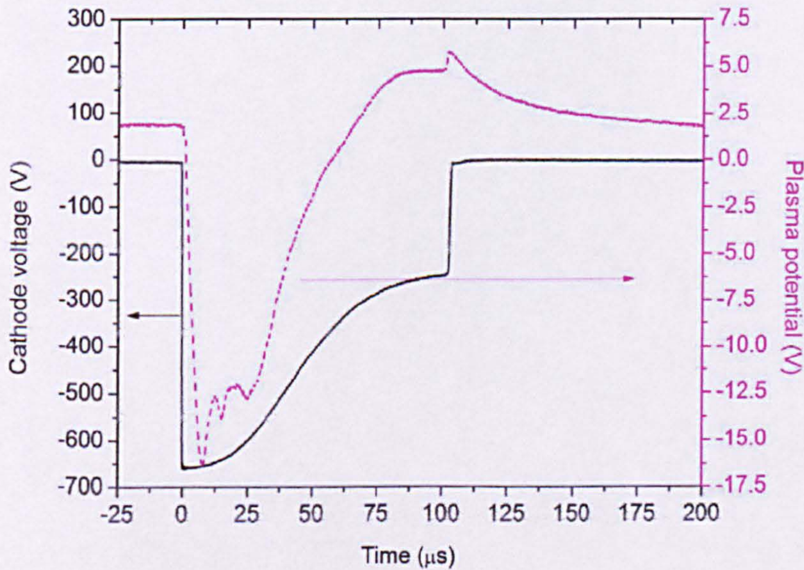

***Figure 4.21**: A plot of the time-evolution of typical plasma potential (V_p) measured at one position (z = 100 mm and r = 45) together with cathode discharge voltage V_d, at an average discharge power of 650 W and a gas pressure of 0.54 Pa in B-field. Here, we identify the "first peak", "second peak" and "I_{Dmax}". At the time of t = 57 μs V_p goes above the ground as shown by vertical line*

From the figure 4.21, it is clear that the plasma potential V_p readily respond to the cathode discharge voltage with some additional double layer potential structure hereby called as '*second peak*'. This '*second peak*' might be a signature of the occurrence of the titanium ions Ti^+ in the discharge as the Ti^+ has been detected first time at the same time in mass spectroscopic measurements in the same operational conditions [106].

The plasma potential V_p is negative for about half of the pulse on-tome (~ 57 μs measured at 100 z = mm) and then it goes above the ground and acquires the value of ~ 4 V. It also shows a kink at t = 100 μs, that is due to the electromagnetic interference caused by the fast change in the discharge voltage V_d at 100 μs. It decreases then and stabilizes at ~ 2 V for rest of the pulse 'off-time'. For the analysis of the plasma potential, we identified three distinct points on the V_p waveform as '*first peak*', '*second peak*' and 'I_{Dmax} - V_p *at maximum discharge current*'. The '*first peak*' was chosen as it is the deepest V_p occurred in the plasma. The '*second peak*' was chosen as it is, we believe, a signature of some physical processes occurring in the discharge and the 'V_p *at maximum discharge current*' as plasma is fully developed at this point of time. From the plot, it is also clear that the V_p follows V_d with an additional potential structure named as '*second peak*' always more positive than the V_d.

The spatial distribution of the plasma potential V_p at '*first peak*' is shown in the figure 4.22. The features present in the plasma potential profile can be seen clearly. The plasma potential V_p is always more positive than the cathode discharge voltage V_d throughout the volume of the bulk plasma having the deepest value (~ -150 V) in a region above the race-track ($10 < z < 15$, $40 < r < 50$ mm). The V_p becomes more

positive farther away the cathode and radially outward. The existence of a region of very high negative plasma potential above the race- track results in a very strong electric field (5 kVm^{-1}) directed towards the cathode and, in turn, back scattered plasma ions towards the cathode contrary to that discussed in conventional pulsed magnetrons [104]. This strong back-scattering of ions could be the root cause of the observed lower deposition rate in HiPIMS discharge as reported in [105].

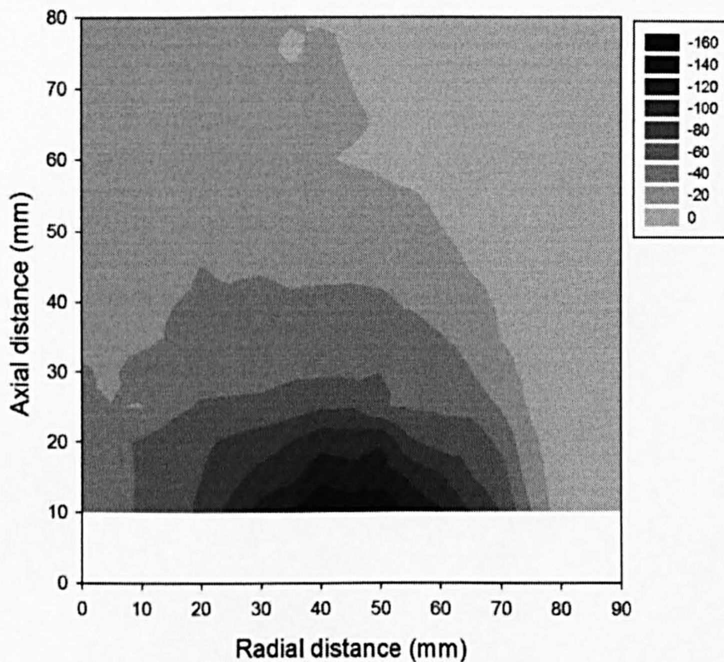

Figure 4.22*: A contour plot of the plasma potential at the times when "first peak" phase occurs.*

The most interesting feature observed here is that the V_p has negative values throughout the bulk plasma during the first peak, however, it becomes positive ($0 < V_p < 4$ V) in the outer region (r > 75 mm) of the discharge and, in turn, creates a lower electric field. Therefore the ions born at higher energies can overcome this potential

barrier (0.4 kV m^{-1}) easily and can diffuse towards the chamber walls. Figures 4.23 and 4.24 show the spatial distribution of the plasma potential at the '*second peak'* and at't = *30 μ*'.

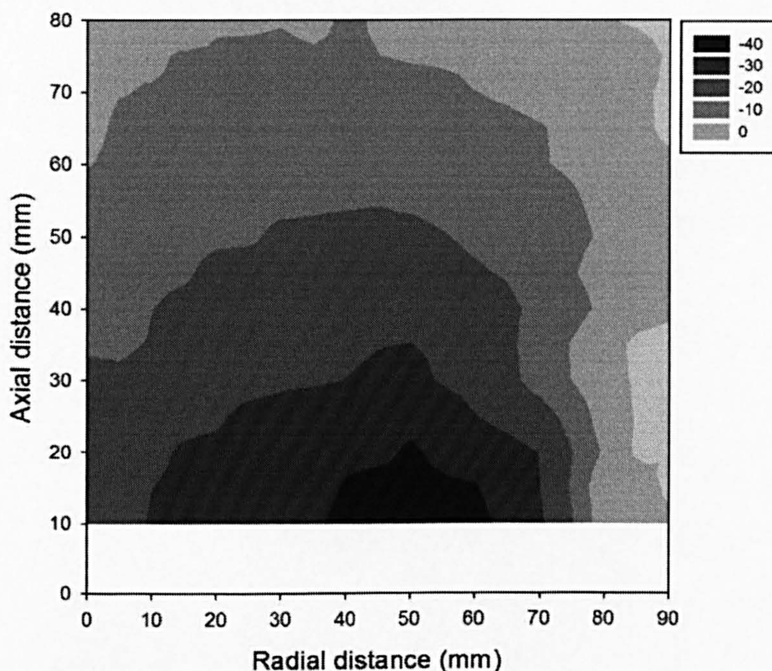

Figure 4.23: *A contour plot of the plasma potential at the times when "second peak" phase occurs.*

It can be seen clearly that V_p distributions in both cases have similar spatial distributions as it in '*first peak*' except that magnitudes of the V_p are lower in both of the cases.

One of the interesting features observed is the large plasma potential V_p variation in the bulk plasma. It is 100 V increase (-150 V → -50 V) from z = 10 to 20 mm during the '*first peak*' and above the racetrack. This change in the V_p decreases as we move

radially from the racetrack, however, it is still larger than that observed in pulsed magnetron [83]. The potential drop of 100 V is obviously much larger than in the classical pre-sheath region ($kT_e/2e$) needed to ions to reach at the ion acoustic speed at the sheath edge in non-magnetized plasma [107].

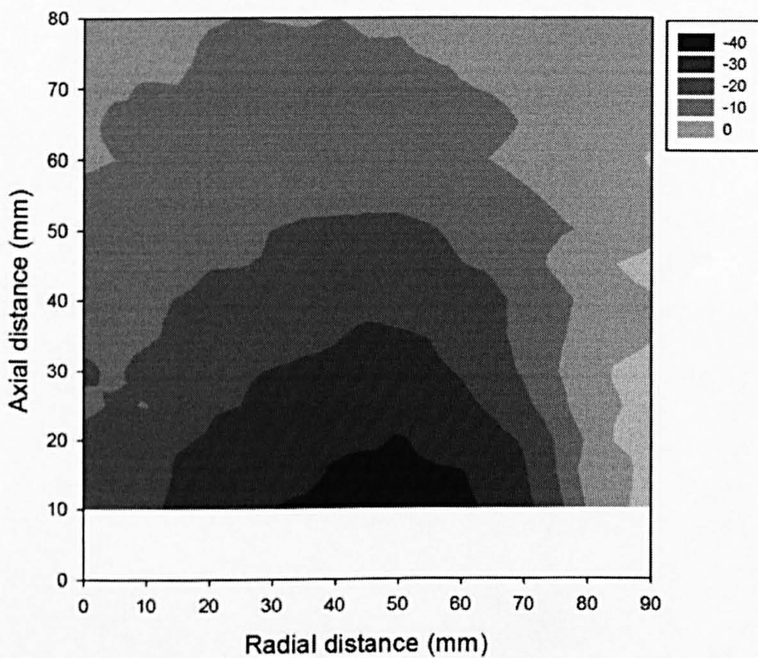

***Figure 4.24**: A contour plot of the plasma potential at the t= 30 μs.*

That is for average electron temperature in HiPIMS of 10 eV, it is ~5 V, very small compared to observed ion acoustic speed in this study. Therefore this region can be interpreted as extended presheath region. The simple classical theory of presheath and one dimensional modeling of magnetron sheath [106] cannot account for the observed large potential variation, however, the modeling study carried out by Sheridan et. al. [101] using PIC-MCC simulation technique and fluid modeling incorporating the

classical diffusion rates have shown the existence of such a large potential variation in the presheath regime.

4.2.3.2 Evolution of Axial and Radial Electric Fields

The electric fields ($E = - dV_p/dx$) have been derived from the discrete measurements of V_p by using the 'central difference method'. Along the axis at r = 0 mm, the boundary condition $E_r = 0$ has been imposed. In the inner region (z = 5 mm), an artificial plasma potential value has been added by extrapolating the measured plasma potentials. These derived data have been smoothed while plotting to make the plot clearer, however, this smoothing process did not lose any prominent features present in the electric field distribution. The spatial distributions of the radial and axial electric fields derived in this way have been shown in the figures 4.25 and 4.26 respectively for the '*first peak*'. The radial electric field E_r, as can be seen in figure 4.25, has clear and distinguishable structures around the racetrack. It is pointing towards the central discharge line between centre and racetrack region (0 < r < 45 mm), however, it is directed radially outward beyond the racetrack region (r > 45 mm). The presence of this strong radial electric field directed outward transports significant number of plasma ions towards the chamber wall and might be responsible to higher deposition rates laterally as reported by Lundin et. al. [81].

Figure 4.26 shows the spatial distribution of the axial electric (E_z) field for the '*first peak*'. From the plot, it is clear that the E_z has a defined structure and directed towards the cathode in the entire bulk plasma except at outer region (r > 80 mm).

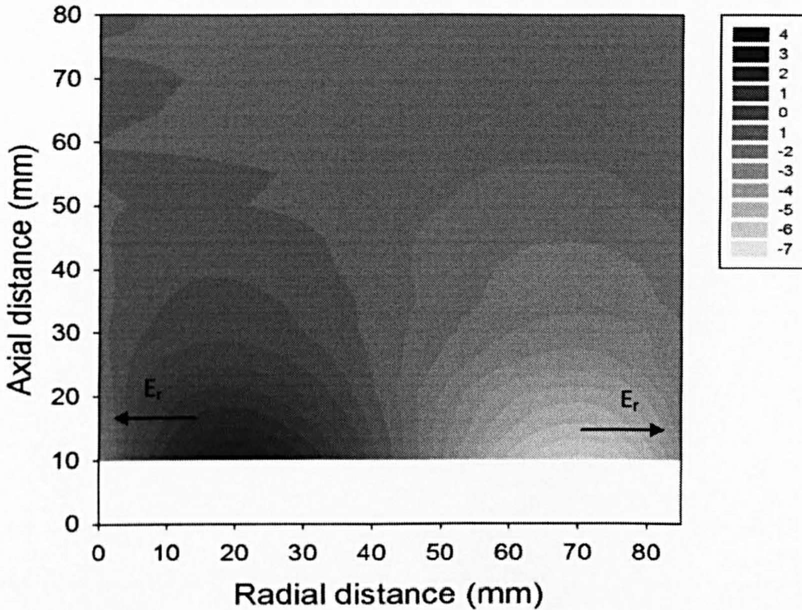

***Figure 4.25**: The plot of the derived radial electric field at times when "first peak" phase occurs. The unit of electric field is in kVm^{-1}.*

The presence of very strong axial electric field E_z directed to the cathode in the region close to the cathode ($10 < z < 20$ mm and $35 < r < 45$ mm) can be seen clearly. This E_z plays very important role in plasma dynamics in two ways. Firstly, it repels the plasma ions towards the substrate and therefore reducing the deposition rates. Secondly, it produces strong close looped electron Hall current and might be an important factor to deflect the ions sideways as reported in [81]. The presence of the appreciable electric field far out into the discharge volume, where the ions are created, implies that the ion energy distribution functions (IEDFs) bombarding onto the substrate should be broad. The radial and axial electric field distributions in '*second peak*' and at'*t = 30 μs*' phases have similar profiles as it has in '*first peak*' phase except in the magnitudes. Therefore, it is not shown here.

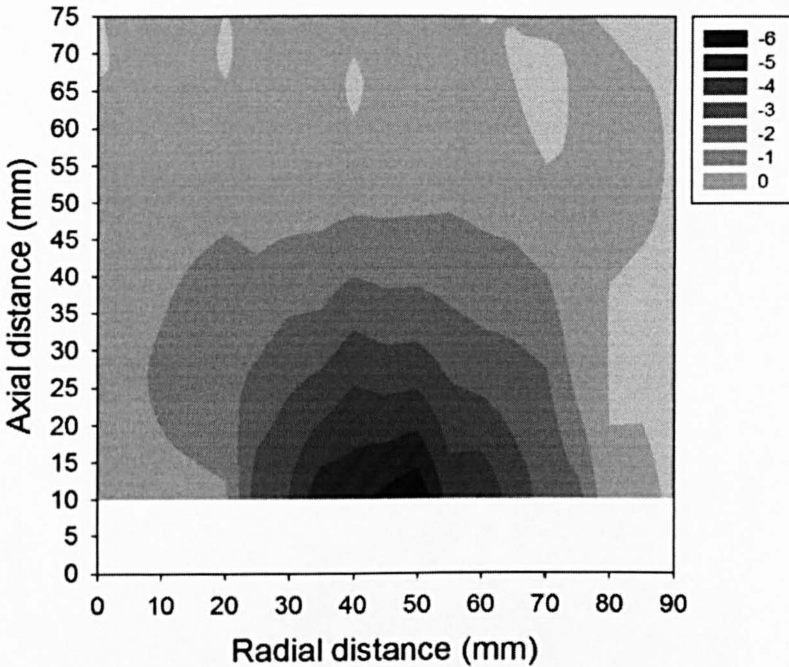

Figure 4.26: *The plot of the derived axial electric field at times when the "first peak" phase occurs. The unit of electric field is in kVm^{-1}.*

As the pulse goes on the magnitudes of these field become less. The examination of these spatial distributions of the electric field reveals the existence of very large axial electric fields inside the magnetic trap region (z < 45 mm at above the racetrack) that opposes the ion transport to the substrate. To reach the substrate, positive ions would need energy of 200 eV in the '*first peak*' (t ~ 3μs) region. In the '*second peak*' (t ~ 8-12 μs), they still need the energy of 45 eV to surmount the potential hill in front of the target. It can be inferred that ions created inside the magnetic trap have very less probability to reach up to the substrate. However, ions created outside the magnetic trap can easily reach the substrate as there is very small variation in V_p (~ 3 eV) elsewhere.

Therefore, Ti neutrals with very few eV of energy that get ionized outside the magnetic trap are the main constituents to be deposited on the substrate in HiPIMS discharges.

4.2.3.3 E × B Drifts Velocities

The distribution E × B drift velocities were calculated from the derived electric fields and measured magnetic field using equation (1) and are shown in figure 4.27 for the *'first peak'* condition.

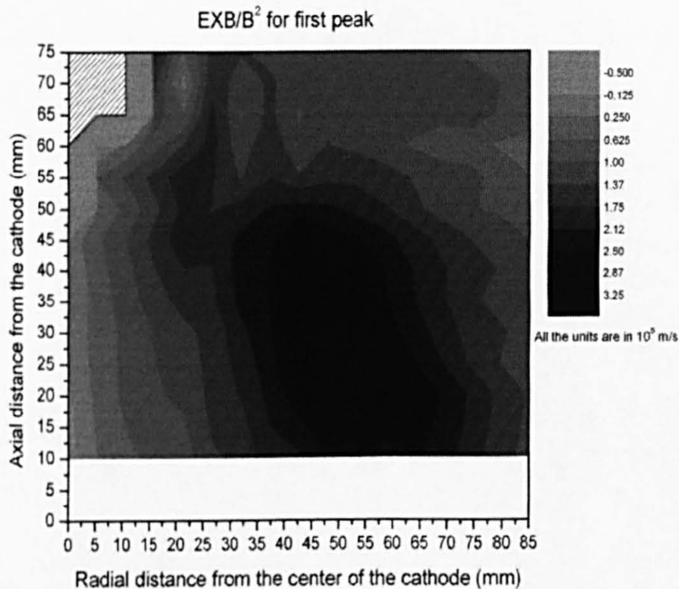

Figure 4.27: *The plots of the E × B Drift speeds in 'first peak' condition*

As it can be seen in the figure 4.27, there are some clear features in the spatial distributions of the E × B drift speeds. There is a diagonal region of high drift speeds extending from above the racetrack to near the discharge central axis at z = 50 to 65 mm. The maximum value of the drift speed found was 3.25×10^5 m/s in the region

extending radially 40 < r < 60 radially and 10 < z < 40 axially in the 'first peak' condition. The checked area shown at the top left hand corner of the contour plot (see figure 4.27), is the region where electron Larmor radii are greater than the distance from the discharge central line. Here $|B|$ field strength is very small and electric field strength E is finite. Therefore, the drift speed E/B will be very high in this region; however, the electrons are not magnetized here and therefore do not contribute to the Hall current densities. The distributions of E × B drift speeds have the similar profile in all the three cases; however, the spread and location of region of maximum drift speeds changes. The drift speeds always reduces as we move farther away from the racetrack region in the radial direction.

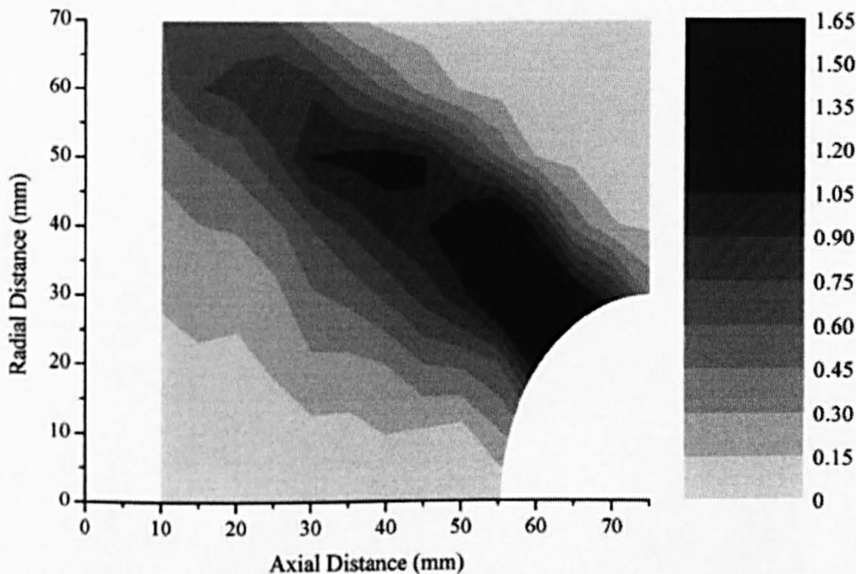

***Figure 4.28**. The distribution of E × B drifts velocities in for a pressure of 0.26 Pa and a cathode voltage of -330 V. The unit is 10^5 ms^{-1}(taken from [83])*

Figure 4.28 shows a plot of E × B drift velocities in DC magnetron discharges as reported in [83]. A comparison of the figures 4.27 and 4.28 readily illustrates that the distribution of E × B drift velocities in HiPIMS discharges is similar to that found in the DC magnetron discharges except the magnitudes. The magnitudes of E × B drift velocities in HiPIMS discharges are larger than in DC magnetron discharges. It is due the fact of existence of larger electric fields in the HiPIMS discharges.

4.2.4 Conclusions

The spatial-temporal evolution of the plasma potential V_p and the E × B drift speeds in the HiPIMS discharge have been studied using emissive probe in '*saturated floating potential*' method. The observed time lag between the V_d and I_d is due to the statistical and formative time required to develop the discharge. From the plasma potential V_p profile, it is clear that the V_p readily respond to the cathode discharge voltage V_d with an additional double layer like potential structure named as '*second peak*' structures during the pulse on-time. The emergence of this 'second peak' might be a signature of the evolution of the titanium ions Ti^+ in the discharge as occurrence of Ti^+ has been observed at the same time during the pulse in mass spectroscopic measurements in the same conditions.

The spatial map of the plasma potential distributions shows a large potential variation (~125 V) in a very small region (10 <z < 40 mm) above the racetrack during the 'first peak', this can be attributed as the extended presheath region close to the cathode which causes much greater ion acoustic speeds compared to the classical Bohm speeds at the sheath edge determined by $(kT_e/M_i)^{1/2}$. This large variation in the V_p produces the large

axial electric field pointing towards the cathode. This electric field hampers the transport of the plasma ions to the substrate and one of the main causes of observed lower deposition rate in HiPIMS discharges.

The spatial distribution of V_p has a similar form as it is in the pulsed magnetron discharges except the comparatively large magnitudes of V_p. It has the laminar shape above the racetrack and remains similar in all the three investigated conditions ('first peak', 'second peak' and 'I_{Dmax}'), however, the magnitude of the plasma potential and its variations reduces respectively.

The radial and axial electric fields derived from the plasma potential V_p measurements by using the 'central difference formula' show the existence of a strong axial electric field directed towards the magnetron close to the cathode. It acts like a potential barrier for the plasma ions travelling to the substrate and therefore back scatters the ions. This axial electric field together with the magnetic field creates large electron E × B drift speeds that, probably, deflect the ions towards the chamber wall. The existence of radial electric field pointing to the chamber walls also plays an important role in the discharge dynamics and transports the plasma ions towards the wall.

The E × B drift speeds have been calculated using the derived electric field and the measured magnetic field strengths. A broad channel of the very high drift speeds ($\sim 3.5\times10^5$ m/s), extending from z = 10 to 50 mm and r = 35 to 65 mm, was found and it was situated above the race track pointing towards the central discharge axis and diagonal in shape. This channel of maximum drift speeds shrinks and moves with time during the pulse.

Chapter 5

POWER DENSITY MEASUREMENTS ONTO SUBSTRATE

This chapter describes the temporal evolution of substrate temperature in the HiPIMS, DC and pulsed-DC magnetron sputtering discharges and it has been used to calculate the power density onto the substrate. The measurements have also been carried out to investigate the effect of pulsing frequency and magnetic field strength on the power densities in the HiPIMS discharges. A comparative study of power densities in HiPIMS, DC and pulsed DC magnetron sputtering has also been carried out at the same average power levels.

5.1 Introduction.

Plasma wall interactions are a very important phenomenon in a variety of applications such as tokamak edge plasma, plasma processing i.e. deposition of thin films, surface modifications and etching and can significantly influence the quality of the thin film deposition. When a substrate is exposed to the plasma, the plasma particles transfer momentum and deposit energy that results substrate temperature to increase. For thin film deposition, the substrate temperature is a very crucial parameter as it controls the atomic processes involved such as adsorption, sputtering, implantation, diffusion and chemical reactions. It has been found that the film properties are highly dependent on the depositional temperature [109] and some particular effects observed in thin films deposited by magnetron sputtering have been

reported to be temperature dependent [110-111], therefore it becomes necessary to understand its sources and how the process parameters influence it so that the discharge could be optimized to produce engineering quality thin films with tailored properties for particular applications.

Reactive sputtering is the sputtering of elemental targets (target consisting of single element) in the presence of chemically reactive gases that react with both the ejected target material and the target surface. It is a very popular technique and widely used for the search of new material properties, for the deposition of a very wide range of compound and alloy thin films, including oxides, nitrides, carbides, fluorides or arsenides [113]. Besides the improved properties of non-reactively sputtered films, the popularity of pulsed DC reactive sputtering from elemental targets can be attributed to several factors such as (1) it is capable of producing thin compound films of controllable stoichiometry [115] and composition [115] at high deposition rates and on industrial scale [116-118] (2) elemental targets are more pure and therefore, films of high purity can be produced [119] etc.

Although, reactive sputtering is conceptually simple, it is in fact a complex and non-linear process which involves many interdependent parameters [119]. The presence of the reactive gas at both the cathode surface and the substrate results in strong interactions of the reactive gas not only with the condensing material but also with the cathode surface, the so-called target poisoning. Reactions in the gas phase are ruled out for the same reasons that ions cannot be neutralised in the gas phase there is no

mechanism which can dissipate the heat of neutralisation to conserve both momentum and energy in a two-body system, therefore it can only happen at a surface. These cathode reactions are seen to increase suddenly at some rate of reactive gas flow. If flow control of reactive gas is used, such reactions are marked by a change in the impedance of the operating plasma, an abrupt increase in the system pressure or more precisely, in the reactive gas pressure, a drastic drop in the deposition rate and a change in the film from metal-rich to gas-rich.

It has been observed that there are three main limitations of reactive sputtering: (1) hysteresis effect (2) jump transition from metallic to reactive mode of sputtering, which excludes the production of the compound films in a certain interval of stoichiometry and (3) arcing. In the recent years, some of these limitations have been overcome [120 - 124].

5.1.1 Hysteresis Effect

Hysteresis effect is a problem in reactive sputtering that causes the adverse effect on producing the non-stoichiometric compound films. This effect originates from two competitive processes (1) sputtering of the cathode surface and (2) the covering of the cathode surface by the reaction products. Figure 5.1 illustrates the dependence of partial pressure as a function of flow rate of reactive gas. The hysteresis occurs in the presence of discharge only. At low values of reactive gas flow rate (see interval AB), all the reactive gas is gettered by the sputtered metal. At point B, the flow rate of reactive gas into the chamber is equal to the gettering rate of sputtered metal. Every small increase in the flow rate results in a sudden increase of partial

pressure in the deposition chamber and a decrease in film deposition rate. A further increase of flow rate (interval CD) results in a linear increase of partial pressure.

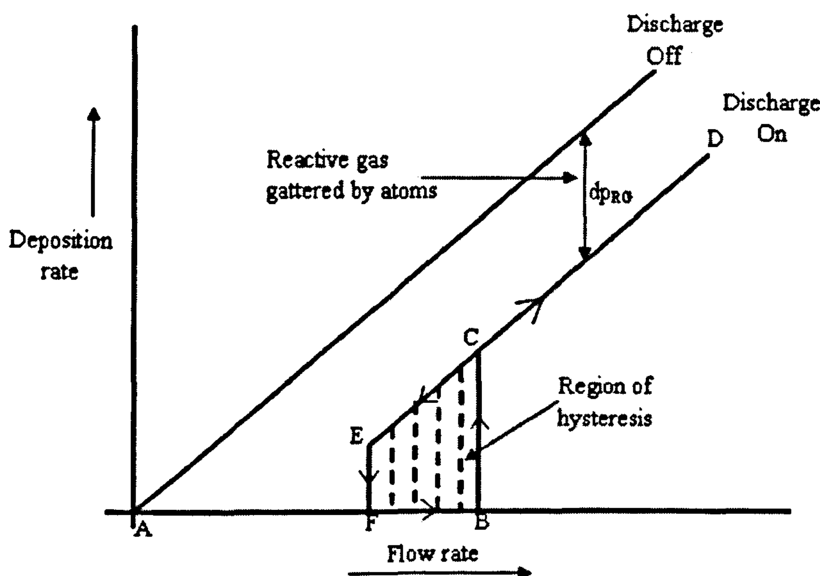

Figure 5.1: Schematic illustration of partial pressure as a function of reactive gas flow rate

The decrease of flow rate from D to E is accompanied by decrease of partial pressure but a return to the metallic mode (interval EC) is delayed. This is because partial pressure remains high until a compound layer on the surface of the sputtered target is fully removed and metal is again exposed to be sputtered. As a result, the consumption of reactive gas increases and partial pressure decreases to the background level. A closed hysteresis loop is formed in this way.

For these experiments, a titanium target (99.995% pure) was sputtered in a reactive environment with argon flow rate of 30 sccm and oxygen flow rate of 1.3 sccm. The

Power density measurements were concentrated on effect of spatial variation (radial and axial) and average power variation on the total power deposited on to the substrate [125-127]. The magnetic effect on the power density has been completely un-explored. The magnetron's magnetic field strength is an important parameter that determines the charge particle transport in the discharge that, in turn, determines the thin film properties.

5.2 Experimental Arrangement

This study has been carried out in two different experimental set-ups in Manchester Metropolitan University (MMU) and Liverpool University (LU) in United Kingdom.

5.2.1 Experimental Set-up at Manchester Metropolitan University

First experimental set-up situated in MMU was a Teer Coatings UDP 450 magnetron sputtering rig fitted with a single unbalanced magnetron with a titanium target (99.5% purity, 300 x 100mm). The target was sputtered in argon at 0.2 Pa for all the measurements, and power was delivered in continuous and pulsed-DC modes via an Advanced Energy Pinnacle plus supply, and in HIPIMS mode via a Huettinger HMP1/1_P2 supply. Target current and voltage waveforms, and hence power levels, were monitored directly via a digital oscilloscope. Deposition rates were measured at a distance of 150 mm from the target surface via a Maxtek crystal monitor, and substrate temperature measured in a similar position over time via a thermal probe, described below. A shutter was placed such that the probes could be isolated from the plasma between readings. Figure 5.2 shows the schematic of the experimental set-up used.

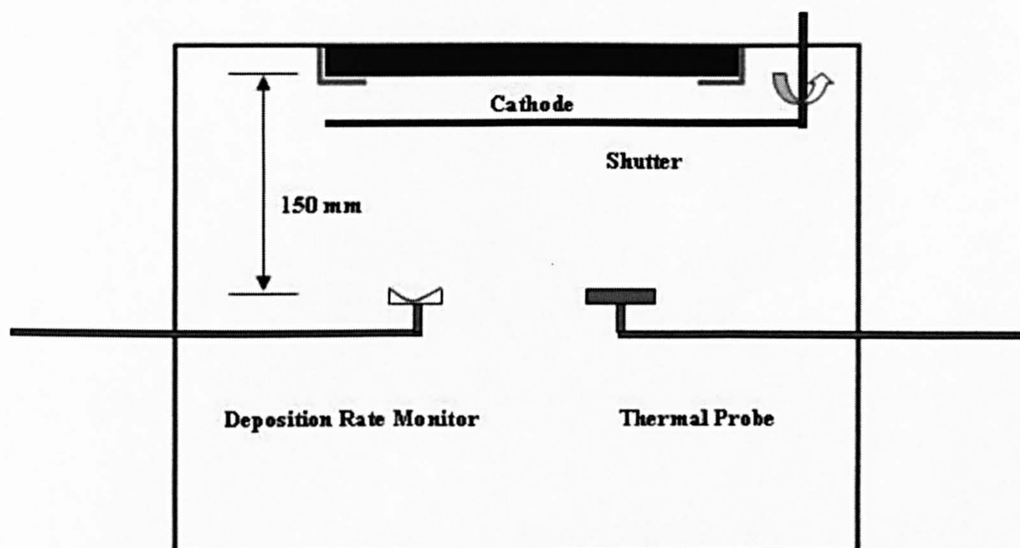

***Figure 5.2**: The schematic representation of the experimental set-up used to measure the power density and the deposition rates.*

Magnetron glow discharges were generated in continuous DC, and at 350 kHz asymmetric bipolar pulsed-DC (50% duty), at three time-averaged discharge power levels (500, 750 and 1000 W). HiPIMS glow discharges were generated at the same three time-averaged power levels (500, 750 and 1000 W) and at five pulse frequencies (100, 250, 500, 750 and 1000 Hz) at each of these power levels. The pulse width was 100 μs in each case. The deposition rate, heating and cooling rates were measured for each discharge, and used to determine the thermal energy flux to the substrate for a normalized deposition rate.

5.2.2 Experimental Set-up at Liverpool University

The experimental set-up used for this study is same as explained in Chapter 2. The thermal probe was placed 100 mm away from the cathode surface, in parallel to the

discharge center, and above the race-track (z = 100 and r = 45 mm) and mounted onto a metallic barrel and therefore could be moved axially. A shutter of stainless steel was also mounted in front of the probe to isolate it from the plasma during the non-operational mode.

5.3 Results and Discussion

The experiments have been carried in two modes of operation namely as metallic and reactive mode. In metallic mode, titanium target has been sputtered in argon gas environment and in reactive mode the same titanium target has been sputtered in oxide mode.

5.3.1 Metallic Mode

The following experiments have carried out in metallic mode.

5.3.1.1 Power Density onto the Floating Substrate

The temperature of a substrate rises when it is exposed to the plasma. The power density onto the substrate i.e. product of incident particle energy and particle flux, is not only the cause of substrate heating but also determines surface etching and sputtering rates that in turn determines the thin film properties. Therefore, the power density is a key parameter in processing plasmas that determine the surface processes. The typical substrate's temperature evolution in heating phase (exposed to plasma) and in cooling phase in DC mode is shown in the figure 5.3. The substrate is exposed to the

plasma for about 180 sec and then the plasma is switched off. The average power fed to the plasma is 1000 W.

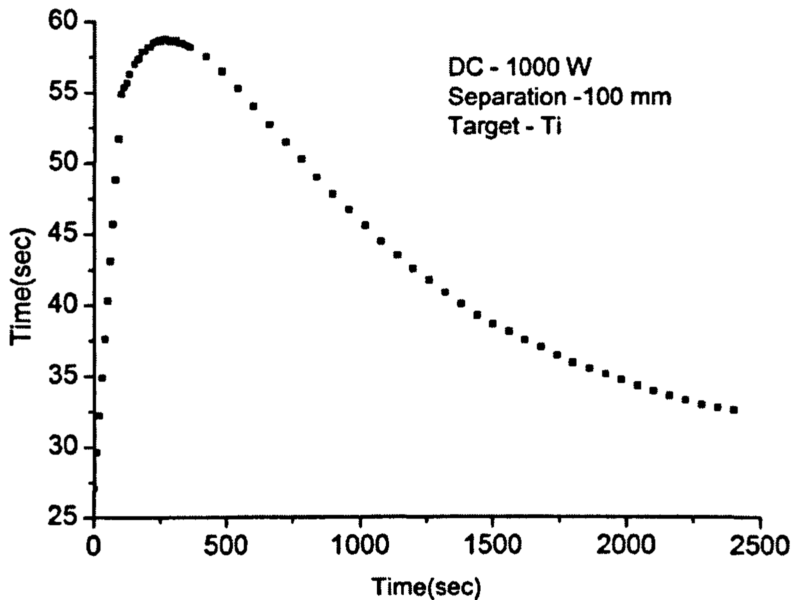

Figure 5.3: Plot showing the temporal evolution of probe temperature in heating and cooling phase. The probe was located at 100 mm away from the cathode surface and above the racetrack (z = 100 and r = 45 mm). The average power fed to the plasma was 1000 W. The average pressure was kept constant at 0.54 Pa.

Figure 5.3 indicates that the temperature rise is very fast when the probe is exposed to the plasma and it cools down slowly when the plasma is switched off. The power density onto the isolated substrate has been calculated from the above plot and has been shown in the figure 5.4. The calculated power density in DC mode at an average power of 250 W was found to be 22.77 mW/cm^2 rising upto 129.72 mW/cm^2 for an average power of 1000 W and it is in agreement with the measurements carried out on to the same device previously [128].

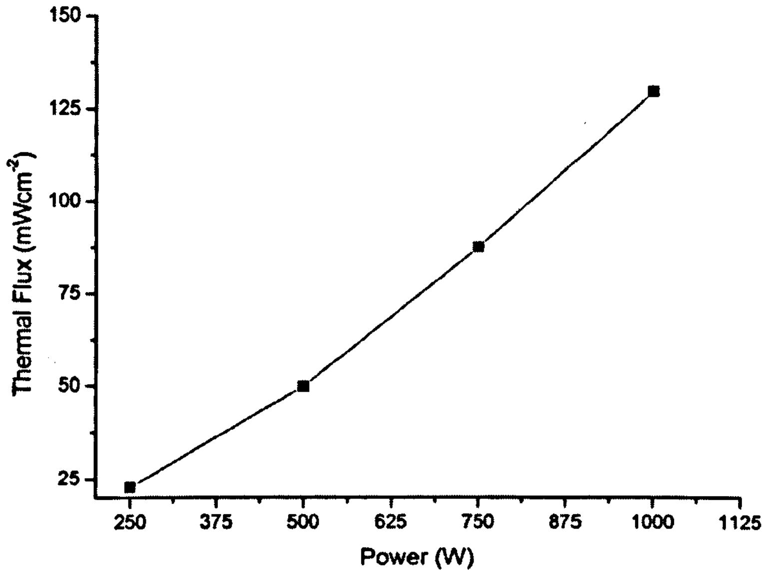

Figure 5.4: *A plot of the thermal Flux versus average power onto the isolated substrate in DC mode. The discharge was operated at 0.27 Pa and the measurements were carried out at 100 mm away from the cathode surface and above the racetrack.*

It is clear from the plot that the average power density onto the substrate is a linear function of the average power fed to the plasma. The increasing trends in power density with the average can be attributed to the increased sputtering with higher powers. Figure 5.5 shows the power density variation with average power in the HiPIMS mode. The plot clearly illustrates that the power density is linearly dependent on the average power fed to the discharge. Figure 5.6 shows the power density against the pulsing frequency in pulsed DC magnetron sputtering. These measurements have been carried out at 100 mm away from the cathode surface and just above the racetrack. The plot depicts that an increment in the pulsing frequency enhances the power density onto the substrate. It is not surprising that as the frequency is increased, the substrate gets less time to release heat from its surface between two consecutive pulses.

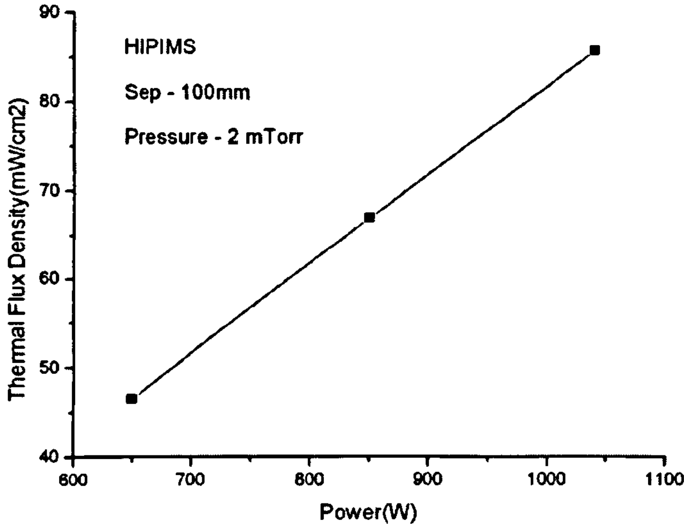

Figure 5.5: A plot of the thermal flux versus average power onto the isolated substrate in HiPIMS mode. The discharge was operated at 0.27 Pa and the measurements were carried out at 100 mm away from the cathode surface and above the racetrack

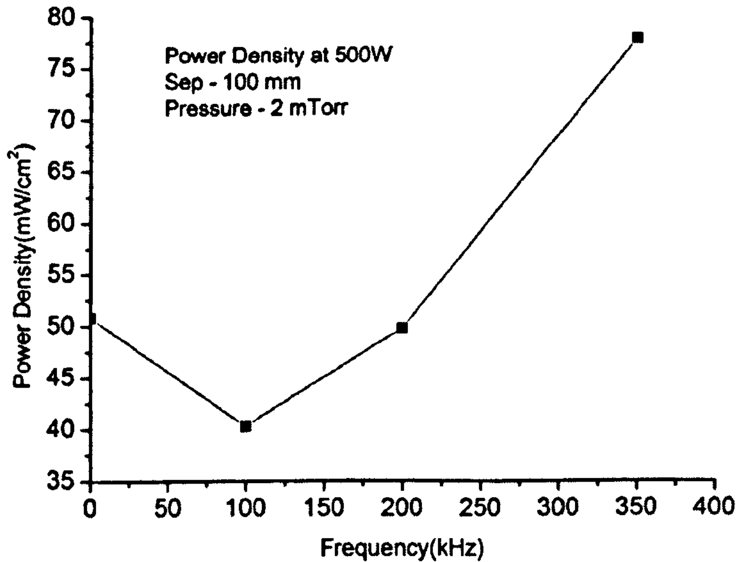

Figure 5.6: A plot of the power density versus average pulse frequency onto the isolated substrate in HiPIMS mode. The discharge was operated at 0.27 Pa and the measurements were carried out at 100 mm away from the cathode surface and above the racetrack

5.3.1.2 Axial variation of the Power Density onto the Substrate

A series of experiments were carried out to study the axial variation of power density onto the isolated substrate in DC, pulsed DC of 100 and 350 kHz and HiPIMS modes of operations. All these measurements were carried out at an average power of 680 W and at an average pressure of 0.27 Pa. The separation between the probe and the cathode surface has been varied from the 80 mm. For the pulsed DC mode of operations of 100 and 350 kHz frequencies, the duty factor was 50% and for HiPIMS mode of operation, the discharge was pulsed at 100 Hz with 100 μs pulse 'on-time'.

A comparison of total power density, during HiPIMS, DCMS and pulsed DCMS at the same average power for different axial locations has been shown in the figure 5.7.

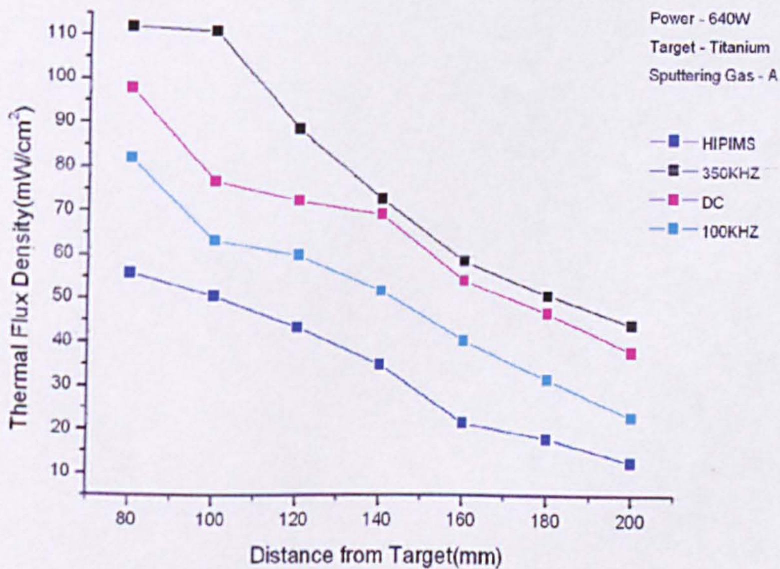

Figure 5.7: A plot of axial profile of power density onto the isolated substrate in HiPIMS, DCMS and pulsed DCMS discharges.

In all of these measurements, the thermal probe was situated just above the racetrack (r = 45 mm) and facing the cathode surface. The power density observed in HiPIMS mode is considerable less than those measured in DCMS and pulsed DCMS.

The axial measurements were carried out in the region between 80 and 200 mm away from the cathode surface as typical substrate position in depositional plasma are between 80 to 120 mm. The plot reveals that the total power density decreases by ~ 35% in pulsed DC discharges and ~ 28% in HiPIMS mode as we move from 80 mm to 140 mm away from the cathode surface.

From figure 5.7, it is also clear that the power density in HiPIMS discharges is significantly less than the DC and pulsed DC modes of operations. The fraction of power density in HiPIMS to power density in DC magnetron sputtering has been estimated as 35% – 60% depending upon the axial positions of the probe. Similar measurements carried out [12] reported similar trends, however the values of this fraction was different (32 - 48%). This difference between the numerical values can be attributed to the different experimental geometry and different average power used. The significantly less power in HiPIMS mode than those in DCMS and pulsed DCMS is due to the reduced particle flux reaching to the substrate in the HiPIMS mode. The lower power density in HiPIMS mode together with deposition rate is a very important parameter that determines the suitability of this technique in deposition onto thermally sensitive substrates such polymeric webs. The total power also decreases significantly with axial variation (~ 50% for DC and pulsed DC and ~ 15% for HiPIMS mode) between the axial locations of 80 mm and 200 mm away from the cathode.

The fraction of the average power fed to the plasma used to heat the substrate is a crucial parameter that is worth considering the deposition is taking place onto the thermally sensitive substrates such as polymer substrate (kapton). As the cathode of diameter of 150 mm has been used in the present study and the average power used was 640 W, the power density on the cathode surface was 3.63 Wcm^{-2}. The total power density at a typical substrate location (z = 100 mm) was 51 and 79 $mWcm^{-2}$ in the HiPIMS and DCMS modes of operations respectively. The fraction of applied power to the cathode that was deposited onto the substrate was 1.4% and 2.2% in HiPIMS and DCMS respectively. Similar results but higher in value have been reported in [126]. This observed difference in this parameter can be attributed to the different experimental set-up and different average pressure used. The current study has been carried out at an average pressure of 0.27 Pa and 0.53 Pa.

5.3.1.3 Deposition rate and substrate heating in HiPIMS, DC and pulsed-DC Magnetron Sputtering

This section describes the power density and deposition rate measurements at a typical substrate position at the same averaged power levels in the HiPIMS, DCMS and pulsed DCMS modes of operations. Then, these measurements were compared to know different mechanisms responsible for these observations.

Figure 5.8 shows the deposition rate measurements in the HiPIMS mode of operation. The deposition rate increases with the average power fed to the discharge and the pulse

frequencies. It should be noted here that the pulse 'on-time' was kept constant at 100 μs in each case therefore the duty factor increased with the pulse frequency.

The deposition rate for DC and pulsed-DC magnetron sputtering are shown in table 5.1. It can be observed from the table that deposition rate is significantly higher in DC case than those in pulsed DC magnetron sputtering.

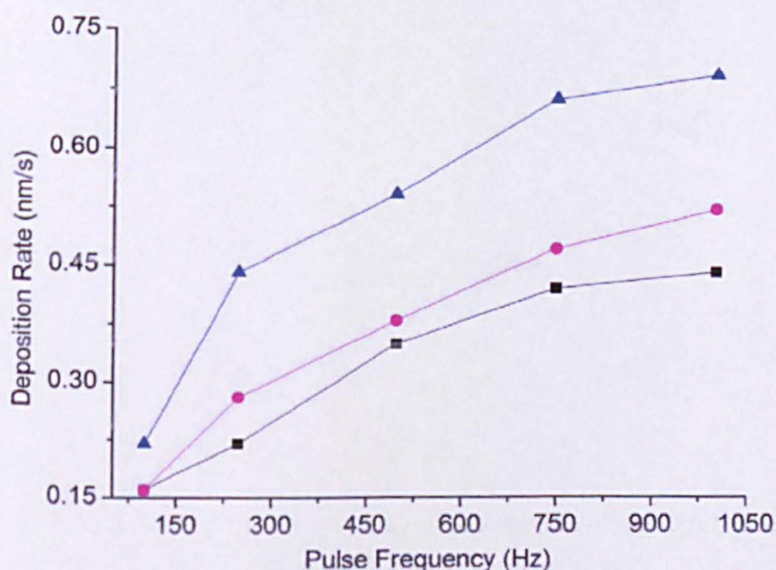

Figure 5.8: A plot of the measured deposition rates in HiPIMS discharge. In all these measurements process parameters were kept constant.

Table 5.1: A table showing the deposition rates in DCMS and pulsed- DCMS.

	Deposition Rate (nm min^{-1})	
Power (W)	**Continuous DC**	**Pulsed at 350 kHz**
500	0.53	0.19
750	1.08	0.31
1000	1.47	0.41

The values for the power density were normalized by the deposition rate in each case to determine power density per nanometer per minute of deposition. This provides a more meaningful measure of heat load that may be applied to a given process.

These values are given in Figure 5.9, which shows distinct groups of values—those for HiPIMS discharges having very low values compared with pulsed dc, and lower normalized thermal energy flux than for DC sputtering. The observed higher normalized power density in pulsed mode can be attributed to overshoot in plasma potential when it transits from 'on' to 'off' [89].

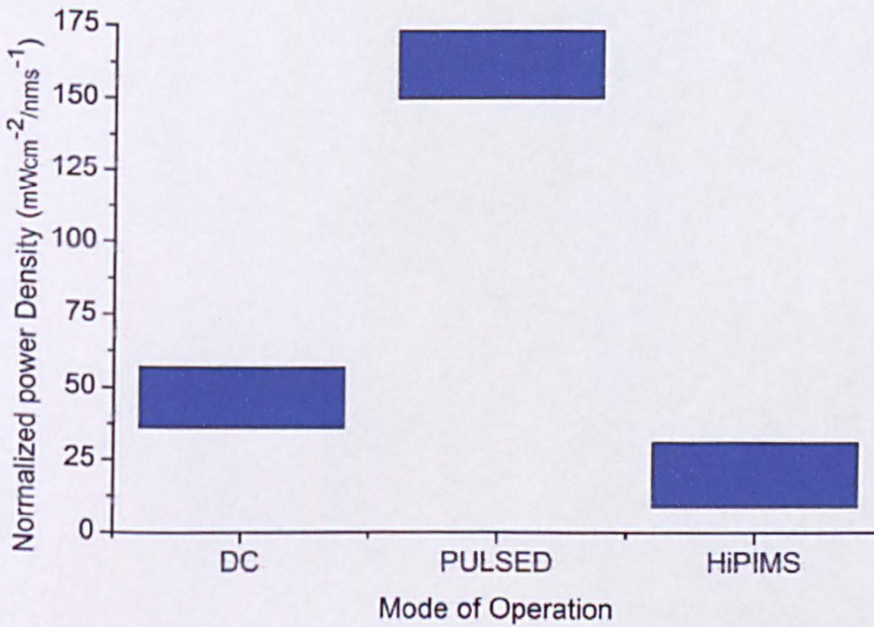

Figure 5.9: Normalized power density for equivalent deposition rates in dc HIPIMS and pulsed-DC modes

5.3.2 Reactive Mode

The following section describes the experiments carried out in reactive mode. In this mode of operation titanium target has been sputtered in argon and oxygen gas environment. The flow rates of argon and oxygen were 30 and 1.3 sccm respectively.

5.3.2.1 Magnetic Field Effect on the Power Density in HiPIMS Discharges

To study the magnetic field effect on the power density onto the substrate, a titanium target is sputtered reactively in the HiPIMS mode.

Before carrying out these experiments, a set of preliminary experiments were carried out to identify the oxygen flow rate that is appropriate for transition mode of the operation. The effect of reactive gas (oxygen) flow rate on the cathode voltage and current waveforms is shown in figures 5.10 and 5.11.

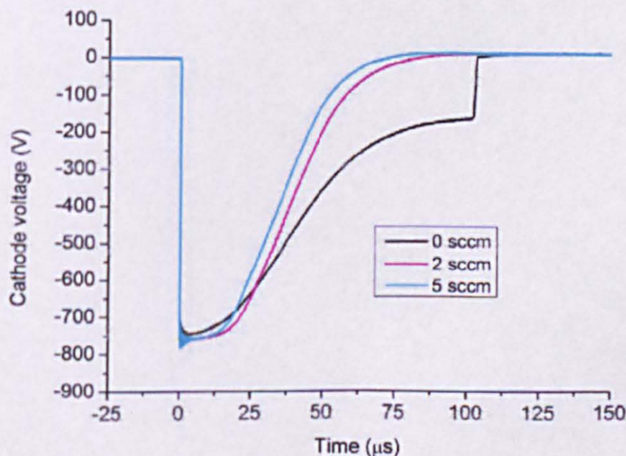

Figure 5.10: A plot of the cathode voltage waveforms at different flow rates of oxygen in reactive mode.

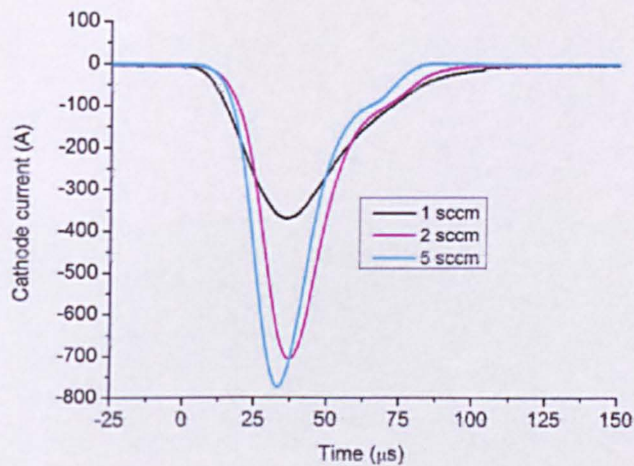

Figure 5.11: A plot of the cathode current waveforms at different flow rates of oxygen in reactive mode.

From the figures 5.11 and 5.12, it can be clearly seen that the oxygen flow rate for the transition is between 1 and 2 sccm. Another experiment carried out with a very small step of flow rate (0.1 sccm) revealed that 1.3 sccm flows rate of oxygen gives the transition mode. Therefore, all the experiments were carried out at oxygen flow rate of 1.3 sccm. However, there was a little change in flow rates with different magnetic field strengths.

To study the magnetic field effect on the total power density onto the substrate, four different magnetic field configurations have been chosen. These magnetic field configurations were obtained by pulling the magnets back relative to the cathode surface. The spatial map of the magnetic field in magnetic field configuration1 is shown in the figure 5.12. Magnetic field measurements were carried out on the bench

while magnetron was removed using a Hall probe with spatial resolution of 5 mm in the radial and axial directions.

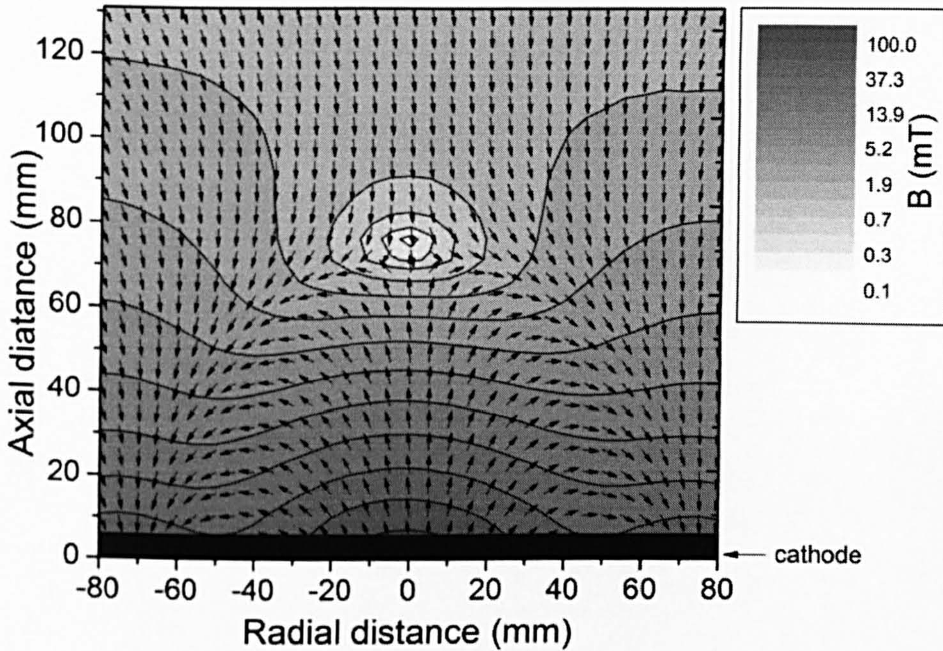

Figure 5.12. The measured magnetic field (flux density B) and field line directions for (a) magnetic field configuration 1 (magnets were situated at 0 mm behind the cathode), Normalized arrows indicate the B-field direction, gray scale is the magnitude of magnetic field B

As the magnetron's magnets are pulled back, the magnetic field strength infront of the cathode surface reduces, however the magnetic field geometry remains same.

The total magnetic field strength ($|B| = \sqrt{(B_z^2 + B_r^2)}$) just above the racetrack and in all the four magnetic field configurations behind has been shown in the figure 5.13. The plot indicates that moving the magnets relative to the cathode surface by 15 mm

reduces the magnetic field strength by 50% at the cathode surface and above the racetrack.

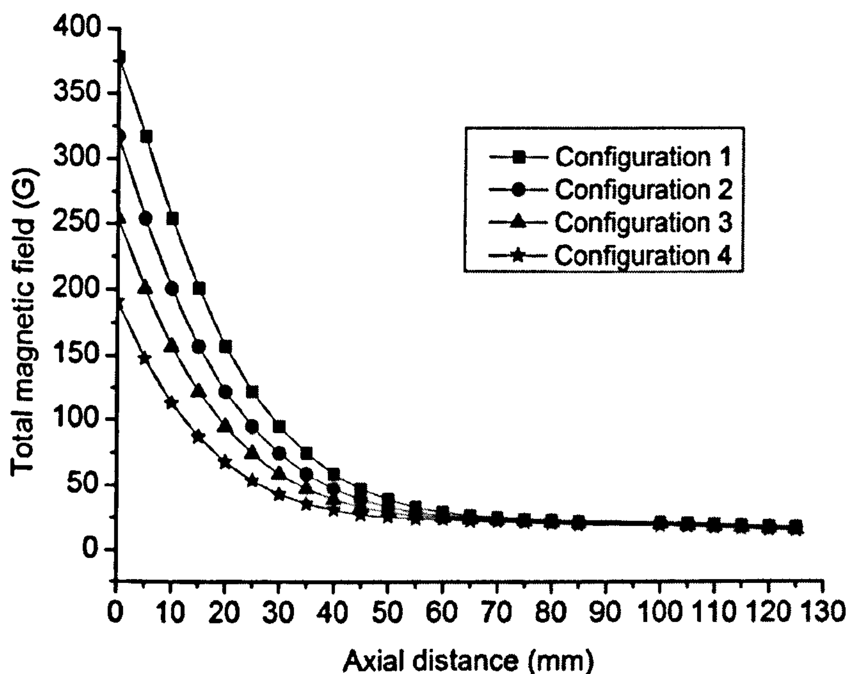

Figure 5.13: The total B-field has been caluclated as $|B| = \sqrt{(B_z^2 + B_r^2)}$ *for all the four locations of magnets. All these measurements were just above the race track (r=45 mm)*

A change in the magnetic field strength influences the temporal evolution of the cathode voltage and current waveforms. Typical plots of cathode voltage and current recorded at the four magnetic field strengths in HiPIMS mode pulsed at 100 Hz with pulse 'on-time' of 100 ms are shown in figure 5.14.

The plot indicates that the peak cathode voltage increases and peak current decreases as the magnetic field strength is reduced. This is not surprising as there is less ionization

efficiency as the magnetic field is reduced and therefore less discharge current and higher discharge voltage for the same average power.

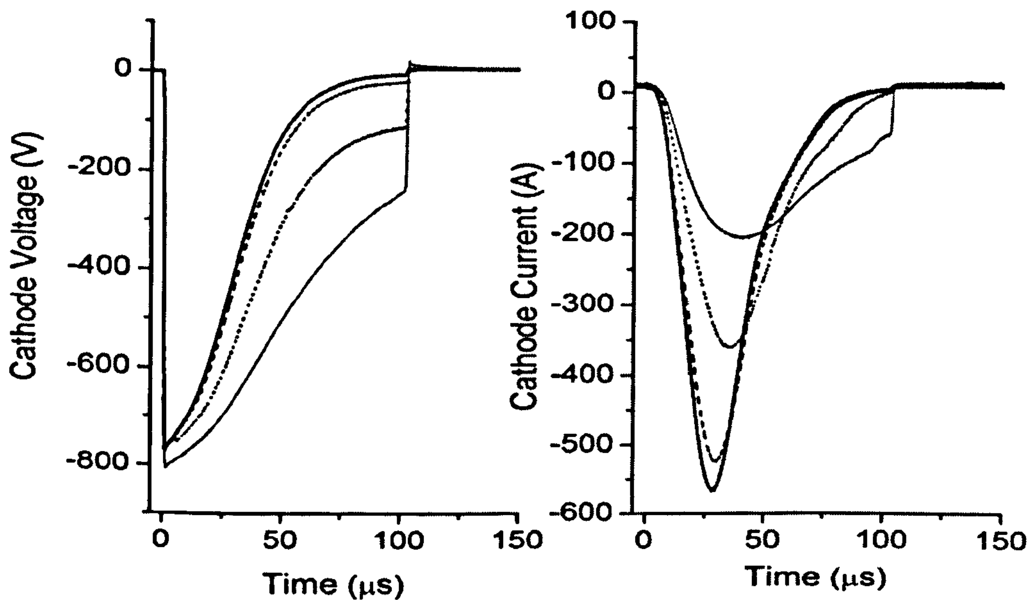

Figure 5.14. The cathode voltage V_d and current I_d waveforms produced by the (a) SINEX 3.0 supply in the HiPIMS mode for an average discharge power of 680 W and a gas pressure of 0.54 Pa in all the four magnetic field configurations. The (1) thick continous line (——) for the magnetic field configuration 1 (2) The dashed line for (– – –) configuration 2 (3) The dashed-dotted line (– · – ·) for configuration 3 and (4) thin continous line (——) for configuration 4.

The power density with different magnetic field strengths has been measured. The measurements were carried out at three different frequencies of 75, 100 and 150 Hz. The pulse 'on-time' for all the frequencies used was kept constant at 100 μs. Therefore, the duty factors were 0.75%, 1% and 1.5% for 75, 100 and 150 Hz respectively. In order

to keep the average power constant at all the frequencies used, the cathode discharge voltages have been adjusted accordingly.

A plot of power densities verses magnetic field strength is shown in figure 5.15. Figure 5.15 clearly indicates that the power density decreases linearly with reducing magnetic field strength.

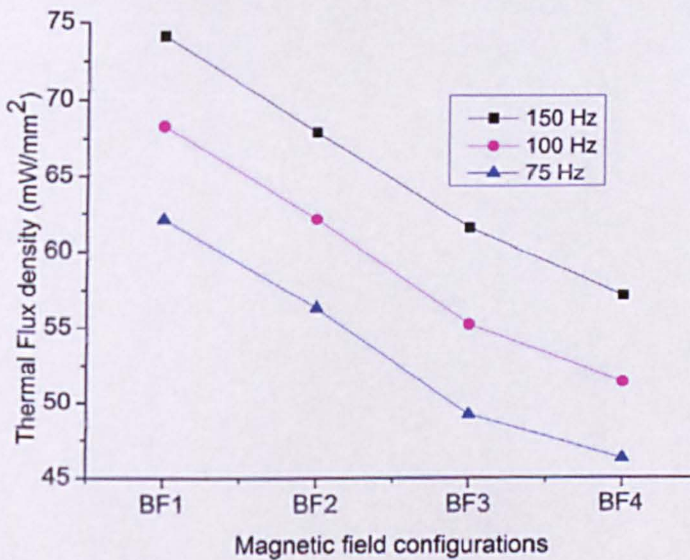

***Figure 5.15**: Plot of power densities verses magnetic field strengths in high power impulse magnetron sputtering discharges. Measurements were carried out at 100 mm away from the cathode surface and above the racetrack (r = 45 mm). The four chosen magnetic field strengths are shown as BF1, BF2, BF3 and BF4.*

It is reduced by ~30% (from 68 to 52 mW/cm^2) at a pulse frequency of 100 Hz when the magnetic field is reduced by an amount of 45%. This is an important observation in the sense that the deposition rate increases with reducing magnetic field strength (details of this finding will be discussed in later chapter of deposition rates measurements),

therefore power density per particle is reduced with reducing magnetic field in a HiPIMS discharge. The reason why power density in HiPIMS discharges is lower at lower magnetic field strengths can be explained as follows. The thermal probe was floating therefore it achieved a negative self-biasing voltage. The main depositing species on the probe is metallic and plasma ions. It has been observed that the strength of the potential barrier infront of the cathode surface reduces at lower magnetic field strength [105]. Therefore the ions produced from the sputtered metal atoms will have less energy and therefore will deposit less power onto the substrate.

Another observation is that the power density increases with increasing frequency. As the frequency was increased from 75 to 150 Hz, the power density was increased by ~27%. This result is not a higher the frequency results in a higher deposition rate that, in turn, increases the power deposited onto the substrate.

5.3.3 Langmuir Probe Measurements

The temporal investigation of plasma properties such as plasma density and plasma temperature against the magnetic field strength has been carried out to further understand the plasma dynamics and to know whether it contributes to the power density onto the substrate. Measurements have been carried out at two different magnetic field strengths – magnetic field configuration 1 (BF1) and magnetic field configuration 3 (BF3). The results are discussed in conjunction with the power density measurements to understand the reason responsible for the observed results.

5.3.3.1 The Evolution of Plasma Parameters

To extract plasma parameters such as plasma density (n_e), electron temperature (T_e) and the plasma potential (V_p) from measured Langmuir probe I-V characteristics, various conditions must be satisfied in order to apply the correct current collection theory discussed in section 3.5. The basic assumption of all these theories is a Maxwellian distribution of electron velocities, more commonly referred to as a single Maxwellian electron temperature T_e. It is common however, in some discharge plasmas including magnetron plasmas, that the measured electron temperature cannot accurately be represented by that of a single Maxwellian distribution [71-75]. Electron energy distribution functions (EEDFs) have been measured at 88 mm away from the cathode surface and above the racetrack (Z = 88 and R= 45 mm) during the pulse 'on-time' (t = 40 µs) and pulse 'off-time' (t = 150 µs) at an average power of 680 W and an average pressure of 0.54 Pa and shown in the figure 5.16. The discharge was pulsed at 100 Hz and the pulse 'on-time' was 100 µs. The Druyvesteyn's method has been used to obtain values of n_e, T_{eff} and V_p as this technique is applicable to all forms distribution function finds the distribution of electron energies from the second derivative of probe data using the assumption that the distribution is spherically symmetric.

Figure 5.16 shows the time evolution of the EEDF at two different time location – first one shown with a continous curve is at 40 µs and second one shown with a dotted curve is at 150 µs after the initiation of the discharge during the discharge cycle. The plot clearly indicates that EEDF during the pulse 'on-time' is wider than that in the pulse 'off-time'.

As the pulse switches off, there is no source of energy for electrons and they lose their energy via collisions.

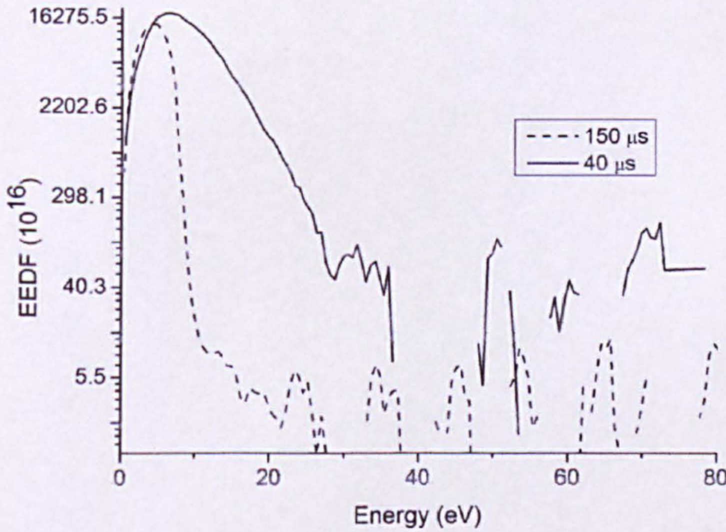

***Figure 5.16**: Evolution of electron energy distributions (EEDF) in bulk plasma (Z = 88 mm) at 40 μs (on-time) and 150 μs (off-time). Both of these distributions have been measured at magnetic field configuration 1 (BF1). The discharge was pulsed at 100 Hz and pulse 'on-time' was 100 μs.*

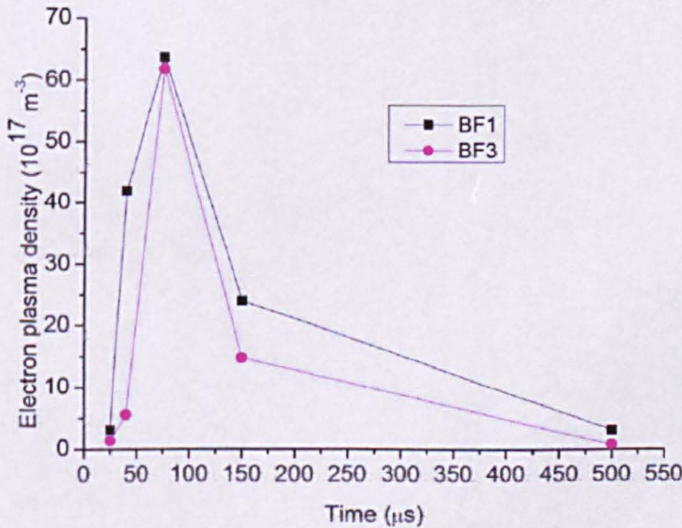

Figure 5.17: A plot of time-resolved plasma density profile in bulk plasma (Z = 88 mm) at two different magnetic field configurations (BF1 and BF3). The discharge was pulsed at 100 Hz and pulse 'on-time' was 100 μs.

From the measured EEDF, the plasma parameters such as plasma density, plasma temperature and plasma potential have been calculated. The plasma potential has been obtained from the point where $d^2I_e/dV^2 = 0$ in the measure probe characteristics.

Figure 5.17 shows the plasma electron density evolution at two magnetic field strengths. The plot clearly indicates that as the discharge is switched on, the plasma density develops and it peaks around 75 μs after the initiation of the discharge pulse for both magnetic field strength and it differs very slightly (~ 5%), however the peak discharge current is significantly differs (see figure 5.14). The important point is that the plasma density is always lower at lower magnetic field strength (BF3). During the pulse on-time – at t = 40 μs, the plasma density is one order higher (6.4×10^{12} per cc) in configuration 1 than that in the configuration 2 (6×10^{11} per cc). It is not surprising because at lower magnetic field strength, ionization efficiency is lower due to less electron trapping.

Figure 5.18 shows the evolution of the electron plasma temperature at two different magnetic field strengths. It is interesting to observe that the electron temperature increases with lowering the magnetic field strength.

When these results are viewed in conjunction with the power density onto the substrate, it can be inferred lower plasma density infront of the substrate at lower magnetic field strength might be a probable cause of lower power density at lower magnetic field strength.

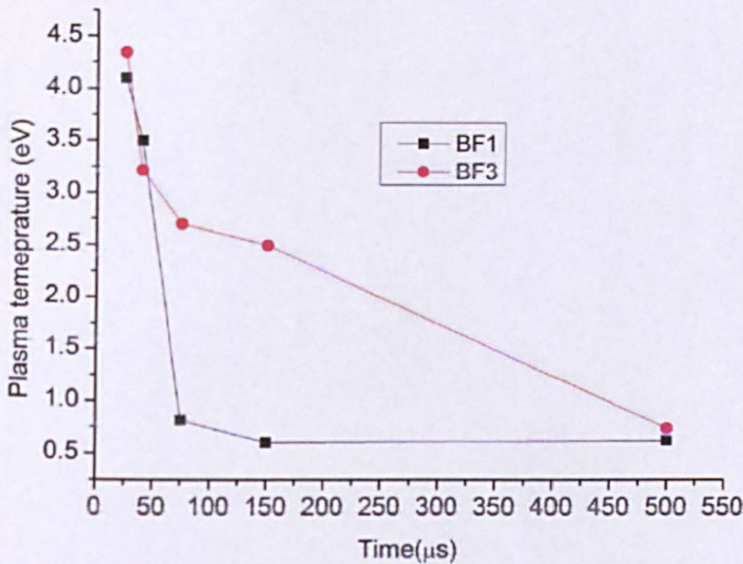

Figure 5.18: A plot of time-resolved plasma electron temperature profile in bulk plasma (Z = 88 mm) at two different magnetic field configurations (BF1 and BF3). The discharge was pulsed at 100 Hz and pulse 'on-time' was 100 μs.

5.4 Conclusions

A power probe has been used successfully to measure the power density onto the isolated substrate in high power impulse magnetron sputtering discharges. The measurements were carried out to investigate the magnetic field effect on the power density in HiPIMS discharges. Measurements indicate the power density is linearly proportional to the applied power in all the modes of operation. It was found that the power density is significantly reduced in the HiPIMS discharge compared with conventional DC and pulsed-DC magnetron sputtering at the same average power levels.

It was also observed that the magnetic field strength of the magnetron can be used to control the thermal loading of the substrate. By reducing the magnetic field strength by

45% could reduce the power density onto the substrate by 28%. This finding is very important in the context of depositing thin films onto the thermally sensitive substrates such polymeric web. Lowering the discharge pulse frequency also reduces the power density.

Electron plasma density measured by the Langmuir probe indicates lower plasma density at lower field strength which might be the probable cause of lower power density at the substrate.

Chapter 6

DEPOSITION RATE MEASUREMENTS

Despite having many advantages, the HiPIMS technique has the major drawback of lower deposition rates than those in conventional DC magnetron sputtering and pulsed DC magnetron sputtering at the same average power levels. To understand the reasons responsible for it, a systemic investigation has been carried out and is being reported in this chapter.

The magnetic field strength of the magnetron and its topology is a crucial global parameter that affects plasma transport in the discharge body that, in turn, influences the deposition rates. Therefore, the study of magnetic field effect on deposition rate has been carried out and compared with the deposition rates in DC magnetron sputtering and the pulsed-DC magnetron sputtering.

Experimental findings suggests that the deposition rate can be controlled by varying the magnetic field strength, however trends in deposition rates versus magnetic field strengths in HiPIMS and pulsed DC were found opposite. This chapter details these investigations and its findings.

6.1 Introduction

Although HiPIMS has provided new process parameters that have the potential of enhancing the film quality and adhesion, it was noticed in most of investigations that the deposition rate, normalized to average power, is significantly lower than in DC magnetron sputtering and pulsed-DC magnetron sputtering discharges [50].

Deposition Rates Measurements

Since the deposition rate is an important process parameter in thin film deposition technology, many investigations were carried out by various researchers to find out the causes of the observed lower deposition rates. Based on these investigations, various ways were reported to enhance it. Bohlmark et. al. [80] reported that it is the magnetic field perturbation that is responsible for the observed lower deposition rates in the HiPIMS discharges and demonstrated that an additional external magnetic field can enhance the deposition rate by 80% for the sample placed at the central axis. Emmerlich et. al. [79] reported the nonlinear dependence of the sputtering efficiency on the target voltage and therefore it is unreasonable to compare the deposition rates in DC and HiPIMS modes. By decreasing the transverse magnetic field (B_t) by 33% (from 50 mT to 17 mT) an increase of 70% in deposition rate (270 to 360 $nmh^{-1}kW^{-1}$) has also been reported [129]. Christie et. al. [77] developed a phenomenological model and predicted that the back-scattering of ions towards the cathode is the root cause of the observed lower deposition rates. A spatial and temporal resolved plasma potential investigation in the HiPIMS discharges [105] reported that the existence of the strong potential barrier in front of the target hampers the transport of the plasma ions towards the substrate and hence causes the lower deposition rates. It was also suggested that the time lag between the target voltage and discharge current is responsible to the lower deposition rates and a novel pulsing technique (high voltage discharge with low voltage pulse at the end) was proposed that could enhance the deposition rates by two times [130].

An experimental study carried out to investigate the deposition rate dependence on the magnetic field strengths in pulsed DC discharges revealed a slight increase in deposition rates with a decrease in magnetic field strength [131]. These deposition rates were compared at constant discharge current. Therefore applied average power had been increased to maintain constant discharge current. For a decrement of more than 50% in magnetic field strength (from 422 to 184 G), a slight increase (~ 5%) in deposition rate has been observed at 5 cm away from the target. It was concluded in that study that this slight enhancement in deposition rates is the result of the increased average power. However, in our case the average power was kept constant instead of the average discharge current.

A comparative study has been reported to investigate the effect of magnetic field strength and topology of the magnetron and the pulsing frequency on the deposition rates in HiPIMS, DC and pulsed DC discharges at the same average power levels. These experimental findings have also been compared with the prediction of the deposition rates using a simple computational model. We also investigate the effect of thickness of the sputtering targets on the deposition rates.

6.2 Experimental Arrangements

A schematic diagram of the magnetron arrangement together with the position of deposition rate monitor is shown in figure 2.2 (Chapter 2).

Deposition Rates Measurements

The deposition rate measurements were carried out above the racetrack at a radial position of r = 45 mm and an axial position of z = 100 mm, using the Maxtek TM-400 multi film deposition rate monitor (equipped with 6 MHz quartz crystal oscillator and silver sensor). Although the deposition rate varies during the pulse, the slow response of the sensor allows only time-averaged values to be determined (in our case from the total thickness measured in the fixed chosen deposition time of 120 s). One important region of the discharge is the magnetic trap, indicated in the figure 2.2 and defined by a region enclosed by magnetic field lines that intersect the target twice.

The magnetic field strengths and directions have been determined from bench measurements of magnetic field taken in the axial (B_z) and radial directions (B_r) using a Hall probe as discussed earlier in chapter 2. The magnitude of total B-field $|B| = \sqrt{(B_z^2 + B_r^2)}$ along the line of deposition rate measurements is shown in figure 2.3. As the magnets are withdrawn, B drops by ~ 40 % at the target.

The plasma source was energized by a SINEX 3.0 HiPIMS power supply (from Chemfilt Ion Sputtering). The target was sputtered at frequencies of 75, 100 and 150 Hz with an "on-time" of 100 μs in an argon gas environment (purity 99.99%), at a pressure of 0.54 Pa and a time-averaged power of 680 W (± 5%). The peak target power and current density in this study were ~ 3 kW cm^{-2} and ~ 2.7 A cm^{-2} respectively. Typical cathode voltage and current waveforms obtained at a pulse frequency of 100 Hz at four chosen magnetic field strengths are shown in figure 6.1.

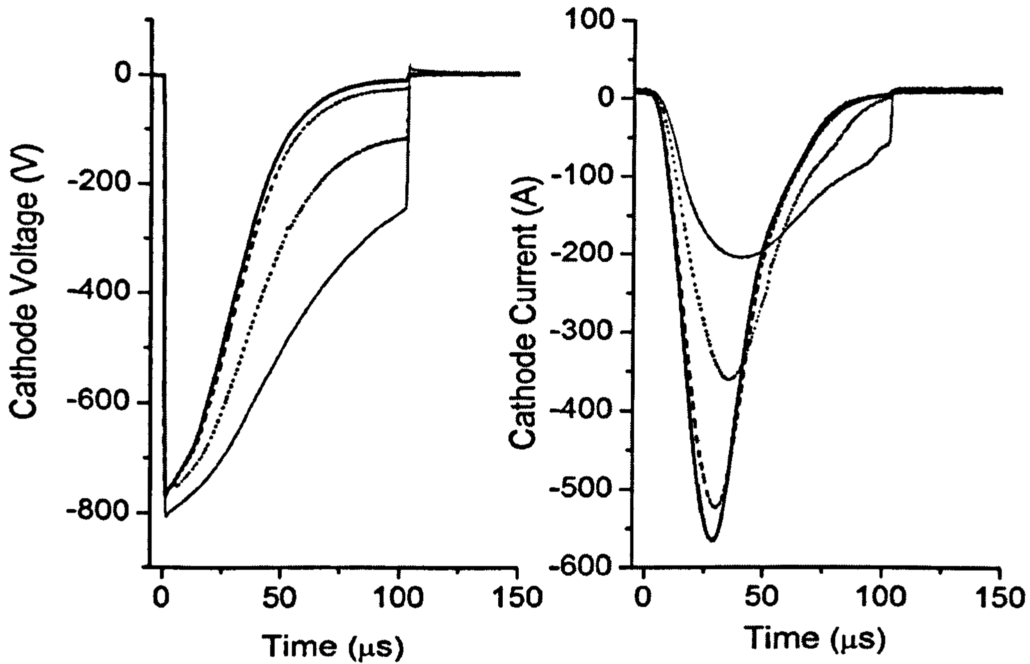

Figure 6.1 : The cathode voltage V_d and current I_d waveforms produced by the SINEX 3.0 supply in the HiPIMS mode for an average discharge power of 680 W and a gas pressure of 0.54 Pa in all the four magnetic field configurations. The (1) thick continous(———) line for the magnetic field congiguration 1 (2) The dashed line (– – –) for configuration 2 (3) The dashed-dotted line (– • –) for magnetic field configuration 3 and (4) thin continous line (——) for configuration 4

For operation in DC and pulsed DC modes, the discharge was triggered by a Pinnacle Plus$^+$ power supply unit from Advanced Energy Incorporated. This is an asymmetric bipolar DC pulsed supply capable of producing output waveforms in the frequency range between 0 to 350 kHz. The pulse 'off-time' can be adjusted by the user to provide various duty factors. In the present study, two frequencies of 100 and 350 kHz were used with 50% duty factors i.e. 'pulse on-times' were 5 and 1.43 μs, respectively. The power supply was used in power regulation mode.

The typical cathode voltage and pulse waveforms during 100 and 350 kHz at four chosen magnetic field configurations are shown in the figures 6.2 and 6.3 respectively.

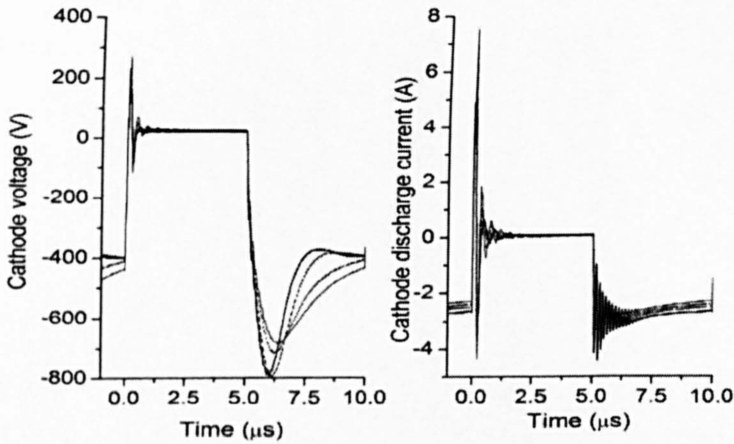

***Figure 6.2**: The cathode voltage V_d and current I_d waveforms for100 kHz pulsed DC mode for an average discharge power of 680 W and a gas pressure of 0.54 Pa in all the four magnetic field configurations. The (1) thick continous line (——) for the magnetic field congiguration 1 (2) The dashed line (– – –) for configuration 2 (3) The dashed-dotted line (– · – ·) for configuration 3 and (4) thin continous line (——) for configuration 4. The duty factor was kept constant at 50%.*

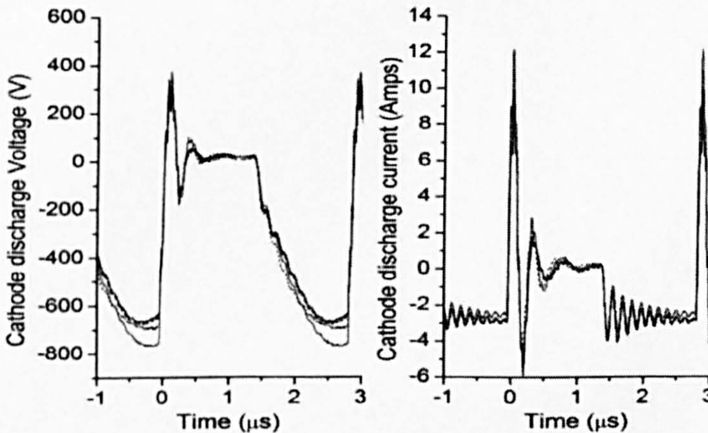

***Figure 6.3.** The cathode voltage V_d and current I_d waveforms for350 kHz pulsed DC mode for an average discharge power of 680 W and a gas pressure of 0.54 Pa in all the four magnetic field configurations. The (1) thick continous line (——) for the magnetic field congiguration 1 (2) The dashed line (– – –) for configuration 2 (3) The dashed-dotted line(– · – ·) for configuration 3 and (4) thin continous line (——) for configuration 4. The duty factor was kept constant at 50%.*

These cathode voltage (V_d) and current (I_d) waveforms were measured at an intermediary aluminium test box placed between the power supply and the magnetron source using a x100 voltage probe (P5100 Tektronix Ltd model) and a x20 current probe (Tektronix Ltd Model TCP 04) in conjunction with a x10 current probe (Tektronix Ltd Model TCP 202) respectively. The reference time t = 0 was defined as the zero voltage crossing point between the 'off' and 'on' phases of the V_d pulse. The discharges were operated at an average discharge power of 680 W and a gas pressure of 0.54 Pa in all the four magnetic field configurations. From the plots in HiPIMS mode and magnetic field configuration 1 (maximum magnetic field strength), we see that in the initial phase, V_d ramps down rapidly from 0 to -650 V in 200 ns, then relaxes somewhat to reach -600 V in the next 20 μs. After this, V_d increases up to 0 V in 100 μs. The cathode current I_d lags cathode voltage V_d, having a maximum value of 230 A which occurs 40 μs after initiation of the discharge pulse. The time lag between I_d and V_d and the time of the establishment of the peak discharge current varies with magnetic field strength.

6.3 Results and discussions

All the deposition rate measurements were carried out above the racetrack position, 100 mm away from the target (r = 45 and z = 100 mm). The deposition rate has been calculated as the deposited film thickness per unit time at a constant average power. For the present study, the film thickness has been measured for a deposition time of 120 seconds. To compare the deposition rates during all the modes of operation, the average power over the time has been chosen as a parameter and it is given as

$$P_{av} = \delta \int_0^{t_p} I(t)\, V(t)\, dt \qquad eq(6.1)$$

Where $\delta = t_{on} / (t_{on} + t_{off}) = t_p f$. Here δ is the duty factor, t_p is pulse duration that is $t_{on} + t_{off}$ and f is the pulse frequency. The average power has been kept constant at 680 W by varying the cathode discharge voltage V_d.

Figures 6.1 – 6.3 show the cathode discharge voltage V_d and cathode discharge current I_d in the three pulsed modes of operations such as 100 Hz HiPIMS, 100 and 350 kHZ pulsed DC respectively. From the plots in the figure 6.1, it is clear that peak discharge voltage V_d increases marginally (~ 5% of the peak voltage in magnetic field configuration 1) by decreasing B-field strengths (~ 40%) in the HiPIMS mode and peak discharge current I_d decreases significantly (~ 64%). However, in pulsed DC mode the change in the cathode discharge current is not so prominent with changing magnetic field strengths. For the pulsed DC measurements, the duty factor was kept constant at 50%. However, in the HiPIMS mode the duty factor could not be kept constant due to the limitations offered by the HiPIMS power supply.

6.3.1 Effect of Magnetic Field on Deposition Rates in HiPIMS

To study the effect of magnetic field strength on the deposition rates in the HiPIMS mode, three different frequencies 75, 100 and 150 Hz have been chosen. In all these frequencies, pulse 'on-time' was kept constant as 100 μs, therefore their duty factors were 0.75 %, 1 % and 1.5 % respectively. The average power was kept constant

therefore, the lower the frequency, the higher the peak power density or peak current density.

The magnetic field strength influences the deposition rate significantly in the HiPIMS discharges as shown in the figure 6.4 with dotted curves. The deposition rate almost doubles (7.48 nm to 14.72 nm/min at 100 Hz pulse frequency) at the typical substrate position ($z = 100$ mm) by reducing the magnetic field strength by 40% at the target position.

The observed increase in the deposition rates can be explained on the basis of following arguments. At lower plasma confinement at the lower magnetic field strengths. The finite Larmor radius (FLR) of electrons plays an important role in the cross field transport of the plasma. The shorter the electron Larmor radius r_L, he stronger is the plasma confinement. As the Larmor radius r_L is inversely proportional to the magnetic field strength ($r_L \sim B^{-1}$), a lower magnetic field means r_L is higher and hence plasma (electrons and ions together) can diffuse from the magnetic field lines more easily to the substrate. Secondly, in this study, the magnetic field strength is reduced by pulling back the magnetron's magnets. It reduces the size of the magnetic trap and therefore reduces the size of plasma confinement region.

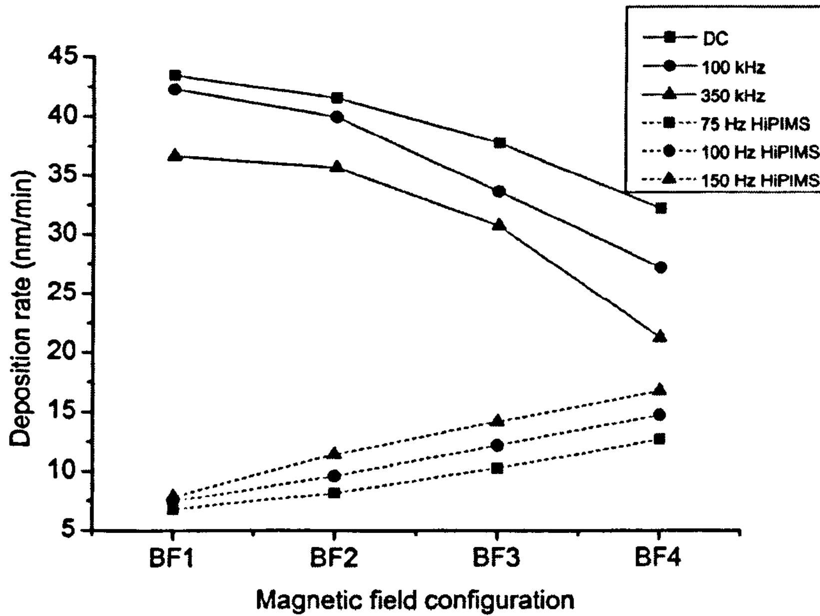

Figure 6.4. A plot of deposition rates versus magnetic field strength in the HiPIMS, DC and pulsed DC modes of operations. The average power and pressure was kept constant at 680 W and 1.08 Pa respectively for all the measurements.

Although, only the electrons are magnetized in the magnetron's magnetic field geometry, it also affects the ion transport due to ambipolar diffusion. Therefore the reduced size of the magnetic trap region effectively reduces the ion retarding space in the plasma bulk. This, in turn, enhances the ion transport towards the substrate and therefore the deposition rates. The third and the most important reason is the lower strength of the potential barrier existing in-front of the target at the lower magnetic field strength. In another experiment carried out with similar parameters [105], it was observed that the height of the potential barrier in front of the target reduces with lowering magnetic field strength. Therefore the ion flux has to face less retarding force while travelling towards the substrate, which results in higher deposition rates.

To explain the observed higher deposition rate at higher pulse frequency, one could argue that at the higher frequency, the target-substrate gap is more frequently filled with electrons and ions produced during the pulse. At higher frequencies, the plasma between the target and substrate has less time for relaxing. This, in turn, increases the time charge particle density in this gap and therefore produces better plasma on-time conductivity. As the plasma conductivity plays a crucial role in the ion transport towards the substrate [131], therefore transport of the plasma particles towards the substrate would be more efficient at higher frequencies and it, in turn, increases the deposition rates as observed in this study.

Axial variation of the deposition rate with various magnetic field strengths and with older (thinner and more pronounced racetrack region) targets has been reported [105]. The average power and the average pressure for those experiments were 750 W and 1.08 Pa respectively. The plot reported in [105] indicates that a reduction of 33% of magnetic field strength (375 G to 250 G) at the target position increases the deposition rate by 6 times at the substrate position. This increased deposition rate is higher than those reported here. This older target produces a significantly higher current density (~1.5 times more and not shown here) at the similar power levels. Therefore, it is speculated that this increased current density might be responsible for larger enhancement of deposition rates with reducing magnetic field strength. Secondly, the magnetic field effect might influence the ion transport differently in experiments carried out with older targets due to a deeper racetrack groove and reduced thickness of the target. This change in magnetic field could also change sputtering and ionization

efficiencies and therefore can produce higher deposition rates. However, there is a need of more investigations to know all the responsible factors for this observation.

6.3.2 Effect of Magnetic Field on Deposition Rates in DCMS and pulsed DCMS

The deposition rate measurements against magnetic field strength in DC, 100 and 350 kHz pulsed DC discharges have been shown in the same figure 6.4 with continuous curves. The results indicate that deposition rates in pulsed DC and DC modes of the discharge increases with the magnetic field strength. Therefore, here, decreasing trends in the deposition rates with lowering of the magnetic field can be attributed to the reduced charge particle densities and lower sputter rates from the target as the effective plasma confinement is reduced. Reduced magnetic field strength reduces the electron plasma density, that, in turn, reduces the discharge current. It results in reduced sputtering rates of the cathode and it eventually produces lower deposition rates. The observed decreasing trend in the deposition rates with increasing pulse frequency can be understood on the basis of the arguments proposed in [132] that there is a dead time (500 to 1000 ns) associated with each pulse 'on-time'. During this dead time, negligible amounts of sputtering take place. This dead time becomes an increasingly significant proportion of the pulse on-time as the pulse frequency is increased. This, in turn, reduces the total sputtering and therefore reduces the deposition rate with increasing frequencies.

6.3.3 Modeling of the Effect of the Magnetic Field Strength on Deposition rates

Using the nuclear stopping power formula and Lindhard electronic stopping power formula, Yamamura and Tawara [133] proposed a simplified empirical formula for the energy dependence of the sputtering yield

$$Y(E) = 0.042\frac{Q(Z_2)\alpha(M_2/M_1)}{U_s}\frac{S_n(E)}{1+\Gamma k_e\varepsilon^{0.3}}\left[1-\sqrt{\frac{E_{th}}{E}}\right]^s \qquad eq(6.2)$$

Where M_1 and M_2 are the masses of the sputtering gas and target respectively. α is a constant that determines the energy deposited at the surface and the function of masses of the of the target and the sputtering gas and also has the Z_2 dependence factorized as $Q(Z_2)$. $S_n(E)$ and k_e are the nuclear and electronic stopping powers, respectively. The term ε is the reduced energy and depends upon the masses and atomic numbers of the target and sputtering gas and the energy of the incident ions on the target. The factor Γ is expressed as [133],

$$\Gamma = \frac{W(Z_2)}{1+(M_1/7)^3} \qquad eq(6.3)$$

E_{th} is the threshold energy for sputtering of titanium (Ti) and is given as [133],

$$\frac{E_{th}}{U_s} = \frac{1+5.7\times(M_1/M_2)}{\gamma} \qquad eq(6.4)$$

where γ is the energy factor and is given as $4\, M_1 M/(M_1+M_2)^2$.

The surface binding energy U_s and the best fit values of Q, W and s for the titanium (Ti) target is given as 4.85 eV, 0.54, 2.57 and 2.5 respectively [135].

Here the deposition rates have been calculated as

$$\rho_d = \delta \int_0^{t_p} I_d(t)\, Y_E(t)\, dt \qquad eq(6.5)$$

where $I_d(t)$ is the cathode discharge current and $Y_E\,(t)$ is the sputtering yield given by eq. (6.3). Here, in calculating the deposition rates, it was assumed that deposition rates are proportional to sputtering rates and all the sputtered particles were deposited.

These calculated deposition rates together with measured deposition rates against the magnetic field strengths, in DC and pulsed DC modes of the operation, are plotted in figure 6.5. It should be noted here that the calculated deposition rates are arbitrary in values. Therefore these values have been multiplied by a constant number that makes deposition rates similar in the magnetic field configuration 1. This exercise has been done for the illustration purposes only. The results plotted in figure 6.5 indicate that the variation in the calculated deposition rates against magnetic field strength have similar trends to the measured values. These trends arise because lowering the magnetic field strength lowers the plasma density, which in turn, reduces the total sputtering and therefore the deposition rates.

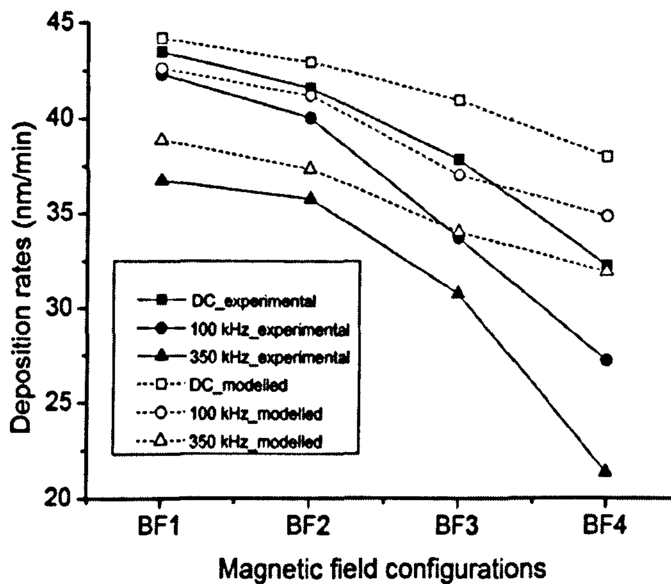

Figure 6.5: A plot of the deposition rates against the magnetic field strength in the DC and pulsed DC modes. The continous lines with solid symbol are for the experimental

It should be noted here that the calculated sputtering yield (Y) always increased with lowering magnetic field in all modes of the operation because lowering the magnetic field strength resulted in increasing cathode discharge voltage to maintain the constant discharge power.

These findings can be explained as follows. In the DC and pulsed DC discharges, the major proportion of the depositing flux is made of sputtered neutrals. As the magnetic field strength is lowered, the cathode discharge current reduces and it reduces the sputtering metal flux that results in the observed lower deposition rates.

The effect of magnetic field strength on deposition rates in the HiPIMS discharges has been shown in figure 6.6.

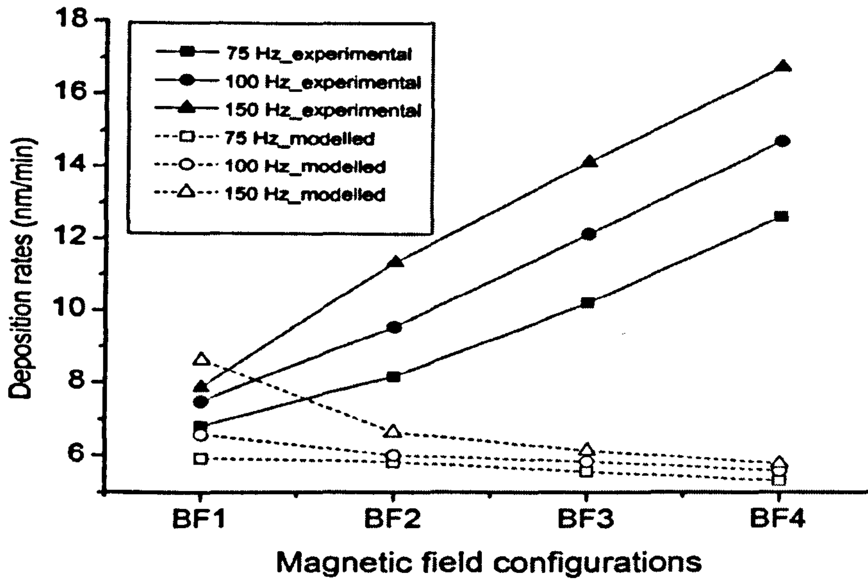

Figure 6.6 : A plot of the deposition rates against the magnetic field strength in the HiPIMS mode. The continous lines with solid symbol are fro the experimental results and the dashed lines with hollow symbols are for the modelled deposition rates.

From the plot 6.6, it is clear that the calculated deposition rates have opposite trends to the measured deposition rates. It can be explained as follows.

In the HiPIMS discharges, the major proportion of the deposited metal flux (~90%) [18] is made of metallic ions. These metallic ions are formed by the ionization of the sputtered neutrals flux. These ions, therefore, have typically the same energy as sputtered neutrals, given by the Sigmund-Thompson distribution. As the magnetic field strength is lowered, the strength of the potential barrier is reduced (see in figure 4.16), therefore less energetic ions are able to surmount the potential barrier and become deposited at the substrate.

Secondly, the lowered magnetic field strength decreases the effective confinement of plasma electrons, therefore electrons can diffuse more readily. Since the thermalized and sputtered ions follow the electrons, they can also diffuse towards the substrate more readily at lower magnetic field strength resulting in the higher deposition rates.

6.4 Conclusions

A comparative study of magnetic field effect on the deposition rates in the HiPIMS, DC and pulsed DC discharges has been carried out using a deposition rate monitor.

It was found that the magnetron's magnetic field strength is a crucial parameter that determines deposition rate for a given set of operating conditions. The measurements carried out in the HiPIMS mode show that the deposition rates increased by a factor of 2 times with lowering the magnetic field strength by 40% at the target. Increasing the pulse frequency at constant pulse on-time also enhances the deposition rates due to increased duty factor and more plasma present above the substrate on time-average.

However, investigations carried out in the DC and pulsed DC (100 and 350 kHz) modes revealed that deposition rate decreases with the lower field strengths due to less ionization efficiency, reduced plasma densities and lower sputtering rates.

Chapter 7

MEASUREMENT OF ION ENERGY DISTRIBUTION FUNCTION IN HiPIMS DISCHARGE

This chapter describes the time-resolved ion energy distribution functions (IEDF's) at the substrate position in a HiPIMS discharge investigated using a commercial quadruple energy-resolved mass spectrometer, incorporating a double gating ion shuttering technique as discussed in chapter 3.

7.1 High Time-Resolved IEDFs in HiPIMS Discharges

This section details the demonstration of Electrostatic Ion Shuttering Technique to measure very high time-resolved ion energy distribution functions in HiPIMS discharges and its findings.

7.1.1 Introduction

IEDFs measurements in HiPIMS discharges have been carried out by a number of researchers using energy-resolved mass spectrometry in the time-averaged as well as the time-resolved modes. Bohlmark et. al. [19] carried out such studies with a Ti target and found that the time-averaged IEDF's are typically broader than in DC magnetron sputtering (DCMS) discharge. They also showed that the time-resolved IEDFs (of Ar^+ and Ti^+) have broad distributions (up-to 100 eV) in the early stage of the discharge pulse, which quickly narrow as the pulse ends. Burcalova et. al. [134] observed in a similar HiPIMS discharge that with decreasing working gas pressure, a significant high energy tail develops in the time-averaged IEDF's, and the fraction of the ionized metal flux to metal neutrals increased with the average current in the pulse.

Hecimovic et. al. [135] performed time-averaged IEDFs measurements of Ar^+ and Cr^+ ions and found that for both species a high-energy tail existed and increased with the increasing target current. The energy corresponding to the peak counts (at 2- 4 eV) was independent of the discharge current since the low energy ions are a remnant of a post discharge plasma which was found to exist. The ion flux transformed from metal-dominated to gas dominated as magnetic field decreased [136].

Vlcek et. al. [137] carried out time-averaged mass spectroscopic measurements at pressure up-to 5 Pa and target current density in the pulse up to 950 W/cm^2. They observed that copper ions are strongly dominant (up to 92%) in total ion fluxes onto the substrate. They also found that the energy distributions with broadened low-energy part at a lower pressure were extended to higher energies (up to 45 eV relative to ground potential).

Although many of these studies have increased knowledge of the species and energies present in the HiPIMS discharge there is lack of detailed information on the time-evolution of the ion energies at the substrate. The time-resolved experimental studies of Bohlmark et. al. [19] despite providing some measurements of the evolution of the IEDF's, the time-resolution was limited to 20 μs and the number of full distributions obtained per cycle was limited to three. This paper investigates the time-evolution of IEDFs in a HiPIMS discharge during the entire pulse with a temporal- resolution of 10 μs.

7.1.2 Experimental Set-up

Experimental set-up consists of the technique used to measure the IEDFs and experimental arrangements.

A technique for obtaining high time-resolution ion energy distribution functions (IEDFs) at the substrate in depositing plasma has been developed, and applied to a High Power Impulse Magnetron Sputtering (HiPIMS) discharge. Key to this technique is the electrostatic gating of ions inside the instrument end cap. The present work is original in the following sense: it demonstrates a newly developed gating technique in order to achieve IEDF measurements in HiPIMS discharges with time resolution better than 2 μs over the entire cathode voltage pulse period.

An electrostatic ion shuttering technique in conjunction with HIDEN EQP 300 (*Electrostatic Quadrupole Plasma* analyser) energy-resolved mass spectrometer [126] was used for time- resolved IEDFs measurements. The details of this technique have been described in chapter 3 (section 3.3.1). The spectrometer was equipped with 45^0 energy sector and SEM (Secondary Electron Multiplier) to count the ions. It provides energy resolution up-to 0.1 eV but in the present experiments a 0.5 eV energy resolution was chosen due to the long acquisition times (~3 minutes) in a single scan. Before choosing this energy resolution setting, the IEDFs were scanned at 0.1 and 0.5 eV energy resolutions and no significant changes, in counts or in the shape of IEDFs, were observed. The mass spectrometer barrel was located opposite the racetrack at a distance of 10 cm (see figure 7.1).

This orientation provides direct line-of-sight between the instrument and surface of the cathode, increasing the probability for the sputtered target material to enter the instrument without undergoing any collisions. The plasma ions were sampled through an orifice of 100 µm in diameter drilled on the grounded end cap of the instrument. The electrostatic shutter [138] was made from a stainless steel mesh having 57 wires/inch and a 45% geometrical transparency. It was situated 0.5 mm behind the orifice (see figure 3.7, Chapter 3). An electrostatic pulse, produced by an external pulse generator, was biasing the mesh via a feed-through. Both the grid and the detector were gated by an external delay generator at a prescribed time delay.

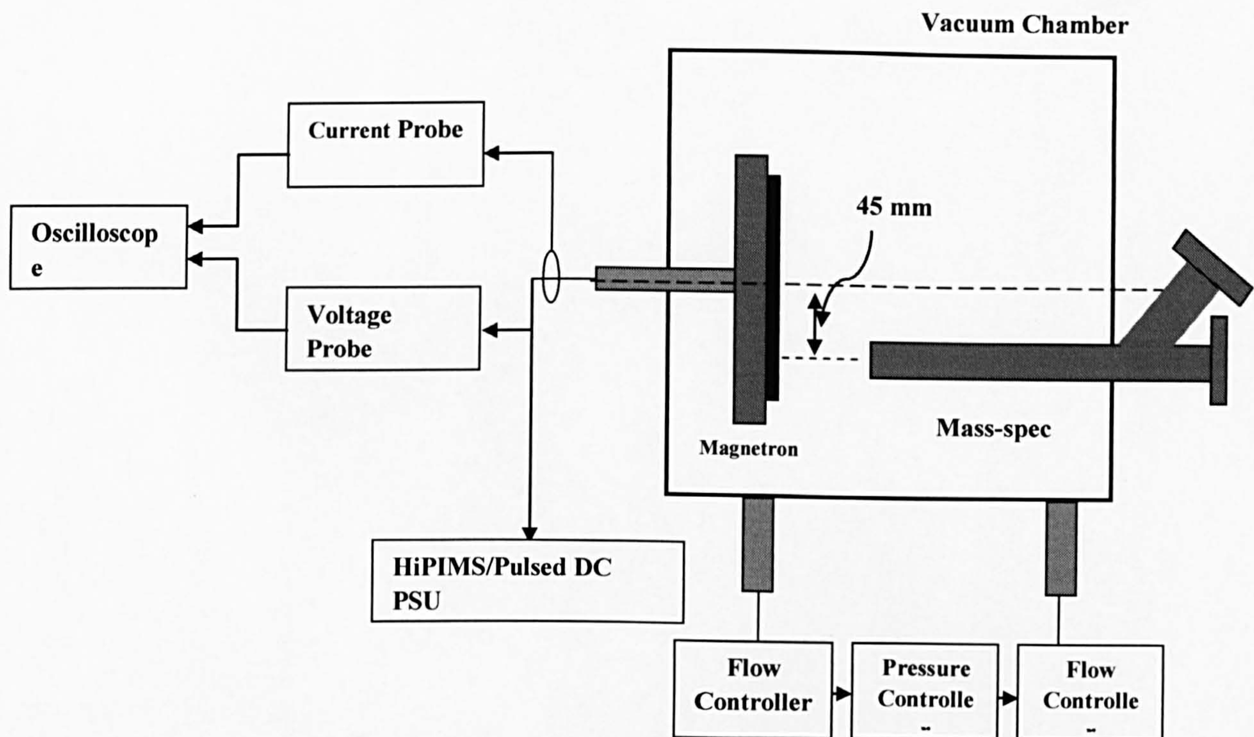

Figure 7.1*: A schematic of experimental set-up used for IEDFs measurements*

The time t=0 position was defined as the zero cutting edge of the target voltage pulse at the off-to-on transition. The details of gating scheme are shown in figure 3.8 (Chapter - 3).

The schematic of the experimental set-up is shown in figure 7.1

7.1.3 Results and Discussion

The time averaged IEDF for Ar^+ is shown in the figure 7.2. While sampling the time-averaged IEDFs, there was no mesh inside the mass spectrometer barrel. The intensity of signal written in terms of counts/sec has been plotted on the log scale while the energy is plotted in linear scale. The plot indicates that the peak counts occur at 3 V.

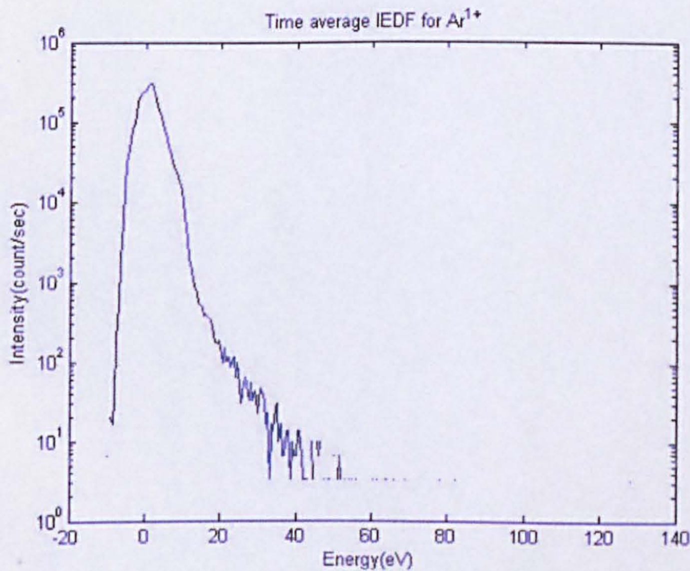

Figure 7.2: The plot of the IEDF in HiPIMS discharges for Ar^+. This measurement has been carried out at the constant power of 640 W and the average pressure of 0.27 mTorr.

It means most of the Ar^+ has the energy of 3 eV and it is an indication of the time averaged plasma potential of the discharge as reported in [19]. Before performing the detailed experiments for time-resolved measurements, a set of preliminary experiments was carried out to assess the performance of the electrostatic shuttering technique. For this, a summation of time-resolved IEDFs at different times during the pulse was compared to a time-averaged IEDF. The plot is shown in figure 7.3. Both of these IEDFs have been recorded in different experiments and with different tuning parameters of the mass spectrometer. The time-averaged IEDF was recorded without mesh in the instrument.

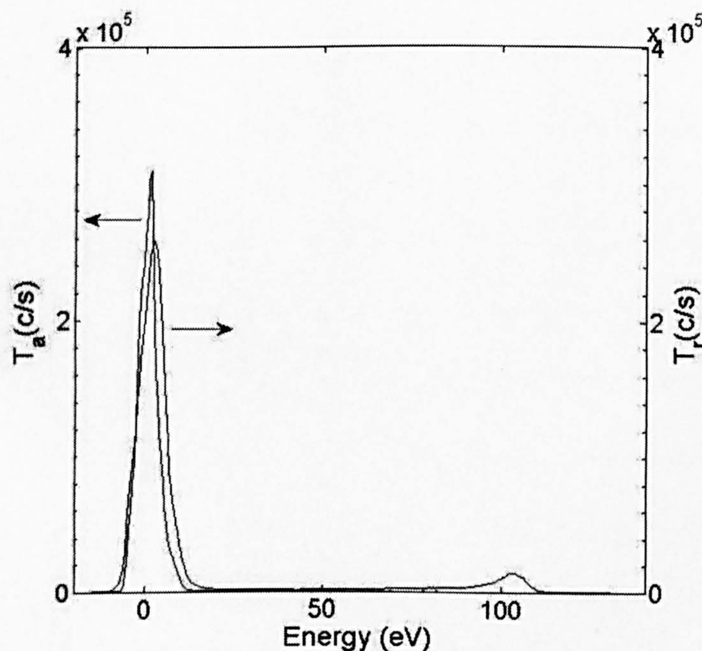

Figure 7.3: *A plot of time averaged IEDF for* Ar^+ *and the summation of all the time-resolved IEDFs in the same time window. A hump at 105 eV is an artefact produced by the biased mesh when there is fast transition from -22 V to 150 V, at the end of gating time window.*

As can be seen from plot, both of these IEDFs match well except that the sum of time-resolved IEDFs have a hump at 105 eV and lower number of counts. This hump is artefact produced by the biased mesh when there is fast transition from -22 V to 150 V, at the end of gating time window.

To confirm that this hump is indeed an artefact produced by the mesh, more experiments were carried out with different shuttering voltages on mesh and it was found that the position of hump follows the mesh biasing voltage.

The lower number of counts in the peak in the time-resolved IEDFs and the slight mismatch in both IEDFs can be attributed to different tuning parameters of mass spectrometer as both of these scans were recorded during different experiments. This test gave us the confidence that the used gating technique was performing well.

The time resolved IEDFs of Ar^+ and Ti^+, obtained at different parts of pulse cycle are shown in figures 7.4 and 7.5 respectively. These measurements were recorded after a prescribed time delay from the initiation of the cathode voltage pulse, with respect to ground potential (end cap of mass spectrometer was on ground potential). The time resolution was 2 μs and the measurements were recorded between 0 and 30 μs. The first appearance of Ar^+ ions was observed 8 μs after the initiation of the pulse. As can be seen in figure 7.4, Ar^+ ions have a distribution extending up to 20 eV. Further into the pulse, the energy distribution of Ar^+ ions spreads up to 35 eV, due to possibly the transfer of energy and momentum to them by Ti^+ via collisions. Similar energy spreads in the Ar^+ IEDFs have been reported by Bohlmark et al [19] for similar pressures.

The Ti^+ ions in figure 7.5 appear 14 μs after the initiation of the cathode voltage pulse, some 6 μs after the arrival of Ar^+ ions at the substrate. It clearly shows that there are two distinct phases of plasma - gas rich plasma followed by metal rich plasma - in agreement with [140 - 142]. The highest counts in the energy distribution of Ar^+ are seen at 3 eV and the energies spread up to 20 eV. Similarly the maximum in the Ti^+ ions counts in the energy distribution at 22 eV however these ions extend up to 100 eV. Bohlmark et al [19] have also reported the similar results.

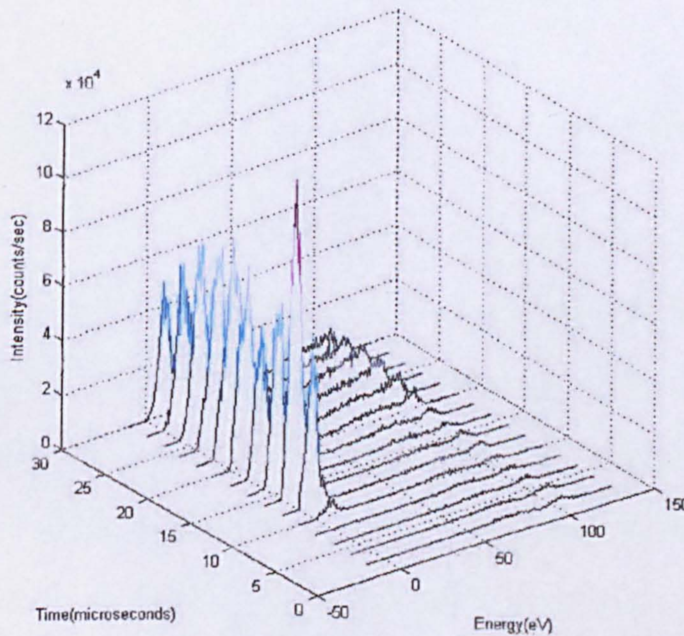

Figure 7.4: *A plot of time resolved IEDFs measurements in Ar^+ in the HiPIMS discharges. The IEDFs have been sampled for first 30 μs with the time-resolution is of 2 μs.*

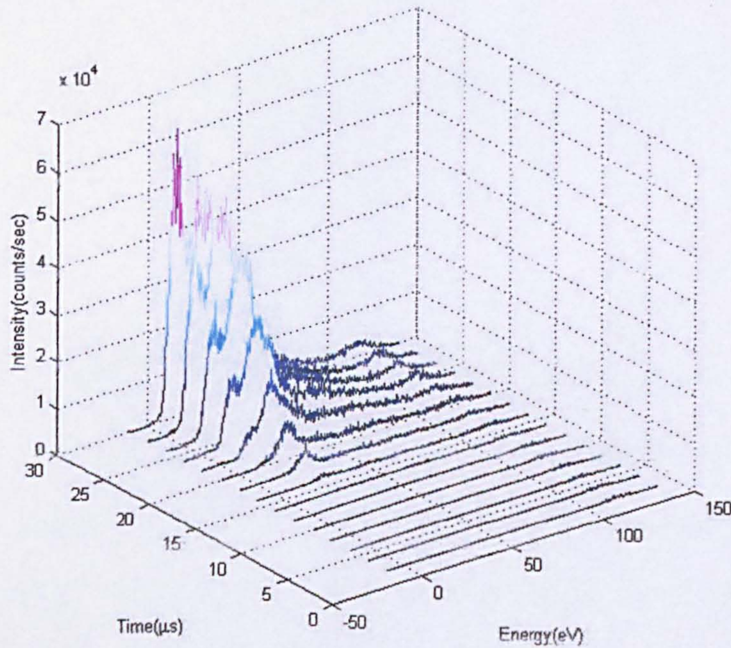

Figure 7.5: *A plot of time resolved IEDFs measurements in Ti^+ in the HiPIMS discharges. The time-resolution is of 2 μs.*

The observed energy of Ti^+ ions can be considered to come from two components, firstly due to plasma potential V_p at which they were created and secondly from the sputtering kinetic energy of Ti atoms before ionization. The origin of higher energy peak of Ti^+ is attributed to sputtering energy of metal atoms and can be explained as follows. Metal atoms are sputtered from the target by the impact of argon gas ions and then they diffuse away in the plasma and get ionized in dense plasma region due to the collisions with electrons, trapped in strong magnetic field of magnetron. These ions therefore have a similar energy same as the sputtered atoms, given by the Sigmund-Thompson distribution

$$F_T(\epsilon) \approx \frac{E_b}{(\epsilon + E_b)^3} \qquad eq(7.1)$$

Where E_b is the binding energy of metal atoms of target and $\in$ is the sputtered atom energy.

7.1.3 Conclusions

A technique for obtaining high time-resolution energy distribution function measurements in a HiPIMS discharge using the commercial energy resolved mass spectrometer (HIDEN Ltd EQP 300) has been demonstrated successfully. The key to this technique is the electrostatic gating of the ions inside the instrument's end cap. To demonstrate the performance of this technique, the time-resolved IEDFs measurement with 2 μs time resolution were carried in the HIPIMS discharge pulsed at frequency of 100 Hz, with a pulse width of 100 μs and average power of 680W.

The excellent agreement between the summation of all the time-resolved IEDFs measurements at different times during the pulse and a time-averaged measurement recorded by the mass spectrometer demonstrated that this technique is quite suitable for very high time-resolved measurements of IEDFs in the HiPIMS discharge.

It was found that the Ar^+ energy distribution has its maximum energy at 3 eV (corresponding to plasma potential) and extends up to 20 eV at 2 μs after the initiation of the discharge pulse. As the pulse develops, this energy spread extends to 35 eV possibly due to the energy transfer from Ti^+ via binary collisions.

The IEDFs of Ti^+ spread up to 50 eV at 20 μs after the initiation of cathode voltage pulse and further into the pulse, ions are detected with energies extending up to 100 eV.

7.2 Temporal Evolution of Ion Bombarding Energy at the Substrate Position

This section describes the investigation of temporal evolution of ion bombarding energies onto the floating substrate using an energy resolved mass spectrometer incorporated with the electrostatic ion shuttering technique.

7.2.1 Introduction

The temporal evolution of ion bombarding energy is very crucial parameter of the discharge that determines the quality of thin films deposited. Therefore a study has been carried out to investigate the temporal evolution of ion bombarding energy onto the substrate in the HiPIMS discharges.

7.2.2 Experimental Arrangement

The experimental arrangement was the same as it was used in previous study 7.1. In the present study, the time resolution of the IEDFs measurements was 10 μs.

7.2.3 Results and Discussion

7.2.3.1 Ion energy distribution functions for Ar^+ and Ar^{++}

The IEDFs of Ar^+ and Ar^{++} ions measured with the 10 μs time-resolution are shown in figure 7.6 and 7.7. As seen in the figure 7.6, the energy distributions of Ar^+ ions extends up to 15 eV and peaks at 3 eV. This low energy peak corresponds to slow Ar atoms ionized at the plasma potential V_p. The higher energy part of these distributions

can be attributed either to Ar atoms which gain energy in collisions with the sputtered Ti atoms [141] or Ar^+ ion-produced neutrals reflected from the target.

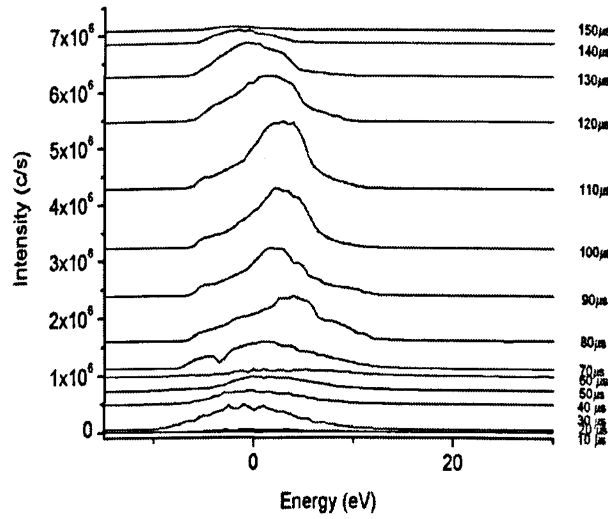

Figure 7.6: *A plot of IEDFs of Ar^+ with 10 μs time-resolution*

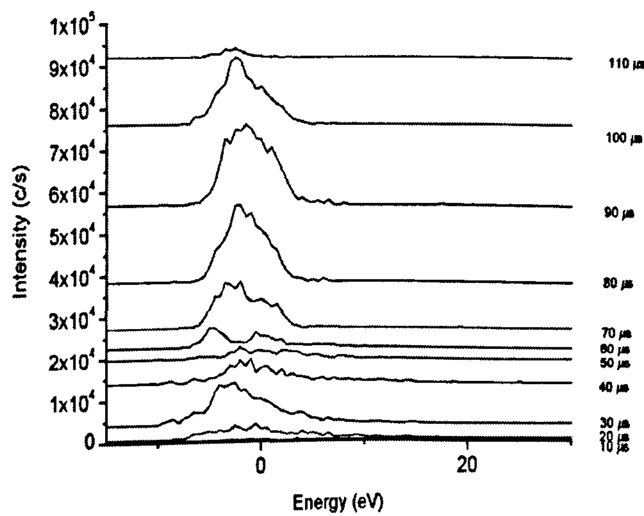

Figure 7.7: *A plot of IEDFs of Ar^{++} with 10 μs time-resolution*

An interesting feature observed in the Ar^+ IEDFs was the occurrence of two peaks in ion counts at times 30 and 100 μs after the initiation of the discharge pulse, however the peak in ion counts for the Ti^+ occurred at 30 μs after the initiation of the discharge pulse. A closer investigation of energy distributions of the Ti^+ ions (figure 7.8) shows that the energy peak of Ti^+ ions shifts towards the lower energy and peak ion counts decreases at times 60 μs after the initiation of the discharge pulse (shown by black arrow in figure 7.8). At the same time the Ar^+ ion peak counts increases. It is evident from the target current waveform that target current peaks at 30 μs after the initiation of the discharge pulse. Based on these observations, occurrence of two peaks in Ar^+ ion counts can be understood as follows. As the discharge pulse is switched on, the argon ions present in the discharge are accelerated towards the cathode. These ions incident on the target and produce the secondary electrons having very high energy (several hundred eV's depending upon the magnitude of the discharge pulse). These secondary electrons travel through the discharge, collide with the argon atoms and ionize them via electron impact ionization mechanism because atoms have fairly high electron impact ionization cross sections at this energy range (8.82 to 17.64 $\times$ 10^{-17} cm^2 at electron energies ranging 20 to 1 keV) [8].

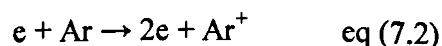

$$e + Ar \rightarrow 2e + Ar^+ \qquad eq\ (7.2)$$

As the target current decreases, the number of secondary electrons in the discharge decreases and it results in lower electron impact ionization. So the lower energy peaks seen in Ar^+ and Ti^+ ions, which are due to electron impact ionization, disappears.

A closer investigation of Ti^+ energy distributions (see figure 7.8) shows that energy and height of peak ion counts shift towards the lower side 60 μs after the initiation of the discharge pulse (shown by arrow in figure 7.8). At the same time second energy peak in Ar^+ ion counts emerges. It can be understood as follows. When the Ti^+ ions with sufficiently high energy collide with argon atoms, there is asymmetric charge exchange ionization between argon atoms and Ti^+ atoms [8].

$$Ar + Ti^+ \rightarrow Ar^+ + Ti \qquad \text{eq (7.3)}$$

It is an endothermic reaction with threshold energy of 8.9 eV [8], and hence rate constant for charge transfer collisions at thermal energies is very small. However, if either the Ar atoms or Ti^+ ions are in excited state, this cross-section can be large at thermal energies. From the figure 7.8, it is evident that at times 60 μs, the energy of Ti^+ ions is about 25 eV. Therefore charge exchange ionization becomes dominant in the later phase of the discharge pulse. In the Ar^+ IEDFs, a significant number of ions were detected with negative energy. The reason of this observation can be understood as follows. There is a deposition of the sputtered ionized metal flux on the sampling surface of the mass spectrometer. It creates charges on the surfaces surrounding the sampling aperture and thus shifts reference ground potential. This shift in the reference ground potential is the cause of this observed negative energy of the argon ions [141].

7.2.3.2 Ion energy distribution for Ti^+ and Ti^{++}

The IEDFs of Ti^+ and Ti^{++} ions are shown in figures 7.8 and 7.9.

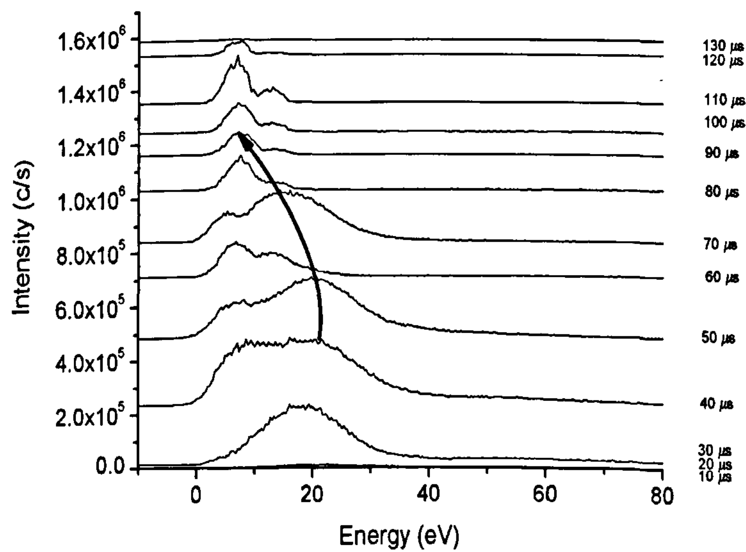

Figure 7.8: *A plot of IEDFs of Ti^+ with 10 μs time-resolution*

As it can be seen from the figure 7.8, energy distribution of Ti^+ extends up to 80 eV and peaks at 22eV.

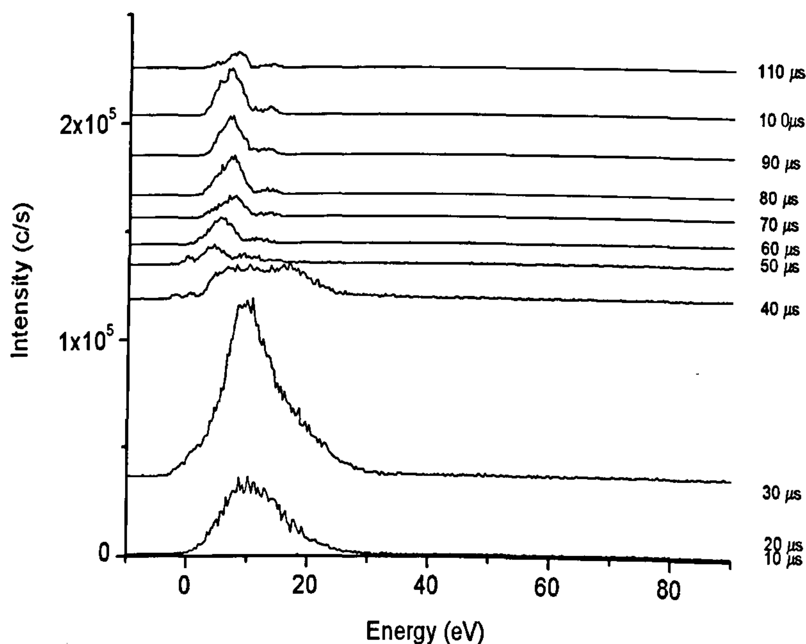

Figure 7.9: A plot of *IEDFs of* Ti^{++} *with 10 μs time-resolution*

The origin of this peak can be explained as follows. The metal atoms are sputtered from the target with an impact of the sputtering gas ions and then travel towards substrate. According to the Sigmund-Thompson sputtering theory, these sputtered atoms have a significant sputtering energy which depends upon the energy of incident sputtering ions and the binding energy of the sputtered atoms. On the way to the target, these metal atoms collide with the plasma ions and become ionized. Thus these metal ions have the sputtering energy associated with the sputtered metal atoms and also acquire an additional energy that is produced due to the potential difference between the bulk plasma and the grounded orifice of the mass spectrometer. Therefore the energy of the metal ions is composed of two parts, the first part is due to sputtering energy and the

second part is due to plasma potential. As it is evident from V_p profile (figure 4.6), the most of time the plasma potential is 3eV, so the rest of the energy of Ti^+, that is 19 eV, can attributed to the sputtered energy.

7.2.4 Conclusions

The time-resolved IEDFs were investigated in the HiPIMS discharge by the double gating technique, using the commercially available energy-resolved mass spectrometer by HIDEN analytical Ltd. The results show that Ti^+ has a longer tail than Ar+, in accordance with previous publications. It was also observed that the energy peaks in IEDFs of Ar^+ and Ti^+ were centred at 3 eV and 22 eV respectively. According to the Sigmund-Thomson sputtering theory, metal ions have the sputtering energy of sputtered metal atoms as well as energy gained while travelling in the electric field produced by the potential difference between the plasma potential and the grounded sampling orifice. It led us to conclude that the energy of Ti^+ ions was partly due to plasma potential, that is 3 eV, and partly due to the sputtering process that is 19 eV. Another observed feature was the occurrence of two peaks in Ar^+ ions counts in the IEDFs, at times 30 μs and 60 μs after the initiation of the discharge pulse respectively. We speculate that first peak was due to electron impact ionization and the second peak was due to charge exchange ionization.

Chapter 8

CONCLUSIONS AND OUTLOOK

This thesis presents a detailed study of time-resolved study of fundamental plasma parameters and their link to the global parameters to get better physical understanding of the discharges. To accomplish this purpose, various time-resolved diagnostics such as emissive probe, Langmuir probe, Mass spectrometry and power probe, have been designed and fabricated.

Previously it has been shown that using HiPIMS discharges for thin film deposition led to the controlled growth of engineering quality thin films and significantly improved film properties and that this could be linked to the details of particle and energy flux arriving at the substrate from the plasma. These are influenced by parameters such as plasma density, electron temperature and the potentials in the discharge and thus optimising these parameters will ultimately allow greater control of the properties of the deposited films.

Despite of many advantages, HiPIMS technique suffers a drawback of lower deposition rates than those in conventional magnetron sputtering discharges at the same average power levels. In the present study, it has been attempted to find out its reason why and a way to improve it. Detailed measurements were carried out to investigate the factors that influence these plasma parameters in an attempt to quantify the characteristics of the HiPIMS discharges and further understand the influence of the magnetron's magnetic field strength on the discharge. The main results have been discussed at the end of each chapter. These are summarized here together with suggestions for the routes future work can take.

8.1 Conclusions

1. From the plasma potential V_p profile discussed in chapter 4, it is clear that the V_p readily responds to the cathode discharge voltage V_d with an additional double layer like potential structure named as '*second peak*' structures during the pulse on-time. The emergence of this 'second peak' might be a signature of the evolution of the titanium ions Ti^+ in the discharge as occurrence of Ti^+ has been observed at the same time during the pulse in mass spectroscopic measurements in the same conditions.

   The spatial map of the plasma potential distributions shows a large potential variation (~125 V) in a very small region ($10 < z < 40$ mm) above the racetrack during the 'first peak', it can be attributed as the extended presheath region close to the cathode cause much greater ion acoustic speeds compared to the classical Bohm speeds at the sheath edge determined by $(kT_e/M_i)^{1/2}$.

   This large variation in the V_p produces the large axial electric field pointing towards the cathode. This electric field hampers the transport of the plasma ions to the substrate and one of the main causes of the observed lower deposition rate in HiPIMS discharges. The radial and axial electric field derived from the plasma potential V_p measurements show the existence of the strong axial electric field directed towards the magnetron close to the cathode that acts like a potential barrier for the plasma ions travelling to the substrate and therefore back scatters the ions.

This axial electric field together with the magnetic field creates large electron E × B drift speeds that, probably, deflect the ions towards the chamber wall. The existence of radial electric field pointing to the chamber walls also plays an important role in the discharge dynamics and transports the plasma ions towards the wall.

2. Power density measurements onto the isolated substrate indicate that the magnetron's magnetic field strength can be used to control the thermal loading of the substrate. By reducing the magnetic field strength by 45% could reduce power density onto the substrate by 28%. This finding is very important in the context of depositing thin films onto the thermally sensitive substrates such polymeric web. Lowering the discharge pulse frequency also reduces the power density. Plasma density measurements indicate lower plasma density at lower field strength which might be the probable cause of lower power density at the substrate.

3. A comparative study of magnetic field effect on the deposition rates in the HiPIMS, DC and pulsed DC discharges revealed that the magnetron's magnetic field strength is a crucial parameter that determines deposition rate for a given set of operating conditions. The measurements carried out in the HiPIMS mode show that the deposition rate increased by a factor of 2 times with lowering the magnetic field strength by 40% at the target. Increasing the pulse frequency at constant pulse on-time also enhances the deposition rates due to increased duty factor and more plasma present above the substrate on time-average.

However investigations carried out in the DC and pulsed DC (100 and 350 kHz) modes revealed that deposition rate decreased with the lower field strength due to less ionization efficiency, reduced plasma densities and lower sputtering rates.

By selecting the magnetic field strength best suited to depositing your film of choice, film properties can be optimized and improved.

4. A technique for obtaining high time-resolution energy distribution function measurements in a HiPIMS discharge using a commercial energy resolved mass spectrometer (HIDEN Ltd EQP 300) incorporated with electrostatic gating of ions has been demonstrated successfully. To demonstrate the performance of this technique, time-resolved IEDFs measurements with 2 μs time resolution, were carried out in the HIPIMS discharge and gave excellent agreement between the summation of all the time-resolved IEDFs measurements and a time-averaged demonstrated the suitability of this technique for very high time-resolved measurements of IEDFs in the HiPIMS discharge.

It was found that Ar^+ energy distribution has its maximum energy at 3 eV (corresponding to plasma potential) and extends up to 20 eV at 2 μs after the initiation of the discharge pulse. As the pulse develops, this energy spread extends to 35 eV possibly due to the energy transfer from Ti^+ via binary collisions. In the present study, it was found that the magnetic field strength of the magnetron plays a very important role in plasma transport and dynamics. By choosing the right magnetic field strength, the deposition rate can be enhanced and the power to the substrate can be reduced.

8.2 Outlook for the Future Work

The experimental findings in this study suggest several research interests that could be explored. It will be interesting to investigate following issues.

1. It has been found in the present study that the lower magnetic field strength enhances the deposition rates. It could be of quite interesting to investigate how reduced magnetic field strength affects the thin film properties by depositing thin films and analyzing them.
2. Lower magnetic field strength reduces the power onto the substrate. It would be interesting to study how the energy associated with different plasma particles varies with magnetic field strength by method of biasing the probe.
3. As the discharge dynamics is responsible for the thin film properties, therefore, it is worth knowing the discharge dynamics and the parameters affecting it so that thin film properties could be tailored according to the applications. A detailed time-resolved Langmuir probe investigation will be able to give a complete picture of the discharge dynamics in the HiPIMS technique and the effect of various parameters such as pulse frequency, pulse width and magnetic field effect on it.
4. It is worth developing a self consistent model of the HiPIMS technique.
5. It is necessary to optimize the sputtering system to achieve the higher ionization rate, higher deposition rate, less power density, improved target utilization and control over the incident ion bombarding energy.

REFERENCES

[1] Musil J, Herman D and Sicha J, *Jn. Vac. Sci. Technol. A: Vacuum, Surfaces and Films,* 2006, 24 (3) 521

[2] Audronis M, Leyland A, Kelly P J and Matthews A, *Surf. Coat. Technol.*2006, 201 (7) 3970

[3] Frach P, Glo D, Goedicke K, Fahland M and Gnehr W M, *Thin Solid Films.* 2003, 445 (2) 251

[4] Kelly P J, O'Brien J and Arnell R D, *Vacuum.* 2004, 74 (1) 1

[5] Kelly P J and Arnell R D, *Vacuum* .2000, 56 (3) 159

[6] Lowenheim Frederick A , Electroplating of Surface Finishing, McGraw-Hill Book Co., New York, 1978

[7] Schwartz R W, Schneller T and Waser R *C R, Chime*, 2004 (7) 433

[8] Lieberman M A and Lichtenberg A J, *Principles of Plasma Discharges and Materials Processing*, John Wiley & Sons, Inc.,1994

[9] Vossen L J and Kern W, *Thin Film Processes II, Academic Press Inc.*, 1250, Sixth Avenue, San Diago, CA, 1991

[10] Willmott P R and Huber J R, *Review of Modern Physics.* 2000, 72 (1) 315

[11] Rossnagel S M, Sputter Deposition, In: Sproul W D, Legg K O, editors. *Opportunities for Innovation: Advanced Surface Engineering*. Switzerland: Technomic Publishing Co., 1995.

[12] Window B and Savvides N, *J. Vac. Sci. Technol. A.* 1986, 4 (3) 453

[13] Schiller S, Goedicke K, Reschke J, Kircho V, Schneider S, and Milde F, *Surf. Coat. Technol.*1993, 61, 331.

[14] Scherer M, Schmitt J, Latz R and Schanz M J, *Vac. Sci. Technol. A*, 1992, 10, 1772.

[15] Kelly P J, Abu-Zeid O A, Arnell R D and Tong J, *Surf Coat. Technol.* 1996, 86, 87

[16] Lane M et al., *Jn. Mater. Res.* 2000, 15, 203

[17] Chen X et. al., *Acta. Mater.* 2003, 51, 2017

[18] Ehiasarian A P, New R, Munz W-D, Hultman L, Helmersson U, and Kouznetsov V, *Vacuum , 2002, 65 (147) 154*

[19] Bohlmark J, Lattemann M, Gudmunsson J T, Ehiasarian A P, Aranda-Gonzalo Y, Brenning N and Helmersson U, *Thin Solid Films.* 2006, 515, 1522

[20] Alami J, Persson P O A, Music D and Gudmundsson J T, *J. Vac. Sci. Technol. A.* ,2005 *(23) 278*

[21] Rossnagel S M, *J. Vac. Sci. Technol. B,* 1998, *16 , 2585*

[22] Ehiasarian A P, Hovsepian P Eh, Hultman L and Helmersson U, *Thin Solid Films.* 2004, *457, 270*

[23] Mishra A, Clarke G C B, Kelly P J and Bradley J W, *Plasma Process and Polymers.* 2009, *6, S610-S614*

[24] Hecimovic A and Ehiasarian A P, *J. Phys. D: Appl. Phys.* 2009, *42, 135209*

[25] Macak K, Kouznetsov V, Schneider J and Helmersson U, *J. Vac. Sci. Technol. A.* 2000, *18, 1533*

[26] Ehiasarian A P, Munz W-D, Hultman L, Helmersson U and Petrov I, *Surf. Coat. Technol.* 2003, *163-164 267*

[27] Chen F F, *Introduction to Plasma Physics and Controlled Fusion*, Volume 1: Plasma Physics, Plenum Press, 2nd Edition, 1984

[28] Konuma M, *Plasma Techniques for Film Deposition*, Alpha Science International Ltd, 2005

[29] Huddlestone R H and Leonard S L, *Plasma Diagnostic Techniques*, Academic Press, New York, 1965

[30] Chapman B, *Glow Discharges Processes*, John Wiley and Sons, 1980

[31] Rossnagel S M, *J. Vac. Sci. Technol. A*, 1988, 6 3, 1821

[32] Bradley J W, Backer H, Kelly P J and Arnell R D, *Surf. Coat. Technol.* 2001, 84, 47

[33] Bradley J W, Backer H, Kelly P J and Arnell R D, *Surf. Coat and Technol.* 2001, 142-144, 337

[34] Swindles I, Kelly P J and Bradley J W, *New Jn. Phys.* 2006, 8 4,47

[35] Anders A, *Surf. Coat. Technol.* 2004, 183, 301

[36] Gu L and Lieberman M A, *J. Vac. Sci. Technol. A: Vacuum Surfaces and Films* 1988, 6 5, 2960

[37] Rossnagel S M and Kaufman H R, *J. Vac. Sci. Technol. A: Vacuum, Surfaces and Films*, 1986, 4 3, 1822

[38] Schiller S, Goedicke K, Reschke J, Kirchoff V, Schneider S and Milde F, *Suf. Coat. Technol.* 1993, 61, 331

[39] Ziegler J F and Biersack J P, *SRIM, The Stopping Range of Ions in Matter*, 2003

[40] Vossen J L and Kem W, *Thin Film Processes*, Academic Press, 1991

[41] Mattox D M, *Handbook of Physical Vapor Deposition (PVD) processing*, 907 William Andrew Publishing/Noyes, 1988

[42] Bunshah R F, *Handbook of Deposition Technologies for Films and Coatings-Science, Technology and Applications* (2nd Addition), William Andrew Publishing/Noyes, 1994

[43] Westwood W D, *Sputter Deposition, American Vacuum Society.* 2003 Education Committee (2), 285

[44] Penning F M, *Physica (Utrecht),* 1936, 3, 873

[45] Window B and Savvides N, *J. Vac. Sci. Technol. A.* 1986, 4 (2)196

[46] Window B and Savvides N, *J. Vac. Sci. Technol. A.*1986, 4 (3) 453

[47] Window B and Savvides N, *J. Vac. Sci. Technol. A.*1986, 4 (3) 504

[48] Arnell R D and Kelly P J, *Surf. Coat. Technol.* 1999, 112, 176

[49] Kouznetsov V, Macak K, Schneider J M, Helmersson U and Petrov I, *Surf. Coat. Technol.* (1999) 122, 29

[50] Helmersson U, Latterman M, Bohlmark J, Ehiasarian A P and Gudmundsson J T, *Thin Solid Films* . 2006, 1, 513

[51] Ehiasarian A P, Wen J G and Petrov I, *J. Appl. Phys.* 2007,101, 054301

[52] Berg S and Nyberg T, *Thin Solid Films.* 2005, 476, 215

[53] Kemp R F and Sellen J M, *Rev. Sci. Instr.* 1966, 37, 445

[54] Chen F F, Huddlestone R H and Leonard S L, *Plasma Diagnostics Techniques ed.* (New York: Academic Press), 1965 Ch. 4

[55] Wang E Y , Intrator T and Hershkowitz N, *Rev. Sci. Instr.* 1985, 50, 210

[56] Takamura S , Ye M Y, Kuwabara T and Ohno N, *Phys Plasmas* (1998) 5, 2151

[57] Smith J R, Hershkowitz N and Coakley P, *Rev. Sci. Instr.* 1979, 50 , 210

[58] Bradley J W, Karkari S K and Vetushka A, *Plasma Sources Sci. Technol.* 2004, 13, 189

[59] Pajdarova A. D, Vlcek J, Kudlacek and Lukas J., *Plasma Sources Sci. Technol.* 2009, 18, 025008

[60] Steffen H, Kersten H and Wulf H, *J. Vac. Sci. Technol. A,* 1994, 12 (5) 2780

[61] Kersten H, Steffen H, Vender D and Wagner H E., Vacuum, 1995, 46 (3) 305

[62] Thornton J A, *Thin Solid Films.* 1978, 54 (1) 23

[63] Wendt R, Ellmer K and Wieswmann K, *J. Applied Physics.* 1997, 82 (5) 2115

[64] Musil J, Kaldec S, Valvoda V, Kuzel J and Cerny R, *Surf. Coat. Technol.* 1990, 4344, 259

[65] Kelly P J and Arnell A D, *Jn. Vac. Sci. Technol. A: Vacuum, Surfaces and Films*. 1998, 16 (5) 2858

[66] Petrov I, Myers A, Greene J E and Abelson J R, *Jn. Vac. Sci. Technol. A: Vacuum, Surfaces and Films.* 1994, 12 (5) 2846

[67] Langmuir I and Mott-Smith H.M., *Phys. Rev.*1926, 28, 727

[68] Allen J E, Boyd R L F and Reynolds P, *Proc. Phys. Soc.* 1957, 70, 297

[69] Laframboise J G, University of Toronto Institute for Aerospace Studies, *UTIAS Report N*, 1966, 100

[70] Godyak V A, Piejak R B and Alexandrowich B M, *J. Appl. Phys.* 1993, 73(8) 3657

[71] Lee S W, Seo S H, In J H, Chung C W and Chang H Y, *Phys. Plasmas.* 2005, 12, 063502

[72] Seo S H, In J H and Chang H Y, *Plasma Sources Sci. Technol.* 2005, 14, 576

[73] Seo S H and Chang H Y, *Phys. Plasmas.* 2004, 11 (7) 3595

[74] Backer H and Bradley J W, *Plasma Sources Sci. Technol.* 2005, 14, 419

[75] Backer H, *Time-Resolved Measurements on Pulsed Plasmas for Thin Film Deposition*, Ph.D Thesis, UMIST, 2003.

[76] Mason S J, Proc. IRE , 1953, 41, 1144

[77] Christie D J, *J. Vac. Sci. Technol.* A . 2005, 23, 330

[78] Helmersson U, Lattemann M, Alami J, Bohlmark J, Ehiasarian A P, and Gudmundsson .J T, *48th Annual Technical Conf. of Society of Vacuum Coaters,* (Denver, CO, USA), 2005, 458

[79] Emmerlich J, Mraz S, Snyders R, Jiang K and Schneider M, *Vacuum.* 2008, 82 867.

[80] Bohlmark J, Ostbye M, Lattemann M, Ljungcrantz H, Rosell T and Helmersson U, *Thin Solid Film.* 2006, 515, 1928

[81] Lundin D, Larsson P, Wallin E, Lattermann M, Brenning N and Helmersson U, *Plasma Sources Sci. Technol.* 2008, 17, 035021

[82] Konstantinidis S and Dauchot J P, *Appl. Phys. Lett.* 2006, 88, 021501

[83] Bradley J W, Thompson S and Gonzalvo Y A , *Plasma Sources Sci. Technol.* 2001, 10, 490

[84] Vetushka A, Karkari S and Bradley J W, *J. Vac. Sci. Technol. A.* 2004, 22, 2459

[85] Gudmundsson J T, Alami J and Helmersson U , *Surf. Coat. Technol.* 2002, 161, 249

[86] Gudmundsson J T, Alami J and Helmersson U, *Appl. Phys. Lett.* 2001, 78 (22) 3427

[87] Welzel Th, Dunger Th, Leibig L and Richter F, *New J. Phys.* 2008, 10, 123008

[88] Karkari S K, Vetushka A and Bradley J W, *J. Vac. Sci. Technol.* 2003, A 21 (6) L28

[89] Balan P, Schrittwieser R, Ionita C, Cabral J A, Figueiredo H.F.C, Fernandes H and Varandas C, *Rev Sci. Inst.* 2003, 74 (3) 1584

[90] Poolcharuansin P and Bradley J W, *Plasma Sources Sci. Technol.* 2010, 19, 025010

[91] Bradley J W and Welzel T, *J. Phys.D: Appl. Phys.* 2009, 42, 093001

[92] Van der Straaten T A, Cramer N F, Falconer I S and James B W, *J. Phys.D: Appl. Phys.* 1998, 31, 177

[93] Rossnagel S M and Kaufman H R, *J. Vac. Sci. Technol. A* . 1987, 5 (1) 88

[94] Vetushka A and Bradley J W, *J. Phys.D: Appl. Phys.* 2007, 40, 2037

[95] Sigmund P, *Phys Rev* .1969, 184, 383

[96] Van der Straaten T A, Cramer N F, Falconer I S and James B W, *J Phys.D: Appl. Phys.* 1997, 31, 191

[97] Brenning N, Axnas I, Raadu M A, Lundin D and Helmerson U, *Plasma Sources Sci. Technol.* 2008,17, 045009

[98] Schmidt D P, Meezan N B, Hargus W A Jr. and Cappelli M A., *Plasma Sources Sci. Technol.* 2000, 9, 68

[99] Kaufman H R, *J. Spacecraft.* 1984. 21, 558

[100] Gilo M and Croitoru N, *Thin Solid Films.* 1999, 350, 203

[101] Sheridan T E, Goeckner M J and Goree J, *J. Vac. Sci. Technol. A.* 1998, 16, 2173

[102] Kakati H, Pal A R, Bailung H and Chutia J, J *Phys D: Appl. Phys.* 2007, 40, 6865

[103] Rossnagel S M and Kaufman H R, *J. Vac. Sci. Technol. A*. 1987, 5, 2276

[104] Fujita H, Yagura S, Ueno H and Nagano M, *J. Phys D: Appl. Phys.* 1986, 19, 1699

[105] Mishra A, Kelly P J, and Bradley J W., *Plasma Sources Sci. and Technol.* 2010, 19, 045014

[106] Mishra A, Kelly P J and Bradley J W, *29th ICPIG,* 2009, *Cancun Mexico*

[107] Bradley J W, *Plasma Sources Sci. Technol.* 1996, 5, 622

[108] Pekker L, *Plasma Sources Sci. and Technol.* 1995, 4 31

[109] Klabunde F, Lohmann M, Blasing J and Drusedua T, *J. Appl. Phys.* 1996, 80, 6266

[110] Gardeneniers J, Rittersma Z and Burger G J, *Appl. Phys.* 1998, 83, 7844

[111] Vink T J and Zon J B von , *Vac.Sci, Technol A*. 1991, 9,124

[112] Lee S W, Seo S H, In J H, Chung C W and Chang H Y, *Phys. Plasmas.* 2005,12, 06350280, 6266

[113] Graham M E and Sproul W D, *Society of Vacuum Coaters, 37th Annual Technical Conference Proceedings.* 1994, p 275 - 279.

[114] Musil J, Valvoda V, Kadlec S and Vyskocil J, *IPAT 87, Proceeds of the 6th International conference on Ion and Plasma Assisted Techniques, Brighton UK.* 1987, 184-189.

References

[115] Larsson T, Blom H O, Nender C and Berg S, *J. Vac. Sci. Technol. A*. 1988, 6 , 3, 1832, 1836.

[116] Schiller S, Heisig U, Steinfelder K, Strumpfel J and Sieber W, *Vakuum technik*. 1981, 30, p 1- 21.

[117] Rizk A, Youssef S B, Habib S K, *Vacuum*. 1988, 38 (2) p 93-95.

[118] Vossen J L, Krommenhoek S and Koss A V, *J. Vac. Sci. Technol. A*. 1991, 9, 3, 600603.

[119] Okamoto A and Serikawa T, *Thin Solid Films*. 1986,137, p 143-151.

[120] Schiller S, Heisig U, Korndfirfer Chr, Beister G, Reschke J, Steinfelder K and Strqmpfel J, *Surf. Coat. Techno*. 1987, 33, 405.

[121] Belkind A, Gerristead W, Orban Z, Dow D, Felts J and Laird R, *Surf. Coat. Technol*. 1991, 49, p 155–160.

[122] Belkind A, Laird R, Orban Z and Rafalko P W, *Thin Solid Films*. 1992, 219, p 46– 51.

[123] Laird R and Belkind A, *J. Vac.Sci. Technol. A10*. 1992, (4), p 1908–1912.

[124] Belkind A, *J. Vac. Sci. Technol. A11*. 1993 (4) p 1501– 1509.

[125] Lundin D, Stahl M, Kersten H and Helmersson U, *J. Phys. D: Appl. Phys*. 2009, 42, 185202

[126] Wolter M, Stahl M, Kersten H, *Vacuum*. 2009, 83, 768

[127] Kersten H, Rohde D, Berndt J, Deutsch H and Hippler R, *Thin Solid Films*. 2000, 585, p 377-378

[128] Cada M, Bradley J W, Clarke J C B and Kelly P J, *J. Appl. Phys*. 2007, 102 063301,

[129] In Jung-Hwan, Seo Sang-Hun and Chang Hong-Young, *Surf. Coat. Technol.* 2008, 2002, 5298

[130] Solochenko I A, *Rev. Sci. Instrum.* 1996, 67, 1646

[131] Ekpe Samuel D, Jimenez F J, Field D J, Davis M J and Dew S K J, *Vac. Sci. Technol. A.* 2009, 27, (6), 1275

[132] Kelly P J, Onifade Ayokola A, Zhou Y, Clarke G C B, Audronis M and Bradley J W, *Plasma Process and Polymer.* 2007, 4, 246

[133] Yamamura Y and Tawara H, NISF *DATA*-23, 1995

[134] Burcalova K, Hecomovic A and Ehiasariaan A P, *J.Phys.D: Appl. Phys. 2008*, 41,115306

[135] Hecomovic A, Burcalova K and Ehiasariaan A P, *J.Phys.D: Appl. Phys. 2008*, 41,095203

[136] Ehiasariaan A P and Vetushka A, *Conference Proceedings*, PSE, 2008

[137] Vlcek J, Kudlacek P, Burcalova K and Musil J, *Europhysics Letters* . 2007, 77, 45002

[138] Voronin S A, Clarke G C B, Cada M, Kelly P J and Bradley J W, *Meas. Sci. Technol.* 2007,18,1872

[139] Olthoff J K, Van Brunt R J and Radovanov S B, *Appl Phys. Lett.* 1995, 67, 473

[140] Kadlec S, Quaeyhagenes C, Knuyt G and Stals L M, *Surf. Coat Technol.* 1997, 89,177

[141] Misina M W, Shaginyan L R, Macek M and Panjan P, *Surf. Coat. Technol.* 2001, 348,142